Washington University in St. Louis
Washington University Open Scholarship

Engineering and Applied Science Theses & Dissertations

McKelvey School of Engineering

Winter 12-15-2018

Graphene Oxides in Water: Characterization, Reactivity, and Application

Siyuan An
Washington University in St. Louis

Follow this and additional works at: https://openscholarship.wustl.edu/eng_etds

Part of the Chemical Engineering Commons

Recommended Citation
An, Siyuan, "Graphene Oxides in Water: Characterization, Reactivity, and Application" (2018). *Engineering and Applied Science Theses & Dissertations*. 397.
https://openscholarship.wustl.edu/eng_etds/397

This Dissertation is brought to you for free and open access by the McKelvey School of Engineering at Washington University Open Scholarship. It has been accepted for inclusion in Engineering and Applied Science Theses & Dissertations by an authorized administrator of Washington University Open Scholarship. For more information, please contact digital@wumail.wustl.edu.

WASHINGTON UNIVERSITY IN ST. LOUIS

School of Engineering and Applied Sciences

Department of Energy, Environmental and Chemical Engineering

Dissertation Examination Committee:
John Fortner, Chair
Marcus Foston
John Gleaves
Erik Henriksen
Young-Shin Jun

Graphene Oxides in Water: Characterization, Reactivity, and Application

by

Siyuan An

A dissertation presented to
The Graduate School
of Washington University in
partial fulfillment of the
requirements for the degree
of Doctor of Philosophy

December 2018
St. Louis, Missouri

© 2018, Siyuan An

Table of Contents

List of Figures vii

List of Tables xvii

Acknowledgments xx

Abstract of the Dissertation xxii

Chapter 1: Introduction 1

1.1 Dissertation Organization 1

1.2 Background 2

1.2.1 Graphene and Derivatives 2

1.2.2 Graphene oxide 3

1.2.3 Carbon Atom Hybridization 5

1.2.4 Graphene Oxide Environmental Behavior and Potential Risk 7

1.2.4 Graphene Oxide Membranes 7

1.2.5 Rare Earth Metals 9

1.3 Objectives 10

Chapter 2 Graphene Oxide Synthesis and Characterization 12

Abstract 12

2.1 Introduction 12

2.2 Materials and Methods 13

2.2.1 Materials 13

2.2.2 Graphene Oxide Synthesis 13

2.2.3 Characterization 15

2.3 Results and Discussion 18

2.3.1 Reaction Temperature 18

2.3.2 Reaction Time 20

2.3.3 Oxidant Ratio 22

2.3.4 Sonication 24

2.3.5 TEM Imaging 29

2.3.6 UV-visible Spectroscopy and Band Gap 29

2.3.7 Raman Spectroscopy 31

2.3.8 Thermogravimetric Analysis (TGA) 33

2.3.9 Fourier Transform Infrared Spectroscopy 34

2.3.10 Hydrodynamic Size Distribution, Zeta Potential, and Colloidal Stability 35

2.4 Conclusion 40

Chapter 2: Supporting Information 41

Chapter 3: Photoenhanced Transformation of Graphene Oxide by Free Chlorine: Reaction Kinetics and Product Characterization 44

Abstract 44

3.1 Introduction 44

3.2 Materials and Methods 46

3.2.1 Materials 46

3.2.2 Synthesis of Graphene Oxide 46

3.2.3 Graphene Oxide Reaction with Free Chlorine under Light Irradiation 47

3.2.4 Product Characterization 47

3.2.5 Chlorine Concentration Measurement 48

3.2.6 Carbon Dioxide Quantification 48

3.2.7 Instrumentation 49

3.3 Results and Discussion 50

3.3.1 Reaction Kinetics 50

3.3.2 Product Characterization 59

3.3.3 Carbon Mass Balance Analysis 63

3.3.4 Reaction Mechanism 68

3.4 Conclusions 69

Chapter 3: Supporting Information 70

Chapter 4: The Effect of Free Chlorine and Light Irradiation on Graphene Oxide Membrane: Stability and Water Flux 74

Abstract 74

4.1 Introduction 74

4.2 Materials and Methods 75

4.2.1 Materials 75

4.2.2 Graphene Oxide Membrane Synthesis 76

4.2.3. Chlorination experiments 76

4.2.4. Membrane Permeability 77

4.2.5. Characterization 78

4.3. Results and Discussion 78

4.3.1 Chemical Stability 78

4.3.2. Carbon Oxidation State Change 80

4.3.3. Effect of pH 83

4.3.4. Reaction Time 84

4.3.3 Surface Roughness 85

4.3.6. Water Flux 86

4.4. Conclusion 87

Chapter 4: Supporting Information 88

Chapter 5: High Efficiency Aqueous Cerium(III) and Lanthanum(III) Adsorption on Graphene Oxide 90

Abstract 90

5.1 Introduction 90

5.2 Materials and Methods 94

5.2.1 Material. 94

5.2.2 Graphene oxide synthesis 94

5.2.3 Graphene oxide characterization. 95

5.2.4 Adsorption experiments. 95

5.3 Results and Discussion 97

5.3.1 Graphene oxide characterization before and after the adsorption. 97

5.3.2 Isotherm Modeling. 99

5.3.3 Sorption Kinetics 103

5.3.4 Effect of pH. 104

5.3.5 Effect of Ionic Strength. 107

5.4 Conclusion 109

Chapter 5: Supporting information. 110

Chapter 6: Conclusions and Recommendations 123

6.1 Conclusions 123

6.1.1 Graphene Oxide Synthesis and Characterization 123

6.1.2 Graphene Oxide Photo-Transformation by Free Chlorine. 124

6.1.3 Chlorination Effect on Graphene Oxide Membrane under Light Irradiation 124

6.1.4 Graphene Oxide Application on Rare Earth Metal Adsorption 125

6.2 Recommended Future Work 125

6.2.1 Graphene Oxide Synthesis and Characterization 125

6.2.2 Graphene Oxide Environmental Fate and Transport 126

6.2.3 Graphene Oxide Composite Membrane Modification and Stability 126

6.2.4 Graphene Oxide Composite for Heavy Metal Adsorption 127

Reference 128

List of Figures

Figure 1.1 Graphene as parent of all graphitic forms: fullerene, carbon nanotube and graphite[1] .. 3

Figure 1.2 Carbon atom with sp^3 hybridized orbital 5

Figure 1.3 Carbon atom with sp^2 hybridization 6

Figure 1.4 Carbon atom with sp hybridization 6

Figure 1.5 Graphene oxide electron delocalization of sp^2 hybridized orbitals. 7

Figure 2.1. Oxidation state change (from XPS C 1s scan) with reaction temperature, with T1 (10, 30, 50 °C) for stage 1 and T2 (30, 60, 90 °C) for stage 2. Reaction time is 2 hours for stage 1 and 60 min for stage 2, with oxidant ratio of 3:1. The sonication time is 2 hours. 19

Figure 2.2 Yield change with reaction temperature, with T1 (10, 30, 50 °C) for stage 1 and T2 (30, 60, 90 °C) for stage 2. Reaction time is 2 hours for stage 1 and 60 min for stage 2, with oxidant ratio of 3:1. The sonication time is 2 hours. 20

Figure 2.3 Reaction time effect on the carbon oxidation state (from XPS C 1s scan) of graphene oxide, with t1 (1, 2, 3, 4 hours) for stage 1 and t2 (0, 30, 60 90 120 min) for stage 2. Reaction temperature is 30 °C for stage 1 and 60 °C for stage 2, with oxidant ratio of 3:1. The sonication time is 2 hours. 21

Figure 2.4 Reaction time effect on the yield of graphene oxide, with t1 (1, 2, 3, 4 hours) for stage 1 and t2 (0, 30, 60 90 120 min) for stage 2. Reaction temperature is 30 °C for stage 1 and 60 °C for stage 2, with oxidant ratio of 3:1. The sonication time is 2 hours. 22

Figure 2.5 Oxidation state change (from XPS C1s scan) with oxidant ratio (1:1, 3:1, 5:1). The other reaction conditions are: 30 °C in stage 1 for 2 hours, 60 °C in stage 2 for 60 min and sonication for 2 hours..... 23

Figure 2.6 Yield change with oxidant ratio (1:1, 3:1, 5:1). The other reaction conditions are: 30 °C in stage 1 for 2 hours, 60 °C in stage 2 for 60 min and sonication for 2 hours..... 23

Figure 2.7 GO solution before and after 2 h sonication, supernatant vs. precipitate. The reaction conditions are: 30 °C in stage 1 for 2 hours, 60 °C in stage 2 for 60 min, oxidant ratio of 3:1 and sonication for 2 hours..... 25

Figure 2.8 Oxidation state change of the graphitic oxide and corresponding graphene oxide with sonication time ranging from 0 to 6 hours. The other reaction conditions are: 30 °C in stage 1 for 2 hours, 60 °C in stage 2 for 60 min and oxidant ratio of 3:1..... 26

Figure 2.9 Sonication yield change with sonication time ranging from 0 to 6 hours. The other reaction conditions are: 30 °C in stage 1 for 2 hours, 60 °C in stage 2 for 60 min and oxidant ratio of 3:1..... 27

Figure 2.10 Initial graphitic oxide concentration (total mass) effect on yield and oxidation state. The graphitic oxide is synthesized with reaction conditions as: 30 °C in stage 1 for 2 hours, 60 °C in stage 2 for 60 min, oxidant ratio of 3:1 and sonication for 2 hours..... 28

Figure 2.11 TEM images of graphene oxide synthesized with conditions as: 30 °C in stage 1 for 2 hours, 60 °C in stage 2 for 60 min, oxidant ratio 3:1 and sonication for 2 hours. 29

Figure 2.13 UV-vis spectra of graphene oxide. The GO is synthesized at temperature of 10 °C and 30 °C (GO-1), 30 °C and 60 °C (GO-2) and 50 °C and 90 °C (GO-3). Other reaction conditions are: reaction time of 2 hours for stage 1 and 60 min for stage 2, oxidant ratio of 3:1 and sonication for 2 hours. 30

Figure 2.14 Raman spectra of GO. The GO is synthesized at temperature of 10 °C and 30 °C (GO-1), 30 °C and 60 °C (GO-2) and 50 °C and 90 °C (GO-3). Other reaction conditions are: reaction time of 2 hours for stage 1 and 60 min for stage 2, oxidant ratio of 3:1 and sonication for 2 hours. 31

Figure 2.15 TGA result of GO. The GO is synthesized at temperature of 10 °C and 30 °C (GO-1), 30 °C and 60 °C (GO-2) and 50 °C and 90 °C (GO-3). Other reaction conditions are: reaction time of 2 hours for stage 1 and 60 min for stage 2, oxidant ratio of 3:1 and sonication for 2 hours. 34

Figure 2.16 FTIR spectra of three types of graphene oxide. The GO is synthesized at temperature of 10 °C and 30 °C (GO-1), 30 °C and 60 °C (GO-2) and 50 °C and 90 °C (GO-3). Other reaction conditions are: reaction time of 2 hours for stage 1 and 60 min for stage 2, oxidant ratio of 3:1 and sonication for 2 hours. 35

Figure 2.17 Zeta potential of GO under different pH levels. The GO is synthesized at temperature of 10 °C and 30 °C (GO-1), 30 °C and 60 °C (GO-2) and 50 °C and 90 °C (GO-3). Other reaction conditions are: reaction time of 2 hours for stage 1 and 60 min for stage 2, oxidant ratio of 3:1 and sonication for 2 hours. 37

Figure 2.18 Critical coagulation of GO with Na^+. The GO is synthesized at temperature of 10 °C and 30 °C (GO-1), 30 °C and 60 °C (GO-2) and 50 °C and 90 °C (GO-3). Other reaction conditions are: reaction time of 2 hours for stage 1 and 60 min for stage 2, oxidant ratio of 3:1 and sonication for 2 hours. 38

Figure 2.19 Critical coagulation of GO with Mg^{2+}. The GO is synthesized at temperature of 10 °C and 30 °C (GO-1), 30 °C and 60 °C (GO-2) and 50 °C and 90 °C (GO-3). Other reaction conditions are: reaction time of 2 hours for stage 1 and 60 min for stage 2, oxidant ratio of 3:1 and sonication for 2 hours. 39

Figure 3.1 UV-vis spectra and photo of graphene oxide in UV/free chlorine system. 1A(1), 1B: GO (50 mg/L) with 200 mg/L free chlorine at pH 5 under UV irradiation (2000 μW/cm^2) for 2 h. 1A(2), 1C: GO (50 mg/L) with 200 mg/L free chlorine in dark. 1A(3), 1D: GO (50 mg/L) under UV irradiation (2000 μW/cm^2). 50

Figure 3.2 Peak position change in UV-vis spectra of GO with reaction time for 50 mg/L GO under UV irradiation (2000 μW/cm^2) for 2 hours at pH 5, with/without 200 mg/L free chlorine. 52

Figure 3.3 Kinetics of GO in UV/free chlorine system. 3.3A: GO ratio remained in the solution, which was taken from the absorbance of 230 nm in UV-vis spectra, under different free chlorine concentrations (mg/L) at pH 6 with UV irradiation (2000 μW/cm2). 3.3B: pseudo first order rate constants of GO with different free chlorine concentrations at different pH levels under UV irradiation (2000 μW/cm^2). 53

Figure 3.4 Reaction rate constants of GO reaction in UV/free chlorine system under different pH and the effect of dissolved oxygen and quenching agent *t*-BuOH (200 mM) 55

Figure 3.5 Free chlorine concentration during the GO/UV/free chlorine reaction. 100 ppm free chlorine was added at time 0, 120 and 210 min..... 58

Figure 3.6 First order reaction rate constant of free chlorine decay under UV irradiation with and without GO in the system, for 3 cycles..... 58

Figure 3.7 TEM images of GO and product with free chlorine under UV irradiation (2000 μW/cm^2) for 2 hours. (a) GO, (b) with 100 mg/L free chlorine at pH 5, (c) with 150 mg/L free chlorine at pH 5, (d) with 200 mg/L free chlorine at pH 5. All scale bars are 200 nm. 59

Figure 3.8 Raman spectra of GO and product. A: GO before and after reaction with 200 mg/L free chlorine at pH 5 under UV irradiation (2000 μW/cm^2). B: D/G ratio of GO after reaction with free chlorine at different pH levels under UV irradiation (2000 μW/cm^2) for 2 hours..... 60

Figure 3.9 FTIR spectra of GO reactions at pH 5 with 100 mg/L and 200 mg/L free chlorine under UV irradiation (2000 μW/cm^2) for 2 hours. 61

Figure 3.10 XPS spectra of (a) GO and (b) GO after reaction with 200 mg/L free chlorine at pH 5 under UV irradiation (2000 μW/cm^2) for 2 hours. 62

Figure 3.11 Total organic carbon after reaction with free chlorine under UV irradiation in open system. A: TOC after reaction with free chlorine under UV irradiation (2000 μW/cm^2) for 2 hours at different pH levels. B: Long-term study of TOC change for the reaction of GO with free chlorine at pH 5 under UV irradiation (2000 μW/cm^2). Additional 200 mg/L free chlorine was applied to the solution every 2 hours. 63

Figure 3.12 Product molecular weight distribution from filtration. GO (50 ppm) with 200 ppm free chlorine under light irradiation at pH 5. 65

Figure 3.13 MALDI-TOF-MS results of GO after reaction with 200 ppm free chlorine at pH 6 under light irradiation (2000 μW/cm^2) for 2 hours, with possible product chemical structures based on the m/z value. 66

Figure 3.14 Carbon mass balance between the gas phase and liquid phase in closed system. Reaction were carried with 50 mg/L GO at pH 5 with 400 (10A), 200 (10B) and 100 (10C) mg/L free chlorine under UV irradiation (2000 μW/cm^2). The solid symbols represent the carbon remaining in the liquid phase (TOC and liquid CO_2) and the empty symbols represent the carbon in gas phase (CO_2) for each free chlorine concentration. 10D: control experiments (1) in dark with 400 mg/L free chlorine and (2) without free chlorine under UV irradiation (2000 μW/cm^2). 67

Figure 3.15 Proposed reaction mechanism for GO in the presence of free chlorine and light irradiation. 68

Figure S3.1 Calibration curve of free chlorine concentration measurement by DPD colorimetric method. 71

Figure 4.1 Carbon dissolved in the aqueous solution after 2 hours reaction of GO membrane with different concentration (0, 10, 50, 100 mg/L) of free chlorine at pH 7, both in dark and under light irradiation (2000 μW/cm^2) 79

Figure 4.2 XPS survey scan (A) and fine scan of C 1s (B) of original graphene oxide membrane 80

Figure 4.3 XPS survey scan (A) and C 1s scan (B) of the graphene oxide membrane after 2 hours reaction with free chlorine (100 mg/L) at pH 7 under light irradiation (2000 μW/cm^2). 82

Figure 4.4 Average carbon oxidation state change (from XPS C1s scan) of the graphene oxide membrane after reaction with different concentration of free chlorine (0, 10, 50, 100 mg/L) in dark and under light irradiation (2000 μW/cm^2) for 2 hours at pH 7. 83

Figure 4.5 Carbon oxidation state change (from XPS C 1s scan) of graphene oxide transformation by free chlorine (10, 50 100 mg/L) under light irradiation (2000 μW/cm^2) for 2 hours under different pH conditions (5, 7, 9)..... 84

Figure 4.6 Carbon oxidation state change (from XPS C1s scan) of graphene oxide membrane after reaction with free chlorine (10 mg/L and 100 mg/L) at pH 7 under light irradiation (2000 μW/cm^2) for 2 hours and 4 hours..... 85

Figure 4.7 AFM image of the original graphene oxide membrane..... 85

Figure 4.8 Surface roughness of graphene oxide membrane after reaction with free chlorine (10 mg/L and 100 mg/L) at pH 7 under light irradiation (2000 μW/cm^2) for 2 hours and 4 hours.... 86

Figure 4.9 Water flux of the graphene oxide membrane before and after the reaction with free chlorine (10 mg/L and 100 mg/L) at pH 7 under light irradiation (2000 μW/cm^2) for 2 hours and 4 hours..... 87

Figure 5.1. XPS (C 1s) of the 3 types of GO before adsorption. (a) low oxidized GO-1 (b) medium oxidized GO2 (c) high oxidized GO-3 97

Figure 5.2 Adsorption isotherm for Ce^{3+} on three types of GO at pH 7, with isotherm fitted by Langmuir model. 101

Figure 5.3 Adsorption isotherm for La^{3+} on three types of GO at pH 7, fitted with Langmuir model 101

Figure 5.4 Sorption kinetics of Ce and La on GO-3 at initial pH of 7 and pH change during the 48 hours adsorption period 104

Figure 5.5 Species diagram of aqueous Ce(III) and La(III) at different pH without precipitation and redox reaction. Calculation based on the complexation of Ce^{3+} and La^{3+} with OH^- only. .. 106

Figure 5.6 Ce^{3+} (A) and La^{3+} (B) adsorption capacity of three types of GO (as stated in the Experimental section) under different pH level (pH 3 – 7). Capacity was calculated based on the q_e in Langmuir isotherm. 107

Figure S5.1. Adsorption isotherm for Ce^{3+} on 3 types of GO at pH 7, fitted with Freundlich model 110

Figure S5.2. Adsorption isotherm for La^{3+} on 3 types of GO at pH 7, fitted with Freundlich model 110

Figure S5.3 GO-1 adsorption isotherm for Ce^{3+} at different pH level (3 – 7), fitted with Langmuir isotherm 111

Figure S5.4 GO-1 adsorption isotherm for La^{3+} at different pH level (3 – 7), fitted with Langmuir isotherm 111

Figure S5.5 GO-2 adsorption isotherm for Ce^{3+} at different pH level (3 – 7), fitted with Langmuir isotherm..... 112

Figure S5.6 GO-2 adsorption isotherm for La^{3+} at different pH level (3 – 7), fitted with Langmuir isotherm..... 112

Figure S5.7 GO-3 adsorption isotherm for Ce^{3+} at different pH level (3 – 7), fitted with Langmuir isotherm..... 113

Figure S5.8 GO-3 adsorption isotherm for La^{3+} at different pH level (3 – 7), fitted with Langmuir isotherm..... 113

Figure S5.9 Ce^{3+} adsorption on GO-1 at pH 5 with increasing ionic strength (0, 1, 10, 100, 600 mM), fitted with Langmuir isotherm 114

Figure S5.10. La^{3+} adsorption on GO-1 at pH 5 with increasing ionic strength (0, 1, 10, 100, 600 mM), fitted with Langmuir isotherm 114

Figure S5.11 Ce^{3+} adsorption on GO-1 at pH 7 with increasing ionic strength (0, 1, 10, 100, 600 mM), fitted with Langmuir isotherm 115

Figure S5.12 La^{3+} adsorption on GO-1 at pH 7 with increasing ionic strength (0, 1, 10, 100, 600 mM), fitted with Langmuir isotherm 115

Figure S5.13 Ce^{3+} adsorption on GO-2 at pH 5 with increasing ionic strength (0, 1, 10, 100, 600 mM), fitted with Langmuir isotherm 116

Figure S5.14 La^{3+} adsorption on GO-2 at pH 5 with increasing ionic strength (0, 1, 10, 100, 600 mM), fitted with Langmuir isotherm 116

Figure S5.15 Ce^{3+} adsorption on GO-2 at pH 7 with increasing ionic strength (0, 1, 10, 100, 600 mM), fitted with Langmuir isotherm 117

Figure S5.16 La^{3+} adsorption on GO-2 at pH 7 with increasing ionic strength (0, 1, 10, 100, 600 mM), fitted with Langmuir isotherm 117

Figure S5.17 Ce^{3+} adsorption on GO-3 at pH 5 with increasing ionic strength (0, 1, 10, 100, 600 mM), fitted with Langmuir isotherm 118

Figure S5.18 La^{3+} adsorption on GO-3 at pH 5 with increasing ionic strength (0, 1, 10, 100, 600 mM), fitted with Langmuir isotherm 118

Figure S5.19 Ce^{3+} adsorption on GO-3 at pH 7 with increasing ionic strength (0, 1, 10, 100, 600 mM), fitted with Langmuir isotherm 119

Figure S5.20 La^{3+} adsorption on GO-3 at pH 7 with increasing ionic strength (0, 1, 10, 100, 600 mM), fitted with Langmuir isotherm 119

List of Tables

Table 2.1 Optical band gap of graphene oxide with different oxidation state 31

Table 2.2 Raman spectra data for 3 types of GO 33

Table 2.3 Hydrodynamic diameter and zeta potential of GO at pH 7 36

Table 2.4 Critical coagulation concentration of GO with Na^+ and Mg^{2+} 39

Table S2.1 XPS result for temperature effect on synthesized graphene oxide, other conditions are: reaction time of 2 hours in stage 1 and 60 min in stage 2, oxidant ratio of 3:1 and sonication for 2 hours. 41

Table S2.2. XPS result for reaction time effect on synthesized graphene oxide, other conditions are: 30 °C in stage 1 and 60 °C in stage 2, oxidant ratio of 3:1 and sonication for 2 hours. 42

Table S2.3. XPS result for oxidant ratio effect on synthesized graphene oxide, other conditions are: 30 °C in stage 1 for 2 hours, 60 °C in stage 2 for 60 min, and sonication for 2 hours..... 43

Table 3.1 Reaction rate constants under different pH with GO in different size..... 56

Table S3.1 Carbon mass conservation for 400 mg/L free chlorine reaction (sealed system)..... 72

Table S3.2 Carbon mass conservation for 200 mg/L free chlorine reaction (sealed system)..... 72

Table S3.3 Carbon mass conservation for 100 mg/L free chlorine reaction (sealed system)..... 73

Table S4.1 XPS result of graphene oxide membrane after 2 hours reaction with free chlorine at pH 7 under light irradiation (2000 $\mu W/cm^2$) 88

Table S4.2 XPS result of graphene oxide membrane after 2 hours reaction with free chlorine at pH 7 in dark condition 88

Table S4.3 XPS result of graphene oxide membrane after reaction with free chlorine (10 mg/L, 50 mg/L and 100 mg/L) under light irradiation for 2 hours under different pH conditions. 89

Table S4.4 XPS result of graphene oxide membrane after reaction with free chlorine (10 mg/L and 100 mg/L) at pH 7 under light irradiation for 2 hours and 4 hours..... 89

Table 5.1. XPS result (C 1s scan) of the GO before and after adsorption with Ce and La 98

Table 5.2. Hydrodynamic diameter and zeta potential of GO at pH 7 99

Table 5.3. Isotherm model fit result of Ce adsorption on GO at pH 7..... 102

Table 5.4. Isotherm model fit result of La adsorption on GO at pH 7..... 102

Table 5.5 Hydrolysis constants of Ce^{3+} and La^{3+} with OH^{-}.[216, 217] 105

Table 5.6 Adsorption capacity of Ce on GO under different ionic strength..... 108

Table 5.7 Adsorption capacity of La on GO under different ionic strength 109

Table S5.1 Langmuir model parameters for Ce^{3+} adsorption on GO 120

Table S5.2 Langmuir model parameters for La^{3+} adsorption on GO..... 120

Table S5.3 Langmuir model parameters for Ce^{3+} adsorption on GO with presence of NaCl at pH 5..... 121

Table S5.4 Langmuir model parameters for Ce^{3+} adsorption on GO with presence of NaCl at pH 7..... 121

Table S5.5 Langmuir model parameters for La^{3+} adsorption on GO with presence of NaCl at pH 5..... 122

Table S5.6 Langmuir model parameters for La^{3+} adsorption on GO with presence of NaCl at pH 7..... 122

Acknowledgments

First, I would like to express my deep and sincere gratitude to my Ph.D. advisor, Prof. John D. Fortner for his excellent guidance and continuous support during this 6 years period. His patience, motivation and immerse knowledge helped me through each difficulties I met on my way of pursuing my scientific dream. Prof. Fortner initiated my research projects while allowing me freedom to explore the issues of interest, which greatly motivated me to complete my research projects to the best of my knowledge.

I would like to thank Prof. Young-Shin Jun, Prof. John Gleaves, Prof. Marcus Foston, and Prof. Erik Henriksen for participating in my thesis committee. Their insight comments and thoughtful suggestions reshaped my research and helped me develop capabilities of creative thinking as an independent researcher. The quality of this research has been significantly improved and I owe this to their precious time and effort being in my thesis committee.

I would like to acknowledge National Science Foundation's CAREER Award (CBET #1454656) and the Mindlin Foundation for their generous support relating to this work. The instrument used in this research are maintained by Nano Research Facility (NRF) at Washington University in St. Louis, a member of the National Nanotechnology Infrastructure Network (NNIN), which is supported by the National Science Foundation under Grant No. ECS-0335765.). Also thanks to Institute of Materials Science and Engineering and Mechanical Engineering and Materials Science Department in Washington University in St. Louis. Without their support in instrumentation, this research could not be completed.

I would like to acknowledge my lab members, besides Prof. Fortner, for their support and generosity during my research. Special thanks to my collaborators: Dr. Wenlu Li, Dr Jiewei Wu, Dr. Yi Jiang, Dr. Seung Soo Lee, Dr. Kelsey Haddad, Changwoo Kim, Qingqing Zeng, Anushree

Ghosh and Junseok Lee. This research could not be completed without their support and I benefited a lot from our discussions about research ideas and approaches.

This work is also supported by McDonnell International Scholars Academy in Washington University in St Louis. Tremendous thanks to them for providing financial support for my Ph.D., as well as great social events and opportunities to networking with scholars in different department with various cultural and scientific background. My communication skills and confidence grew significantly together with my vision via those wonderful experience. Special thanks to Director James Wertsch together with all the staff in McDonnell International Scholar Academy for their time and effort organizing events, caring for us and invaluable advices on career development.

I would like to thank all my friends and staff in Department of EECE for their help and support.

Last but not least, I would like to thank my parents and my wife, Yatian Li, for their unconditional love and support. Without them I could never achieve what I have today.

Siyuan An

Washington University in St. Louis

December 2018

ABSTRACT OF THE DISSERTATION

Graphene Oxides in Water: Characterization, Reactivity, and Application

by

Siyuan An

Doctor of Philosophy in Energy, Environmental & Chemical Engineering

Washington University in St. Louis, 2018

Professor John Fortner, Chair

Recently discovered, graphene and graphene oxide materials have drawn considerable research attention due to outstanding and novel properties, which underpin wide material potential for a number of advanced applications including supercapacitors, solar cells, sensors, catalysts, semiconductors, sorbents, and membranes, among others. Graphene oxides (GO), which are considered as a family of oxidized graphene materials (derivatives), is a key precursor to the synthesis of free-standing graphene via oxidation-exfoliation-reduction pathways. GO properties depend on the synthesis routes/conditions (i.e. derivatization), including partially maintaining graphene (i.e. sp2) properties. Further, oxygen-containing functionalities (epoxy, hydroxyl, carbonyl, and carboxyl groups) render GO hydrophilic – and correspondingly stability in water, thus underpinning (aqueous-based) transport and even reactivity. Juxtaposed with aforementioned application potential, the inadvertent implications of GO, and corresponding daughter products, in environmental systems remain largely unknown. For successful aqueous applications, it is necessary to overcome two fundamental challenges: 1) control of the functional group

quantity/type via synthesis process, and 2) understand the behavior (e.g. fate and transport, application) of the material(s) as a function of surface chemistry and reactivity.

In this work, classic graphene oxide synthesis is systematically explored and evaluated, including synthesis temperature, reaction time, oxidant ratios, and sonication time, with resulting material properties described, For this matrix, materials are characterized with regard to aqueous stability and spectral analyses including transmission electron microscopy (TEM), UV-vis spectroscopy, X-ray photoelectron spectroscopy (XPS), Raman spectroscopy, thermogravimetric analysis (TGA), total organic carbon analysis (TOC), and Fourier transform infrared spectroscopy (FTIR). Additionally, the reactivity and transformation of these materials in the presence of free chlorine, a common oxidant, under light irradiation is also described. Specifically, reaction kinetics and mechanism(s) are systematically evaluated as a function of pH, dissolved oxygen, and initial size of graphene oxide (coupons). For these reactions, partially mineralization is confirmed via direct CO_2 detection and carbon mass balance. Final product(s) are described via TEM, FTIR, XPS, Raman spectroscopy, and mass spectrometry (MS). Further, we evaluated and describe graphene oxide applications, including as a platform sorbent for rare earth metals, focusing on cerium(III) and lanthanum(III). For these, graphene oxide functionality (both function group type and quantity), solution pH, and ionic strength are systematically evaluated and described towards sorption optimization. Lastly, graphene oxide membranes are explored with regard to surface reactivity (i.e. exposure to free chlorine), under both dark and light irradiation conditions, as it relates membrane stability and (separation) performance for related water treatment processes.

Chapter 1: Introduction

1.1 Dissertation Organization

The dissertation begins with identifying key scientific and engineering issues to be addressed, followed by a review of the current research body with respect to the aforementioned issues. Chapter 2 focuses on the synthesis of graphene oxide – specifically evaluating key factors, such as temperature, reaction time, oxidant ratio and sonication conditions. This also includes extensive characterization, including method development, using transmission electron microscopy, UV-vis spectroscopy, X-ray photoelectron spectroscopy, Raman spectroscopy, thermogravimetric analysis, and Fourier transform infrared spectroscopy, among other techniques. In Chapter 3 the transformation of graphene oxide by free chlorine, a common oxidant and disinfectant, under light irradiation is described. For this, reaction kinetics were modeled and the effect of pH, dissolved oxygen, size of initial coupon were explored. Products were characterized by UV-vis spectroscopy, TEM, FTIR, TOC, Raman spectroscopy, mass spectrometry, and XPS. Partial mineralization was confirmed and carbon mass balance between the gas phase and aqueous was well established. This work served as a guide for Chapter 4, which details the effect of free chlorine dose, pH, and exposure time on GO membrane chemical stability, carbon oxidation state, water flux, and surface roughness. In Chapter 5, graphene oxide materials with different quantities/types of functional groups (taken material libraries established in Chapter 2) were applied towards aqueous-based cerium and lanthanum adsorption. Adsorption isotherms were established for all conditions tested. The effects of functional group quantity, type, pH, and ionic strength on the adsorption capacity are described. Finally, Chapter 6 summarizes the key findings and contributions in this dissertation. The implications of the

findings are discussed. Based on the discussions, recommendations for future research are proposed.

1.2 Background

1.2.1 Graphene and Derivatives

Graphene is an allotrope of carbon that takes the form of a two-dimensional, hexagonal lattice with sp^2-hybridyzed carbon atoms at each vertex. Graphene can also been considered as a parent material of other graphitic-like carbon forms including fullerene, carbon nanotubes and graphite as shown in Fig. 1.1.[1] Since 2004, when Novoselov and co-researchers identified isolated graphene[2], it has gained considerable research interest. Graphene exhibits a number of interesting material properties, including some approaching theoretical material limits[3], including room-temperature electron mobility[4], Young's modulus[5], thermal conductivity[6], optical absorption[7], impermeability to gases[8], and the ability to sustain extremely high electron current densities[9]. Based on these and other properties, graphene is poised to be applied in a number of advanced applications such as supercapacitors[10-12], solar cells[13-15], sensors[16-18], catalysts[19-21], semiconductors[22-24], and other functional nanocomposites[25-27]. Via chemical vapor deposition (CVD), high quality graphene could be synthesized but in very limited quantity.[28] Although the development of large(er) scale graphene is still largely at the R&D stage, the global graphene market hit USD 23.7 USD in 2015, and is projected to grow at a CAGR of 36.7% until 2025[29], with most demand in semiconductor electronics, energy (mainly to batteries) and composite material industries[30]. However, the wide application potential requires large scale production of graphene material at low cost[31].

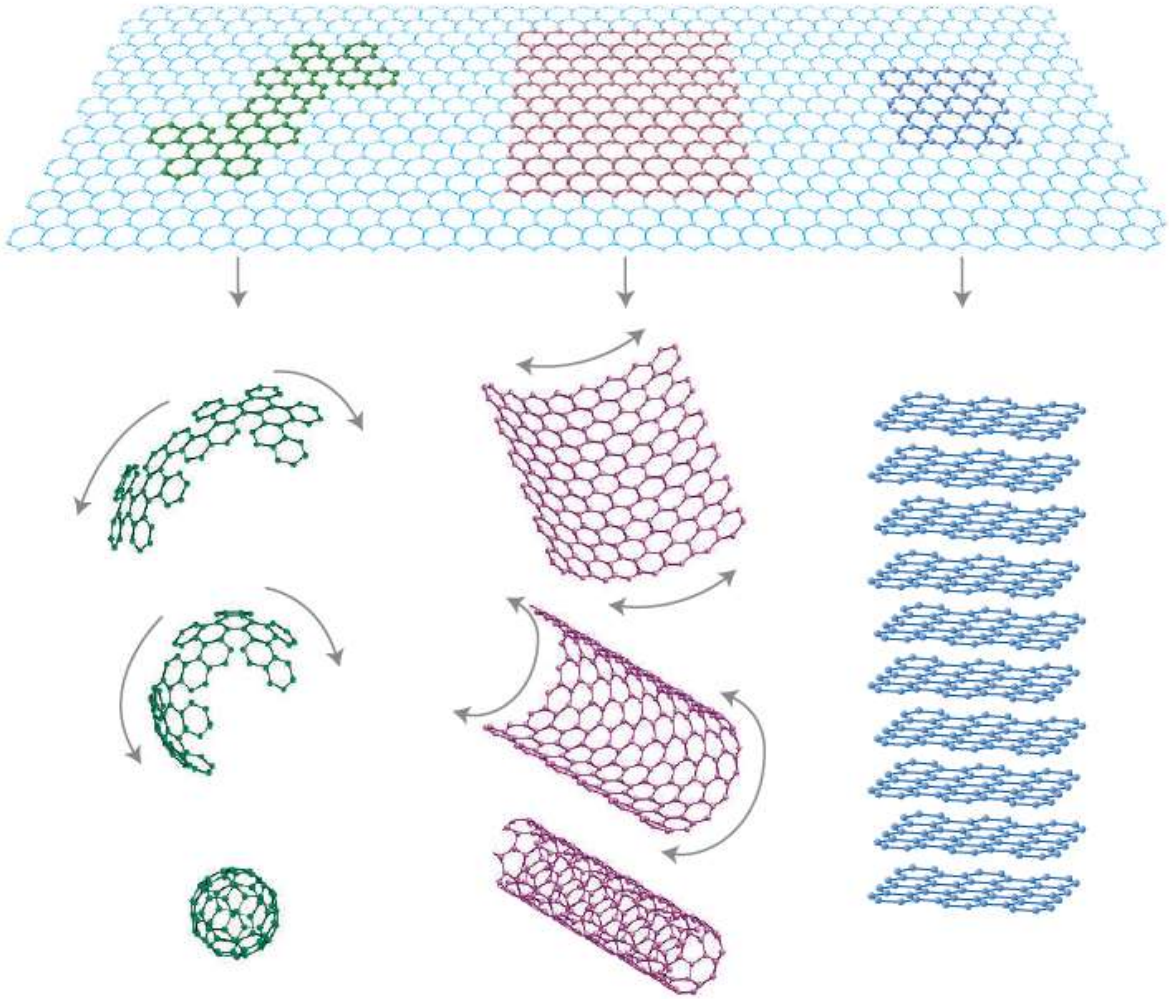

Figure 1.1 Graphene as parent of all graphitic forms: fullerene, carbon nanotube and graphite[1]

1.2.2 Graphene oxide

Graphene oxide (GO) is a key precursor to large scale synthesis of free-standing graphene[32]. GO has oxygen functionality on both the basal plane (typically as epoxy and hydroxyl groups) and coupon edges (as carbonyl and carboxyl groups)[33], which are several layers to single-layer thin and stable in water[34]. Also it serves as a starting material for large scale production of reduced graphene oxide (rGO), which is suitable for many application as it retains a number of graphene properties[35]. Currently, graphene oxide(s) (GO) materials account for >30% of the global graphene market share[29, 36] as advances in GO processing allow for a number of potentially

scalable routes to achieve mass production of chemically modified graphene – while also having broad applications in polymer composites, supercapacitors[37-39], sensors[40-42], catalysts[43-45], membranes[46-48], and biomedical materials, among others[49]. The process of oxidizing graphite and exfoliating it in an aqueous solution, typically done via the modified Hummers method, yields graphene oxide as several, or even single layers, in relatively large (gram - kilogram scales) quantities[34]. Oxygen-containing groups on the graphene plane (e.g. epoxy, hydroxyl, carbonyl) are more hydrophilic than the sp^2 carbon clusters, and also increase the space between graphene layers, thus allowing for facile solvent-exfoliation[33]. Adding reducing agents, such as hydrazine[50-52], into the system or thermally reducing oxygen-containing groups[33, 53, 54], GO can then be reduced (back to sp^2 carbons), (re)gaining properties of 2-D graphene, which makes GO an important precursor for potential scaled production of graphene itself[31]. By controlling the level of reduction, the field requirements for material applications can be achieved – i.e. the materials can be specifically tailored for functionality. Additionally, GO itself has interesting properties other than large surface area and outstanding electron properties. The hydrophilic oxygen-containing groups facilitate enhanced water stability water, allowing for potential (suspended) aqueous applications. Also the oxygen groups enable graphene oxide to be functionalized via covalent bonding or physical interactions, making it a building block for versatile functional materials[55]. This also allows for further modification(s), such as solution-based conjugation with polymers or metal/metal oxides[49, 56]. Recently, there have been interesting reports regarding graphene oxide itself or modified with other materials acting as novel sorbents[57-59] and catalysts[60-63].

1.2.3 Carbon Atom Hybridization

In chemistry, orbital hybridization is the concept of mixing atomic orbitals into new hybrid orbitals (with different energies, shapes, etc., than the component atomic orbitals) suitable for the paring of electrons to form chemical bonds in valence bond theory[64]. Carbon atoms could form four covalent bonds, like methane which has four bonds with hydrogen atoms. The four equivalent orbitals come from the carbon 2s and 2p orbitals, with each bond composed of ¼ of 2s orbital and ¾ of one of the p orbitals and the new orbital is called sp^3 orbital, as shown in Figure 1.2[65]. This process of orbital mixing is called hybridization this carbon atom would be sp^3 hybridized[65]. As electrons repel each other, the four orbitals will distribute as tetrahedron to minimize the total energy. This is applied when carbon atoms are bonded with oxygen atoms in C-O groups or with hydrogen atoms in C-H.

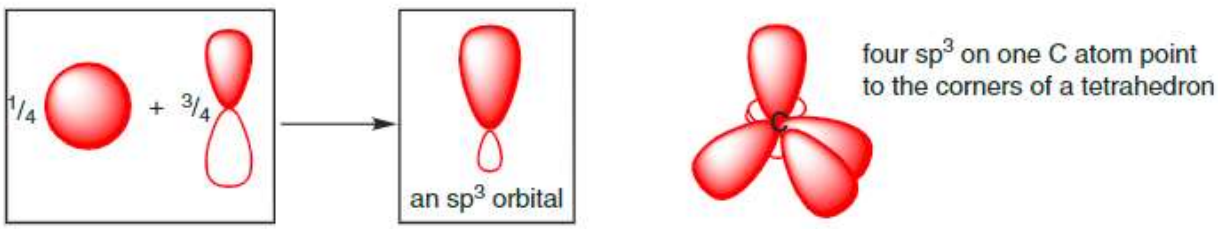

Figure 1.2 Carbon atom with sp^3 hybridized orbital[65]

Then for double bonds, another set of hybridized orbitals are described. Like in ethylene, besides the two orbitals taken by the C-H bond, there are 2s orbital and two 2p orbitals for hybridization, which is called sp^2 hybridized. These orbitals have 1/3 of the 2s orbital and 2/3 of the 2p orbitals, as shown in Figure 1.3[65]. The overlap of the 2 sp^2 orbitals form the π bond above and below the plane. This is applied when carbon atoms are bonded with carbon atoms in C=C or oxygen atoms in C=O.

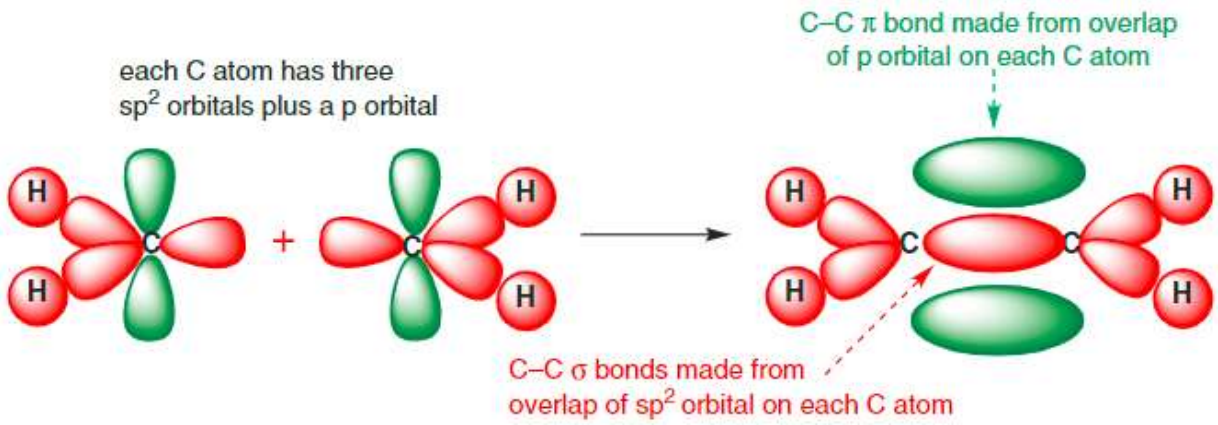

Figure 1.3 Carbon atom with sp^2 hybridization[65]

Also for the acetylene with triple bond, i.e., C≡C, the sp hybridization is formed with one 2s orbital and one 2p orbital to form two new orbitals, each with ½ 2s orbital and ½ 2p orbital[65]. Then the two sp hybrid orbitals overlap and form two mutually perpendicular π bonds, as shown in Figure 1.4[65].

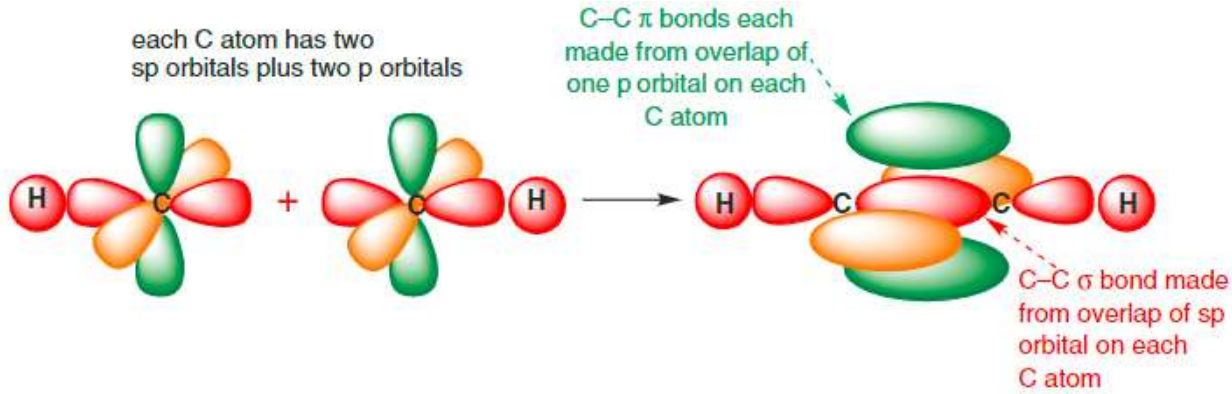

Figure 1.4 Carbon atom with sp hybridization[65]

In graphene, the conjugation of sp^2 orbital would merge between the aromatic rings and form the π system, as shown in Figure 1.5[66]. The electron delocalization would give graphene extraordinary electron mobility and conductivity[67].

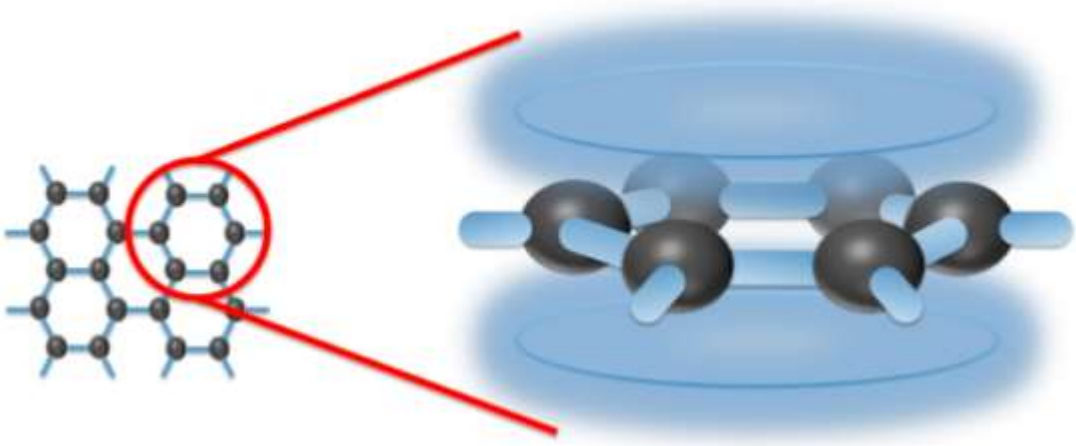

Figure 1.5 Graphene oxide electron delocalization of sp^2 hybridized orbitals[66]

1.2.4 Graphene Oxide Environmental Behavior and Potential Risk

Given the promising application potential, a significant amount of research has been conducted focused on graphene and derivative materials in various fields, as mentioned above. However, environmental based reactions of graphene / graphene derivatives with ubiquitous reactants / system (UV irradiation, common oxidants, reductants microorganisms, etc.) have only recently been explored and described. While the exceeding low stability of graphene leads to rapid aggregation/precipitation in aqueous solutions, graphene oxide, due to hydrophilic functionality, has the potential to disperse into water volumes, and thus interacting with a number of systems. It should be noted that, GO has been found to be relatively toxic compared to other, different graphene materials[68-70]. Thus the environmental fate and transport of graphene oxide nanoparticles should be clearly understood to better facilitate the application of graphene oxide, for the regulation, treatment, and/or recycle of the material.

1.2.4 Graphene Oxide Membranes

Even though water is considered as renewable resource, it was predicted that one-third of the global population will suffer from chronic water shortage issues[71]. Membrane-based water

treatment and purification technology has attracted great attention due to its advantages of easy-operation, energy efficiency and environmental friendliness[72]. Graphene oxide has shown notable potential in membrane-based applications, due to its mechanical strength, hydrophilicity and functional groups readily for chemical or physical modification[73]. Theoretical calculations indicated that graphene oxide physiochemical properties could increase the water permeability in desalination an order of magnitude higher than the conventional reverse osmosis[74]. In addition, graphene oxide was incorporated into the membrane to enhance the antimicrobial and anti-fouling properties of the membrane, as well as roughness, mechanical strength, electronegativity, hydrophilicity, due to its uniform dispersion, accelerated charge transfer and cytotoxic effect to the microbials[75-78]. Zhao et al prepared microfiltration membrane by blending PVDF and graphene oxide and showed sustained permeability, low cleaning frequency and anti-fouling property[78]. Saraswathi et al. explored graphene oxide incorporation in the poly(amide imide) (PAI) membrane and showed the improved water flux and protein rejection[79]. Bernstein et al. used zwitterion polymer and graphene oxide together for the modification of PES membrane and demonstrated the anti-fouling property[80]. Wang et al applied interfacial polymerization to incorporate graphene oxide into the polyamide active layer of thin-film composite membranes for organic compounds removal with improved anti-fouling property[81]. Liu et al reported fabrication of polyelectrolyte assembled functionalized graphene oxide membrane and demonstrated the high performance in dye/salt separation with water flux of 52.1 L/(m*h*bar)[82]. Zhang et al incorporated oxidized carbon nanotubes and graphene oxide into the PVDF casting solution and the synthesized membrane showed higher porosity and water flux, with anti-fouling property[83]. Lv et al synthesized graphene oxide-cellulose composite to blend into PVDF micro-filtration membrane, which exhibited high wettability, low protein and polysaccharides

adsorption, high permeability and anti-fouling property in long-term operation[84]. By modification of graphene oxide, the hydrophilicity of membrane could be tuned to fit different application requirements. Mahmoudian et al. chemically modified graphene oxide with hydrophobic polymethylmethacrylate and deposited on poly(ether sulfone) (PES) membrane for separation of salts, dyes and heavy metals[85]. Karim et al blended graphene oxide with PES in the casting solution and the synthesized membrane showed increased water flux and rejection of bovine serum albumin (BSA) of 97% compared to the PES membranes[75]. Kang et al. used sulfonated graphene oxide to functionalize polysulfone membrane and achieved high water flux and BSA rejection (over 98%)[86]. Wu et al blended graphene oxide with TiO_2 for membrane fabrication and showed high water flux (531 L/(m^2 h bar)) and application on oil/water separation[87]. Chen et al. synthesized sandwich-structured polyamide-graphene oxide-polyamide membrane intercalated with TiO_2 nanoparticles and showed water flux of 13.77 L/(m*h*bar) and 92% rejection for methylene blue[88]. Dai et al. synthesized poly(lactic acid) (PLA) electrospun membrane immobilized with zeolitic imidazole framework/graphene oxide hybrid and demonstrated the increased hydrophilicity, mechanical strength and photocatalytic degradation of methylene blue[89]. The previous work in our lab also showed great performance of graphene oxide membrane in water purification[90].

1.2.5 Rare Earth Metals

Lanthanides, commonly referred to as rare earth elements, are crucial and extensively used in applications such as health care, electronics, metallurgy, catalyst, magnets, and phosphors[91]. The rare earth metal market rises dramatically in the past years, increasing by a factor of 17 from 1964 to 1997 and by a factor of 20.5 from 1997 to 2007[91]. Rare earth metals are not particularly 'rare' in terms of abundance. Their average abundance in the earth crust is 60 – 68 ppm for Ce

and 32 – 39 ppm for La, about the same level as zinc and copper[92]. However, their similar chemical properties kept them rarely separated for many years[93]. Among all the rare earth metals, cerium makes up 45% of the market and lanthanum makes up for 39%, while the rest of the rare earth metals make up for the remaining 15%[94]. Specifically, the catalysis application consisted of 66% lanthanum oxide and 32% cerium oxide, being 72% for fluid cracking and 28% for automobile catalytic converters[91]. Cerium and lanthanum are crucial components in the catalyst for petroleum cracking and refining[95, 96]. Cerium oxide is used in catalytic converters in cars, enabling them to run at high temperatures, for oxidation of CO and NO_x emissions in the exhaust gases, and is required by Federal law to be installed in nearly all gasoline and diesel fueled vehicles in the United States[97].

1.3 Objectives

Overall, research described in this thesis is organized as an ordered matrix of material synthesis and environmentally relevant reactions, followed by GO applications in water treatment membranes and rare earth metal adsorption. There are four overarching research objectives, as follows:

Objective 1: Systematically explore key variables in GO synthesis processing such as temperature, reaction time, oxidant ratios, and sonication time as they relate to material properties.

Objective 2: Describe the reaction kinetics and mechanisms of graphene oxide reactivity with free chlorine under UVA irradiation. Quantify the effects of pH, dissolved oxygen, and initial coupon size for these reactions. Identify and characterization the key products, such as CO_2 and other small fragment molecules.

Objective 3: Explore chemical stability of the graphene oxide membrane in the presence of free chlorine and light irradiation. Study the effects of pH, free chlorine dosem and exposure time on the water flux, surface roughness, and surface carbon oxidation state.

Objective 4: Investigate the application of graphene oxide towards rare earth metal (cerium and lanthanum) adsorption and separation. Describe sorption isotherms over a range of system considerations and variables including graphene oxide functional groups, system pH, and ionic strength. Propose an adsorption mechanism based on the results.

To meet these objectives, graphene oxide synthesis process was first studied and the set of characterization methods was established. By controlling the parameters during the synthesis, graphene oxide with different quantities of functional groups were synthesized for later studies. The reaction with free chlorine under light irradiation was then investigated which also provided the guiding hypotheses for our experiments evaluating the graphene oxide membrane stability and performance upon chlorine exposure. Lastly, graphene oxide materials with different surface chemistries were explored in detail for rare earth metal adsorption and separation.

Chapter 2 Graphene Oxide Synthesis and Characterization

Abstract

In this chapter, we describe synthesis processing of graphene oxide under different conditions, exploring the effects of temperature, reaction time, oxidant ratio, and sonication time. Average oxidation state of carbon and carbon yield were chosen as the two criteria to evaluate produced (product) graphene oxide materials. It was observed that as temperature increased, the oxidation state and yield of GO also increased. Reaction time and oxidant ratio not only increases the oxidation state of GO, but also has a pronounced effect on material yields. As a function of reaction conditions, graphene oxide materials were characterized and described via a suite of techniques, including transmission electron microscopy, UV-vis spectroscopy, X-ray photoelectron spectroscopy, Raman spectroscopy, thermogravimetric analysis, and Fourier transform infrared spectroscopy.

2.1 Introduction

Currently, most graphene oxide and reduced graphene oxide applications use a version of the Hummers method for graphene oxide synthesis as it is relatively simple, scalable, and fairly green, compared to other GO synthesis methods[34]. The modification on Hummers method differs from one report to another and the effect of the modifications on the properties of graphene oxide remain outstanding[98, 99]. Even though the Hummers method is widely used in GO synthesis, the difference in reaction temperature, reaction time, oxidant ratio, and sonication time likely results in products with different properties, which has not been absolutely quantified and directly

compared in the literature. For example, the reaction temperature of graphene oxide synthesis reported range from 30 °C to 50 °C, with reaction time ranging from 1 hour to 3 hours[28, 31, 98, 100, 101]. Even for a sonication step(s), the time range vary from 15 min to 2 hours, and most reports fail to provide information about the time and power of the sonication, which could lead to varied redox reaction(s) of the product[98, 101-104]. This, among other variables, underscores difficulties when comparing the GO materials among different research groups and reports. Also, from an engineering perspective, it would be beneficial if we could control the quantity of functional group on the GO surface. Based on the most common method of graphene oxide synthesis, here we studied the factors during the synthesis process, including reaction temperature, reaction time, oxidant ratio, and sonication time. Research presented in this chapter aims to directly addressing these issues.

2.2 Materials and Methods

2.2.1 Materials

Graphite powder, sulfuric acid, potassium permanganate, and hydrogen peroxide solution were purchased from Sigma-Aldrich. All chemicals were reagent grade or higher and used without further purification, unless otherwise noted.

2.2.2 Graphene Oxide Synthesis

According to the standard Hummers method, there are two reaction stages for graphite oxidation with $KMnO_4$.[34] In stage 1, graphite powder and concentrated sulfuric acid (95 – 98%) is added into a beaker and cooled down to 0 °C with an ice bath. Potassium permanganate is then slowly added into the beaker while the temperature is adjusted to 30 °C. The oxidant ratio of $KMnO_4$ / graphite ratio of 3:1 w/w is standard. Next, the mixture is magnetically stirred for 2 hours and then diluted with milli-Q (>18 MΩ) water. The solution is then stirred for another 60 min while

the temperature is maintained at 60 °C. At the end of stage 2, hydrogen peroxide (H_2O_2, 30%) solution is slowly added into the beaker to terminate the reaction, until gas evolution ceased, also to reduce the residual permanganate to soluble manganese ions. The solution/suspension is then passed through 220 nm filter and washed with milli-Q water until solution pH reached 5 – 6, removing any excess salt. After drying in a vacuum chamber for 24 h, ca. 150 mg recovered solid was suspended in 200 mL milli-Q water (750 mg/L) and sonicated for 2 hours, respectively. The sonication energy input rate was 4,355 J/h. After centrifuge, the supernatant containing graphene oxide was collected as a stock solution and samples were then used for characterizations.

To evaluate reaction temperature, the following temperature matrix was designed: 10, 30, or 50 °C for stage 1 and 30, 60 or 90 °C for stage 2. All the other conditions were kept standard as described above. In some reports, the second stage is omitted[101], hence besides the temperature matrix, we also studied the reaction time effect with the stage 1 being 1, 2, 3 and 4 hours and stage 2 being 0, 30, 60, 90 and 120 min, with other conditions kept standard. For the oxidant ratio experiment, the ratio of 1:1, 3:1 and 5:1 were evaluated, with 3 types of reaction temperature set: 1) 10 °C in stage 1 and 30 °C in stage 2 (GO-1), 2) 30 °C in stage 1 and 60 °C in stage 2 (GO-2), and 3) 50 °C in stage 1 and 90 °C in stage 2 (GO-3). The other conditions were kept standard. The same set of three graphene oxide and sample names were also used in the characterization section.

The graphitic oxide synthesized at the standard conditions except for the sonication process was used to study the effect of sonication effect, including sonication time (1 – 6 hours) and sonication ratio (100 – 1500 mg/L). After centrifuge, the precipitate was usually disposed. However, it would be beneficial if we could gain some insight of the properties of the precipitate,

which could help to better understand the sonication process. Thus we took samples from both supernatant and precipitate for XPS characterization.

2.2.3 Characterization

For characterization section, three types of graphene oxide were chosen as described above. Transmission electron microscopy was performed on Tecnai G2 Spirit from FEI Company, operating at 120 kV. Sample solution was diluted and bath-sonicated before being dropped on to the copper grid and dried before measuring. X-ray photoelectron spectroscopy (XPS) could quantitatively describe the percentage of carbon atoms in GO with different oxidation states. The amount of function groups (oxygen groups) is critical in determining the properties of GO product. Three measurements at different positions were performed for each sample and the average value was calculated. The instrument was PHI 5000 Versa Probe II. The peaks were fit using a mixed fit of 80% Gaussian and 20% Lorentzian characters in the PHI Multipak software. Peak position calibration was carried out by aligning the C 1s peak (C-C/C=C) with its reference position at 284.8 eV, and a Shirley background subtraction was performed. Total organic carbon analysis (TOC) was used to measure the concentration of graphene oxide suspension, as carbon. All samples were diluted to the concentration of 5 – 50 ppm before measurement. It was performed by TOC-L TOC analyzer from Shimadzu, with ASI-L auto sampler, using potassium hydrogen phthalate as a carbon standard. 0.1 M HCl was applied to the sample to facilitate removal inorganic carbon from the system (as CO_2).

As the concern of production, yield of the GO is important to estimate the concentration of the stock solution and the production cost. Here we investigated the effects of sonication time and initial graphitic oxide concentration on the yield of the product graphene oxide. The yield

was calculated based on the Total organic carbon analysis (TOC) and XPS data of the supernatant after centrifuge as followed:

$$yield = \frac{TOC}{[graphitic\ oxide]} \times \frac{C/O}{1 + C/O}$$

where graphitic oxide concentration was calculated by the mass added into water divided by the volume (200 mL throughout this work). Note that the mass of graphitic oxide was converted to the mass of carbon by the coefficient of C/O ratio of the graphitic oxide from XPS data. So the yield here was actually carbon yield, not the mass yield.

UV-vis spectroscopy was performed on Varian Cary 50 Bio UV-Visible Spectrophotometer from Varian, Inc. at wavelength range of 200 – 800 nm with 0.5 nm step size. Raman spectrum was collected with a 514.5 nm laser excitation at 10% power focused on the sample using a 50x objective. The spectrum was collected from 1000 cm^{-1} to 2000 cm^{-1}. The solution was dropped onto silicon wafer substrates and dried in a vacuum for 24 h before measuring. The instrument was InVia Confocal Raman microscope from Renishaw.

Dynamic light scattering (DLS) was used to measure GO hydrodynamic diameter (173° backscatter, refractive index: 1.333)[105] and zeta potential (Smoluchowski model)[55]. All samples were measured at 25 °C for 5 cycles and each cycle consists of 5 measurements. For critical coagulation concentration measurement, NaCl or $MgCl_2$ of calculated concentration was added into the graphene oxide solution (10 mg/L, pH 7) and the diameter (D) changing was measured at 15 seconds interval for a 30 min period. The initial aggregation period was defined as the period from t_0 to the time when the D exceeded 1.5D[106]. The initial aggregation rate constant (k_a) is proportional to the initial rate of change for D[107]:

$$k_a \propto \frac{1}{N_0}\left(\frac{dD}{dt}\right)_{t\to 0}$$

where N_0 is the initial particle concentration. The attachment efficiency α was used to evaluate the aggregation kinetics and defined as the initial aggregation rate constant (k_a) normalized by the rate constant under diffusion-limited conditions ($k_{a,fast}$)[107]:

$$\alpha = \frac{k_a}{k_{a,fast}} = \frac{\frac{1}{N_0}\left(\frac{dD}{dt}\right)_{t\to 0}}{\frac{1}{N_{0,fast}}\left(\frac{dD}{dt}\right)_{t\to 0,fast}} = \frac{\left(\frac{dD}{dt}\right)_{t\to 0}}{\left(\frac{dD}{dt}\right)_{t\to 0,fast}}$$

So the attachment efficiency could be calculated based on the above equation and would be plotted with the Na^+ or Mg^{2+} concentration as the x axis. Finally the critical coagulation concentration was determined by the intersection of extrapolated lines from diffusion-limited regime and reaction limited regime[106].

Thermogravimetric analysis (TGA) was used to investigate the overall thermal stability and could give information on the quantity of the functional groups. The data was collected from room temperature to 1000 °C with 10 °C per minute rate under nitrogen atmosphere. The instrument was TGA Q5000 IR from TA Instruments. Fourier transform infrared spectroscopy was used to identify the functional groups on the graphene oxide. The sample was dried in vacuum chamber and mixed with KBr for pressing into plates. The spectrum was collected from 500 cm^{-1} to 4000 cm^{-1} with 1 cm^{-1} interval. The instrument was Thermo Nicolet NEXUS 470 FTIR from Thermo Scientific.

2.3 Results and Discussion

2.3.1 Reaction Temperature

For XPS spectra in Figure 2.1, the 284.8 eV peak was assigned to the sp^2 hybridized carbon atoms, the 286.6 eV peak was assigned to the mono-oxidized carbon (e.g. C-O, C-OH) and the 288.3 eV peak was assigned to the deoxidized carbon atoms (e.g. C=O)[108]. XPS results for synthesis done at different temperatures (Figure 2.1 with T1 for temperature in the first stage and T2 for temperature in second stage), we clearly observe that higher temperature leads to more oxidized graphene oxide in both stages, with lower C-C/C=C percentage, as well as lower C/O ratio and higher C-O, C=O percentage (shown in Supporting Information). At temperature of 10 °C and 30 °C, the least oxidized graphene oxide we synthesized had C-C/C=C percentage of 56.33%, while at temperature of 50 °C and 90 °C, products have a C-C/C=C percentage of 45.21%. As the oxidation reaction is endothermic process, an increase in temperature leads to higher extent of graphite oxidation. One thing to note here is that the temperature of the first stage cannot technically be higher than 60 °C, as there is an explosion danger due to the fast initial reaction rate. This is also the reason for cooling down the graphite-sulfuric acid mixture to 0 °C with an ice bath before slowly adding in potassium permanganate. The yield change with the synthesis temperature is summarized in Figure 2.2 and shows that temperature increase also led to enhanced yield, which is due to the higher quantity of functional groups to facilitate the exfoliation process. At temperature of 10 °C and 30 °C, the yield was 33.9% and after the temperature increased to 50 °C and 90 °C, the yield increased to 65.4%.

Interestingly, during the second stage of the reaction (after diluting with water), if the temperature was 90 °C, there would is no gas generated by the addition of H_2O_2, indicating that all the permanganate was consumed. This is also observed when the temperature of the first stage

was 10 °C. We suspect this has to do with the viscosity in the reaction mixture was being relatively high, becoming even higher as reaction progressed. Mass transport could also be a limiting factor –higher temperature applied did not solve the problem as water is also evaporating, thus leading to higher viscosities. By observation, the mixture solidified at the end of 3 hours when the temperature was 30 °C or higher. However, after diluting with water, the mass transport limits appear to be overcome and higher temperature yields faster reaction rates, resulting in all the permanganate to be reacted. This underscores the necessity of the second stage of reaction for consistent material synthesis.

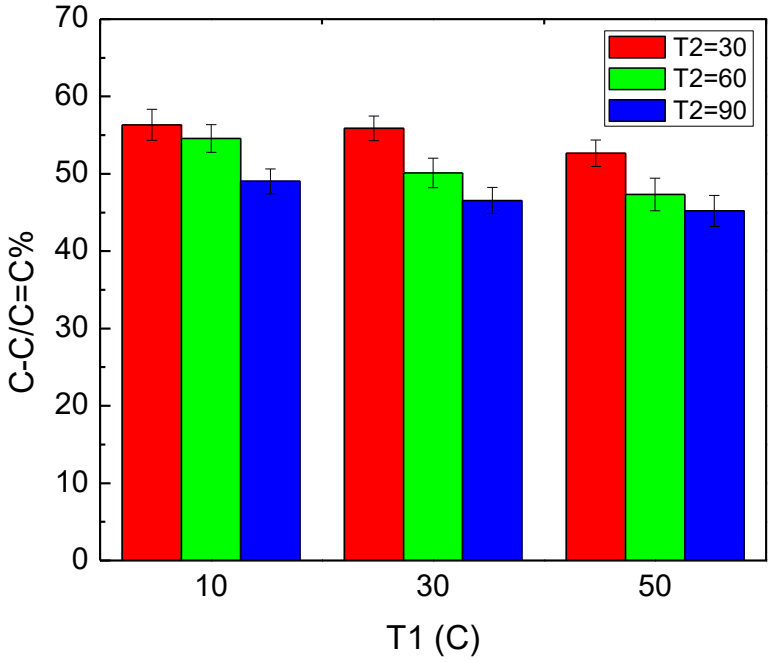

Figure 2.1. Oxidation state change (from XPS C 1s scan) with reaction temperature, with T1 (10, 30, 50 °C) for stage 1 and T2 (30, 60, 90 °C) for stage 2. Reaction time is 2 hours for stage 1 and 60 min for stage 2, with oxidant ratio of 3:1. The sonication time is 2 hours.

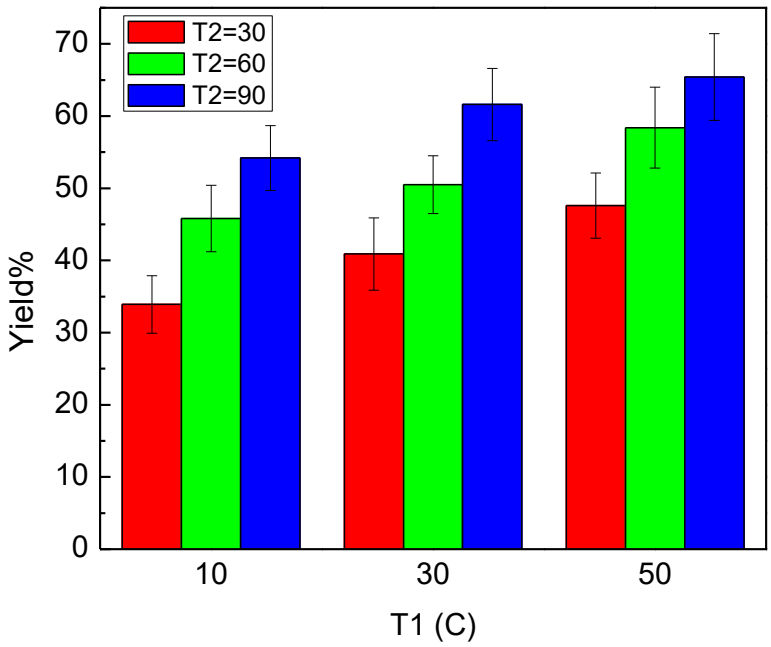

Figure 2.2 Yield change with reaction temperature, with T1 (10, 30, 50 °C) for stage 1 and T2 (30, 60, 90 °C) for stage 2. Reaction time is 2 hours for stage 1 and 60 min for stage 2, with oxidant ratio of 3:1. The sonication time is 2 hours.

2.3.2 Reaction Time

Figure 2.3 shows the oxidation state change, represented by the C-C/C=C percentage and the corresponding yield, as the function of reaction time. The C/O ratio, C-O and C=O percentage are summarized in Table S2.1 in the Supporting Information. Data in Figure 2.3 suggests that longer reaction times in stage 1 yields more oxidized graphene oxide (within 2 hours) and further increase in reaction times marginally increase in the oxidation state. The increase in reaction time of stage 2 did not have much effect on the oxidation state (less than 5% difference). However, in terms of the yield, longer reaction time does make a difference as shown in Figure 2.4, increasing the yield from 26.4% to 51.1%, 35.4% to 52.9%, 41.9% to 55.6%, and 43.2% to 55.3% for first stage reaction time of 1, 2, 3, 4 hours, respectively. Longer reaction times likely

reach a point whereby the major oxidant ($KMnO_4$) is completely consumed. Data shows that at temperature of 30 °C in the stage 1, the oxidation of graphite reached a limit after 2 hours, which could be due to aforementioned transport limitations caused by high viscosity of the reaction mixture. Again, as viscosity was decreased (by diluting the mixture), the oxidation faster towards the inner layers of the graphitic oxide particles, which was the main reason for the yield increases, as more functional groups inside could exist to facilitate the exfoliation. Note that with longer t1, the effect of t2 on yield increase would drop because of the limited amount of $KMnO_4$. With t1 being 1 hour, the yield kept increasing with t2 increased from 0 min to 120 min. However, with t1 being 3 or 4 hours, the yield would only increase till t2 reached 60 min.

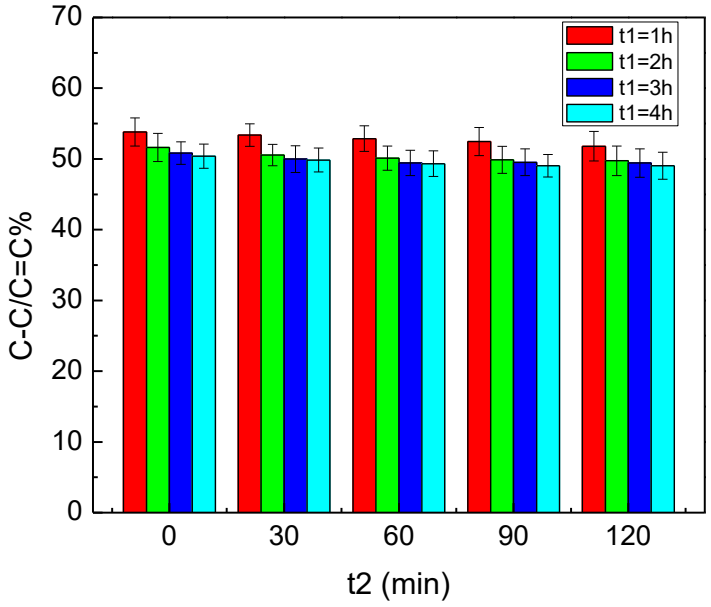

Figure 2.3 Reaction time effect on the carbon oxidation state (from XPS C 1s scan) of graphene oxide, with t1 (1, 2, 3, 4 hours) for stage 1 and t2 (0, 30, 60 90 120 min) for stage 2. Reaction temperature is 30 °C for stage 1 and 60 °C for stage 2, with oxidant ratio of 3:1. The sonication time is 2 hours.

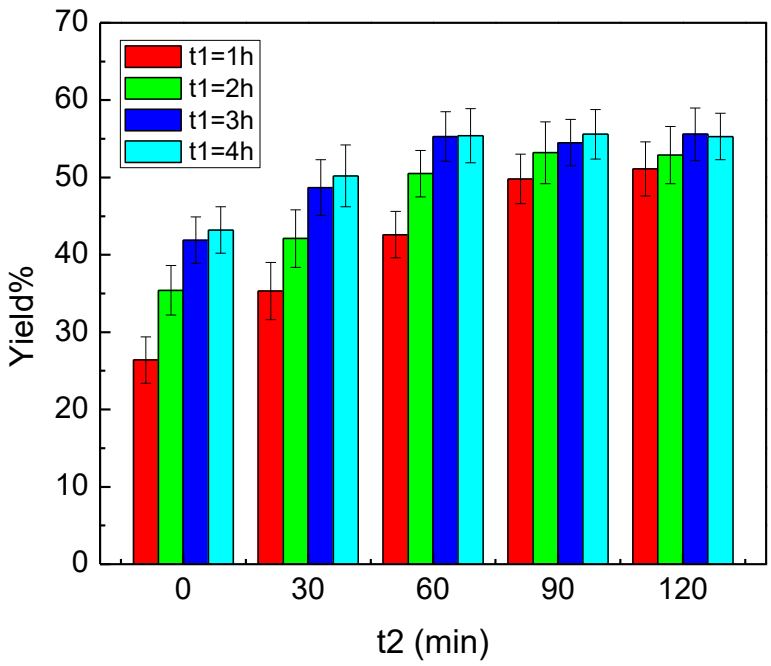

Figure 2.4 Reaction time effect on the yield of graphene oxide, with t1 (1, 2, 3, 4 hours) for stage 1 and t2 (0, 30, 60 90 120 min) for stage 2. Reaction temperature is 30 °C for stage 1 and 60 °C for stage 2, with oxidant ratio of 3:1. The sonication time is 2 hours.

2.3.3 Oxidant Ratio

Another key variable in GO syntheses reactions is the oxidant ratio. Figure 2.5 shows the oxidation state, represented by C-C/C=C percentage, and yield of the product graphene oxide with oxidant ratio of 1:1, 3:1 and 5:1. Note that in the case of 1:1 ratio, the C-C/C=C ratio of the graphene oxide was below 55%, indicating oxidation occurred; however, yields were below 10% even with the highest temperature set (GO-3), as shown in Figure 2.6. This is due to insufficient functional group inside the graphitic oxide particles for exfoliation, even though the surface of the particles is well oxidized. This result indicates that the oxidant ratio has to be above a certain level to achieve enough oxidation of graphite/graphitic oxide to facilitate exfoliation of graphene oxide from the bulk into solution.

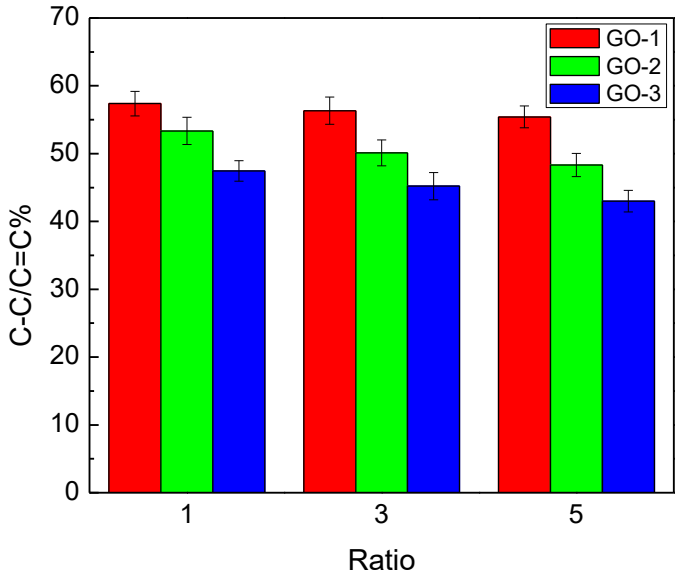

Figure 2.5 Oxidation state change (from XPS C1s scan) with oxidant ratio (1:1, 3:1, 5:1). The other reaction conditions are: 30 °C in stage 1 for 2 hours, 60 °C in stage 2 for 60 min and sonication for 2 hours.

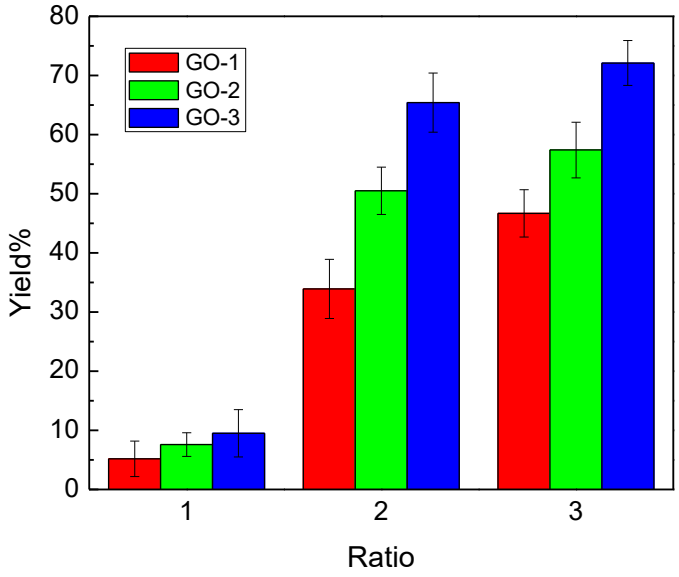

Figure 2.6 Yield change with oxidant ratio (1:1, 3:1, 5:1). The other reaction conditions are: 30 °C in stage 1 for 2 hours, 60 °C in stage 2 for 60 min and sonication for 2 hours.

2.3.4 Sonication

As a last step in the GO synthesis procedure, probe sonication is employed to enhance exfoliation and GO separation[109]. As a process with relatively large amount of energy input, sonication likely changes the oxidation state of the graphitic oxide and GO products. Here, the effects of sonication time and ratio (concentration of the initial graphitic oxide) on the oxidation state and yield are explored and described.

Figure 2.7 shows the oxidation state of carbon before and after 2 hours sonication followed by centrifuge process (described above), for both the supernatant and the precipitate. The first thing to notice is that after sonication, the graphitic oxide was slightly reduced, i.e. the C-C/C=C ratio increased. During the oxidation reaction, the outer layers were oxidized first and the functional groups form on the surface of the graphite particles. The functional groups effectively open or 'crack' graphite layers, increasing the distance between layers, thus allowing the oxidant to react with more carbon atoms oxidation propagated into the solid, the oxidant ($KMnO_4$) transport would then limit the reaction rate.[110, 111] XPS penetration depth is usually less than 100 nm, which is much smaller than the dimension of the graphitic oxide particles, thus XPS data collected (from the precipitate) is mainly from the surface layers of the graphitic oxide particle, instead of an average of the entire particle. During the sonication process, the inner layers, which were less oxidized, started to be exposed and exfoliated. Based on these reasons, after the sonication, the less oxidized graphene oxide was exposed to the surface and the measured overall oxidation state of the graphitic oxide and product graphene oxide effectively decreases. The difference of oxidation state between the supernatant and precipitate also supports this hypothesis, whereby the materials in the supernatant are more oxidized than the precipitate,

suggesting that the exfoliated (outer) layers have higher overall oxidation state (carbon) than the layers remaining in the bulk.

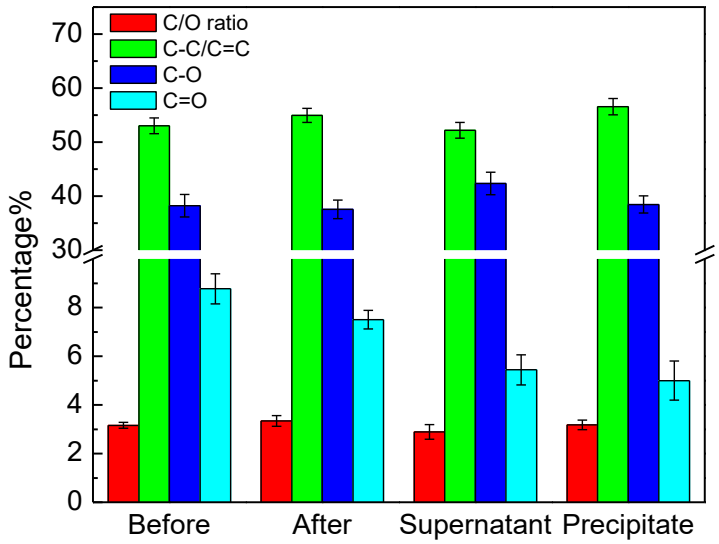

Figure 2.7 GO solution before and after 2 h sonication, supernatant vs. precipitate. The reaction conditions are: 30 °C in stage 1 for 2 hours, 60 °C in stage 2 for 60 min, oxidant ratio of 3:1 and sonication for 2 hours.

We further increased the sonication time to 6 hours and monitored the oxidation state change of the graphitic oxide and the corresponding graphene oxide product after centrifuge at each time interval. The oxidation state change of graphitic oxide and produced graphene oxide is shown in Figure 2.8. It was found that the oxidation state of graphitic oxide in the suspension showed little change within 4 hours with regard to C-C/C=C ratio (from 53% to 56%), which was consistent with the data in Figure 2.7 and discussion above. The oxidation state of the product graphene oxide after centrifuge also showed the same trend, with C-C/C=C percentage increased from 47% to 52%. Liscio et al and Pan et al independently reported the hypothesis that during sonication process, C-C bond breakage could occur, leading to decreased ratio of C-

C/C=C in the XPS spectrum[110, 112]. Further, due to the high energy input from the sonication, localized environments could be of high temperature and pressure, which could lead to both formation of oxygen groups (similar to oxidation of graphite) and deformation of oxygen group (similar to thermal reduction), according to the research of Qi et al[113]. Thus there are likely several mechanisms working together to change the average oxidation state of the graphene oxide product: 1) inner layers with lower oxidation state are exfoliated, leading to lower average oxidation state; 2) oxygen functional group formation and deformation due to the energy input, and with undetermined effect on the oxidation state; and 3) C-C bond breakage led to lower ratio of C-C/C=C and higher oxidation state. This could explain the platform after 4 hours since it could reach steady state in terms of average oxidation state.

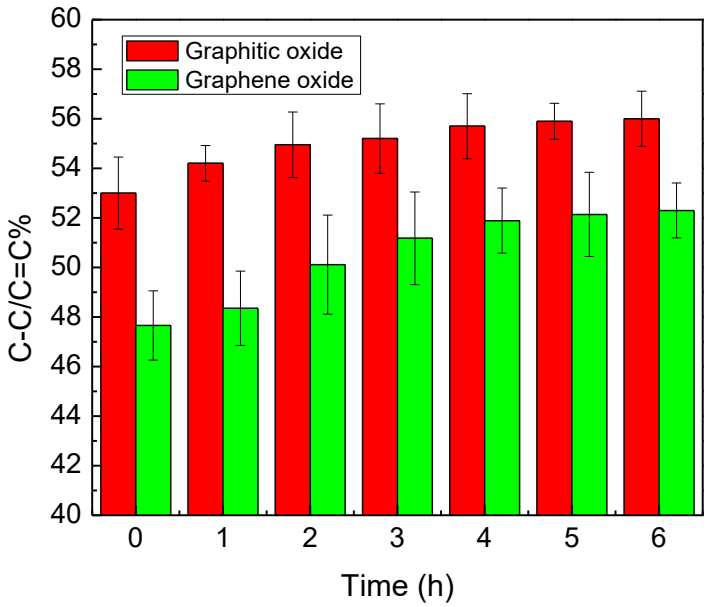

Figure 2.8 Oxidation state change of the graphitic oxide and corresponding graphene oxide with sonication time ranging from 0 to 6 hours. The other reaction conditions are: 30 °C in stage 1 for 2 hours, 60 °C in stage 2 for 60 min and oxidant ratio of 3:1.

Figure 2.9 shows the effect of sonication time on the yield, which increased rapidly in the first 2 – 3 hours then slows, which was consistent with the report from Botas et al, even though they did not try to characterize the oxidation state of the product graphene oxide[114]. After 4 hours, the yield could reach over 60% then reaches plateau. Also note that without sonication, the centrifuge of graphitic oxide still yields around 5% of graphene oxide in the supernatant.

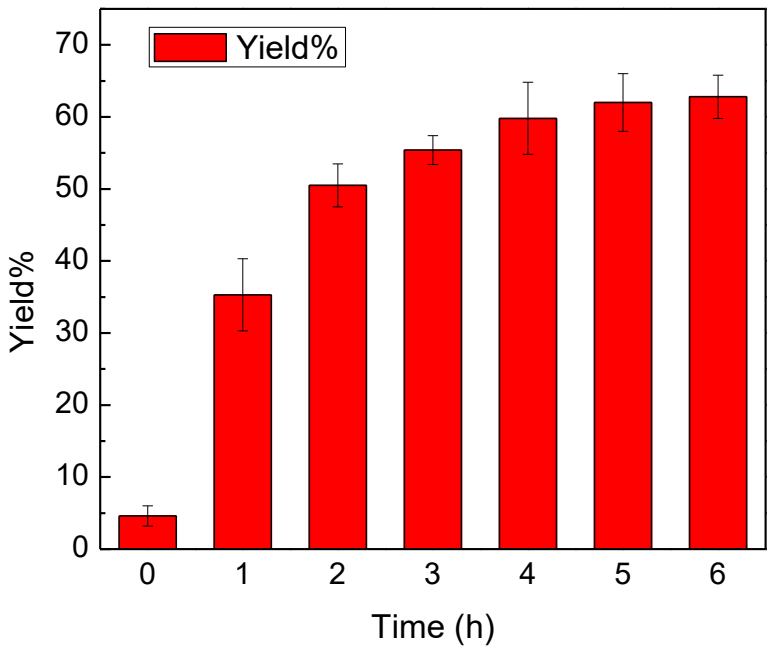

Figure 2.9 Sonication yield change with sonication time ranging from 0 to 6 hours. The other reaction conditions are: 30 °C in stage 1 for 2 hours, 60 °C in stage 2 for 60 min and oxidant ratio of 3:1.

The concentration of graphitic oxide in the sonication suspension will affect the average energy put onto each particle. Figure 2.10 shows yield and oxidation state change with different initial graphitic oxide concentration (total mass mg/L), after 2 hours sonication. As the initial concentration increased, the yield of the GO product decreased, due to reduced energy input per graphitic oxide particle. At lower concentrations (e.g. 100 mg/L), yields reached as high as 90%

while yields decreased to below 50% when sonicating at higher concentration (e.g. 1500 mg/L). Figure 2.10 also shows that as a higher percentage of the graphitic oxide was exfoliated, the overall oxidation state of the product decreased. Based on these results, it is important to find the balance between improving yield and achieving high-oxidized graphene oxide. Another aspect to consider is that even though high yields can be achieved at low concentration of graphitic oxide, the corresponding concentration of graphene oxide is low, which could be a concern for some synthesis routes and related applications.

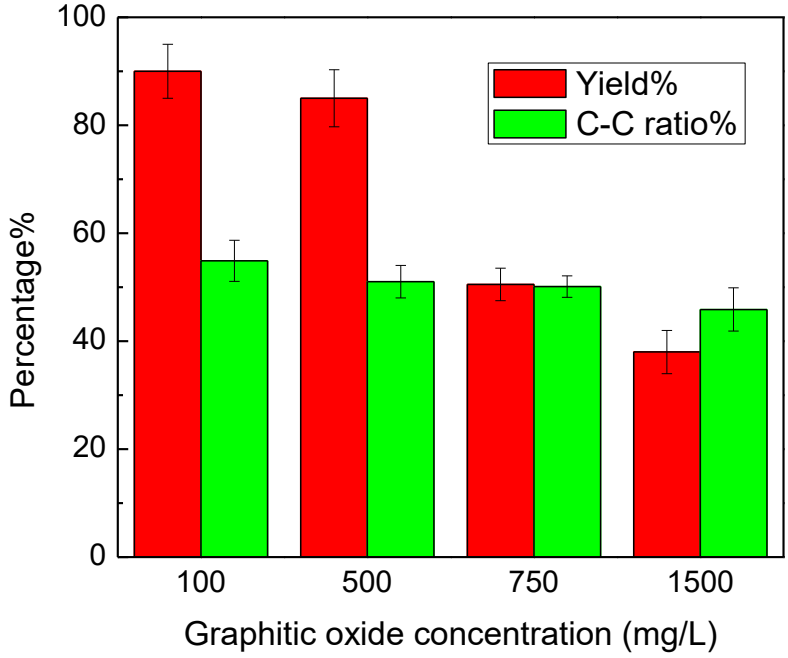

Figure 2.10 Initial graphitic oxide concentration (total mass) effect on yield and oxidation state. The graphitic oxide is synthesized with reaction conditions as: 30 °C in stage 1 for 2 hours, 60 °C in stage 2 for 60 min, oxidant ratio of 3:1 and sonication for 2 hours.

2.3.5 TEM Imaging

Figure 2.11 showed the TEM images of synthesized graphene oxide (GO-2 via standard Hummers method). We did not observe significant difference via electron microscopy between graphene oxide samples synthesized under different conditions.

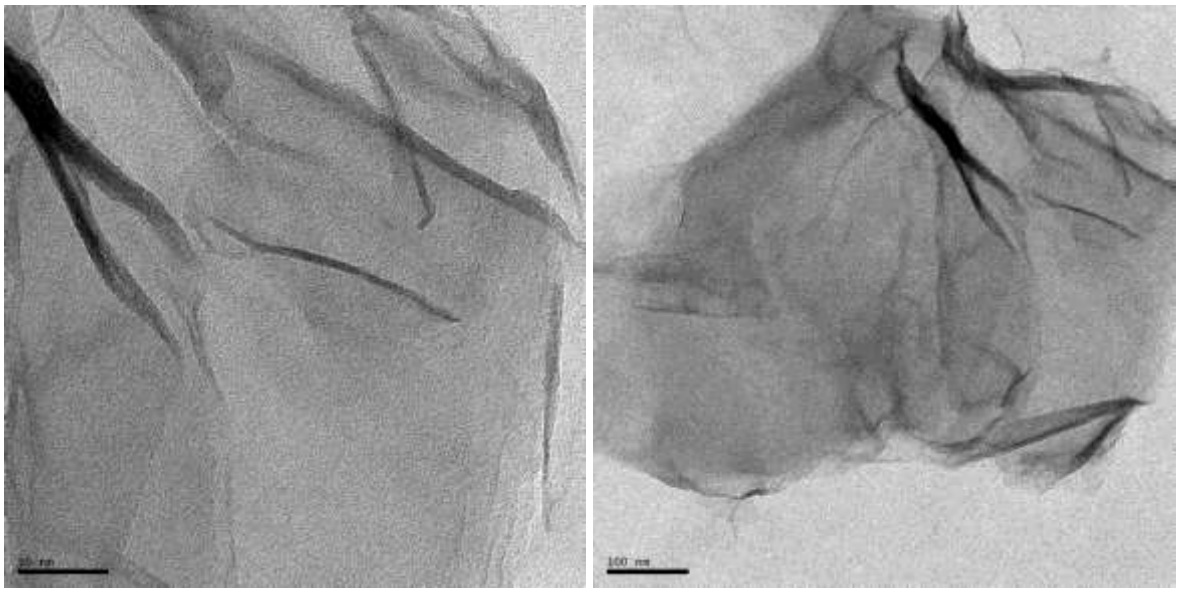

Figure 2.11 TEM images of graphene oxide synthesized with conditions as: 30 °C in stage 1 for 2 hours, 60 °C in stage 2 for 60 min, oxidant ratio 3:1 and sonication for 2 hours.

2.3.6 UV-visible Spectroscopy and Band Gap

UV-vis spectroscopy is a relatively fast and efficient way to evaluate graphene oxide structural information as well as relative concentration. Figure 2.12 shows the UV-vis spectra of three types of GO synthesized at different temperatures (as GO-1, GO-2 and GO-3 as detailed in the Experimental section). The characteristic peak at ~230 nm corresponds to π-π conjugation, which represents the sp^2 carbon domains in the graphene oxide structure[115]. The shoulder peak at ~ 310 nm is assigned to n-π excitation, which represents the C-O and C=O groups on the graphene oxide structure[116]. For these materials, a blue shift is also observed as the synthesis temperature increased, with 240 nm for GO-1, 234 nm for GO-2 and 230 nm for GO-3, indicating that

graphene oxide is more oxidized, with a higher band gap[115]. Based on the UV-vis spectra, we were able to calculate the band gap of synthesized graphene oxide materials via Tauc's expression[117, 118, 119]:

$$\omega^2\varepsilon = (h\omega - E)^2$$

where ω is the angular frequency which is taken as 2πc/λ and ε is the adsorption intensity. E is the optical band gap. By plotting $\varepsilon^{1/2}/\lambda$ vs. h/λ, the extrapolated intercept with the h/ λ axis would give band gap energy value (E/2πc). The calculated band gap values are summarized in Table 2.1. As temperature increased, the band gap also increased with the higher oxidation state and quantity of functional groups, from 0.36 eV for GO-1 to 1.92 eV for GO-3. This tunable property could also contribute to electronic and photo-based applications of graphene oxide[115, 119, 120].

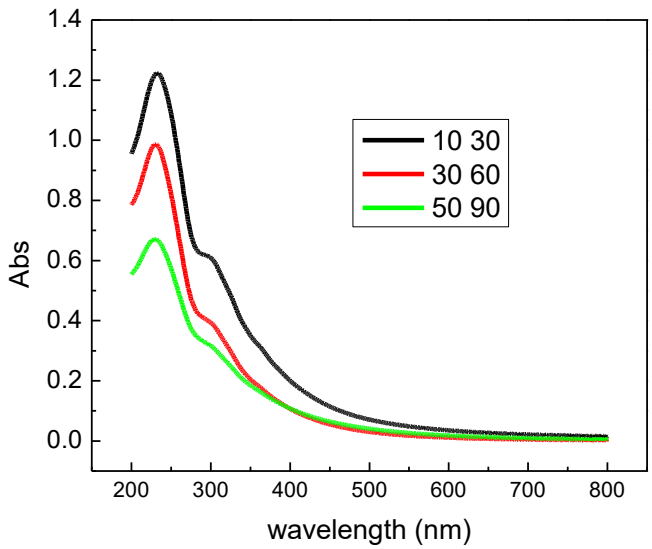

Figure 2.13 UV-vis spectra of graphene oxide. The GO is synthesized at temperature of 10 °C and 30 °C (GO-1), 30 °C and 60 °C (GO-2) and 50 °C and 90 °C (GO-3). Other reaction conditions are: reaction time of 2 hours for stage 1 and 60 min for stage 2, oxidant ratio of 3:1 and sonication for 2 hours.

Table 2.1 Optical band gap of graphene oxide with different oxidation state

	Optical band gap / eV
GO-1	0.36
GO-2	1.04
GO-3	1.92

2.3.7 Raman Spectroscopy

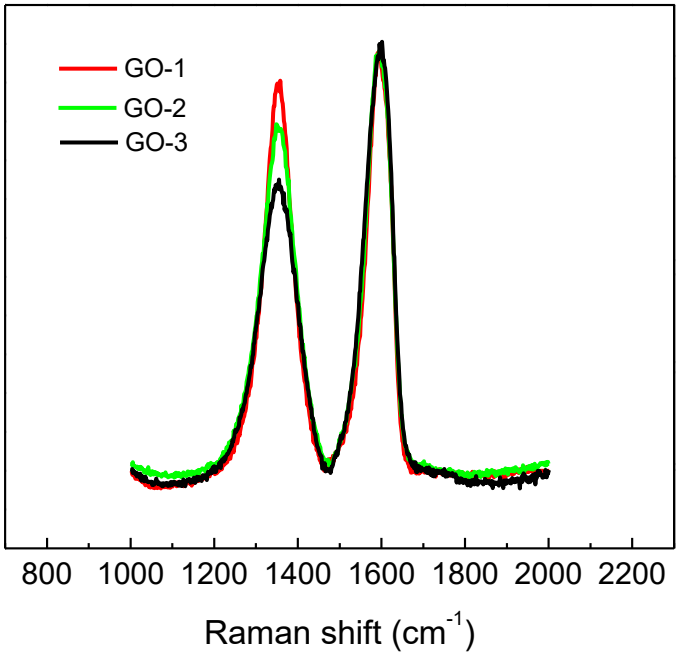

Figure 2.14 Raman spectra of GO. The GO is synthesized at temperature of 10 °C and 30 °C (GO-1), 30 °C and 60 °C (GO-2) and 50 °C and 90 °C (GO-3). Other reaction conditions are: reaction time of 2 hours for stage 1 and 60 min for stage 2, oxidant ratio of 3:1 and sonication for 2 hours.

Raman spectroscopy is widely used to quantify the defects and average size of the sp^2 domain for carbon materials which provide insight into the structure and fundamental properties, as well as providing reference for applications[31]. Figure 2.14 shows Raman spectra for three types of graphene oxide synthesized at different temperatures as GO-1, GO-2 and GO-3 stated in Experimental section, in which the D band at 1355 cm^{-1} is due to the breathing modes of hexagon rings and requires defect for the activation, thus representing a defect structure (sp^3 carbon)[121-124], while The G band at 1603 cm^{-1} represents the graphene base structure (sp^2 carbon), which arises from the first order scattering of E_{2g} phonons of the graphitic carbon atoms[31]. The ratio of D band over G band is a relative measurement of the average size of the sp^2 network[31], This method has been widely used according to Tuinstra and Koenig, in which they found the ratio of D band intensity over G band intensity increased with more defects (smaller average size of the sp^2 domain)[121]. However, this relationship can fail for high defect densities[122]. In a certain regime, higher D/G ratio stands for smaller sp^2 network but according to research by Cancado et al., higher D/G ratio could represent larger sp^2 network in the GO structure itself[125]. By analyzing the G peak width (measured by the full width at half-maximum, FWHM), we can distinguish between the two stages, as it would be significantly larger in stage 2 where the D/G ratio is decreasing while more defects exist[125]. According to their research, I_D/I_G is also affected by the laser energy , thus we used same laser wavelength (514 nm) and intensity for all experiment, thus the change in I_D/I_G should be only affected by the relative quantity of the disordered structure and graphene structure[125]. Also note that this analysis only applies to defects which could activate the D peak. It has been reported that a perfect zigzag GO edge is not included as defect measured by Raman spectroscopy[126, 127]. The Raman spectra of the 3 types of graphene oxide were shown in Figure 2.17 with the G peak normalized to the same level. It

shows that the oxidized GO has lower D peak intensity, which suggest that higher disordered structure. Also the D/G ratio and FWHM for G and D peaks were summarized in Table 2.2. The data confirmed that more oxidized GO with broader peaks (both D peak and G peak), which had more disordered structure, would have lower D/G ratio, being 0.983 for GO-1, 0.843 for GO-2 and 0.687 for GO-3.

Table 2.2 Raman spectra data for 3 types of GO

	G FWHM / cm^{-1}	D FWHM / cm^{-1}	I_D/I_G
GO-1	68.84	78.49	0.983
GO-2	71.35	91.85	0.843
GO-3	76.18	104.94	0.687

2.3.8 Thermogravimetric Analysis (TGA)

TGA quantitatively measures total mass loss of a material as a function of temperature. For GO materials evaluated, TGA curves of the three types of graphene oxide synthesized at different temperatures (as GO-1, GO-2 and GO-3 stated in Experimental section) were shown in Figure 2.15. As temperature increases, associated water first evaporates at around 150 °C. Around 220 °C, we observe another major mass loss which was caused by the pyrolysis of the oxygen functional groups, generating CO and CO_2 as observed by others[128, 129]. The drop (loss) in more oxidized graphene oxide was more significant due to the higher quantity of functional groups. The weight continues to decrease and at the end of thermal degradation, there was 43.6% weight remaining in GO-1, 35.8% in GO-2 and 31.4% in GO-3. This also suggested more oxidized

graphene oxide would be more vulnerable to thermal degradation, due to lower chemical stability of the functional groups compared to graphene structures[130].

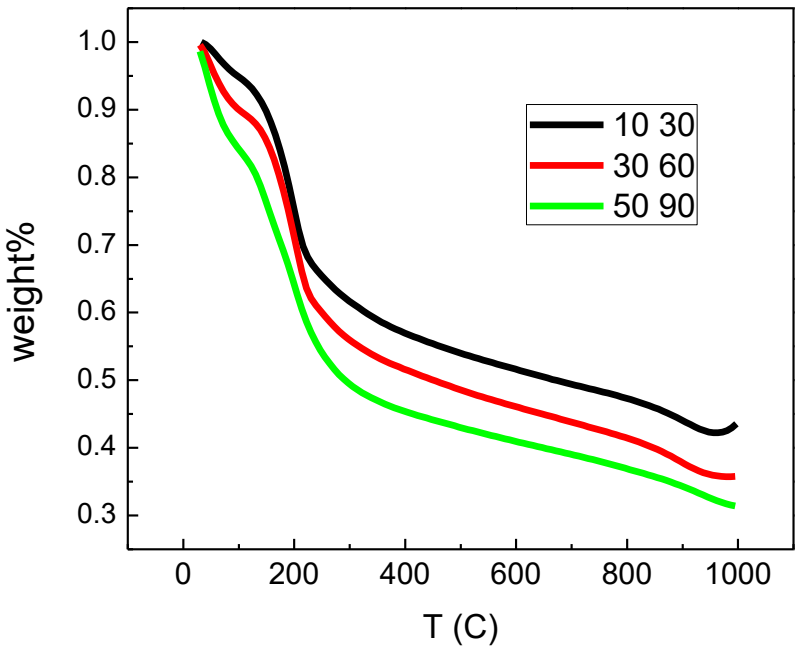

Figure 2.15 TGA result of GO. The GO is synthesized at temperature of 10 °C and 30 °C (GO-1), 30 °C and 60 °C (GO-2) and 50 °C and 90 °C (GO-3). Other reaction conditions are: reaction time of 2 hours for stage 1 and 60 min for stage 2, oxidant ratio of 3:1 and sonication for 2 hours.

2.3.9 Fourier Transform Infrared Spectroscopy

Figure 2.16 showed the FTIR spectra of the three types of graphene oxide synthesized at different temperatures (as GO-1, GO-2 and GO-3 stated in Experimental section). The broad peak at 3200 cm^{-1} indicated the existence of –OH group[131]. The peak at 1740 cm^{-1} is assigned to the C=O stretching vibration and its intensity increased with the synthesis temperature, which is consistent with the XPS data[31, 132, 133]. The peak at 1620 cm^{-1} is attributed to the aromatic C=C vibrations in the skeleton of the graphene structure[31, 131]. The peak at 1420 cm^{-1} corresponds to

the O-H deformation vibration[31]. The C-O stretching vibration peak found at 1220 cm^{-1} for epoxy group and 1050 cm^{-1} for alkoxy group and both of their intensities increased with the synthesis temperature[31, 131]. The peak at 850 cm^{-1} represents the C-H vibration and this was contributed to a portion of the disordered structure characterized by Raman spectroscopy[31]. The result was consistent with our other characterization, showing that GO-3 had the most functional groups while GO-1 had the least, but they all have the same set of functional groups.

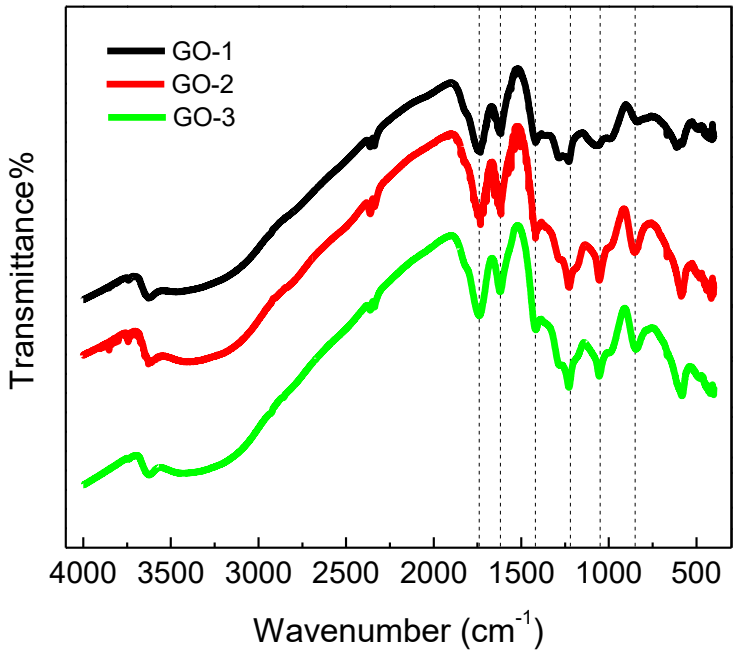

Figure 2.16 FTIR spectra of three types of graphene oxide. The GO is synthesized at temperature of 10 °C and 30 °C (GO-1), 30 °C and 60 °C (GO-2) and 50 °C and 90 °C (GO-3). Other reaction conditions are: reaction time of 2 hours for stage 1 and 60 min for stage 2, oxidant ratio of 3:1 and sonication for 2 hours.

2.3.10 Hydrodynamic Size Distribution, Zeta Potential, and Colloidal Stability

For aqueous applications, such as adsorption and catalysis, the interaction between graphene oxide particles and other components in the environment is critical. The hydrodynamic size and

zeta potential are key properties regarding aqueous stability, transport, and reactivity of the material. Due to oxygen functionality, including –COOH groups, on the surface and edges, graphene oxide is net negatively charged and the dissociation of –COOH would be affected by pH. Table 2.3 showed the hydrodynamic diameter and zeta potential at pH 7 for three types of GO synthesized at different temperatures (as GO-1, GO-2 and GO-3 stated in Experimental section) and Figure 2.17 showed the pH effect on the zeta potential. As pH is increased from 2 to 9, the zeta potential changed from -19.7 mV to -41.04 mV for GO-1, -24.43 mV to -47.97 mV for GO-2, and -28.45 mV to -55.13 mV for GO-3, respectively. Also, at same pH, relatively more oxidized (higher degree) graphene oxide has a more negative zeta potential, due to higher quantity of functional groups per coupon.

Table 2.3 Hydrodynamic diameter and zeta potential of GO at pH 7

	Hydrodynamic diameter / nm	Zeta potential / mV
GO-1	184.70 ± 8.17	-38.50 ± 0.81
GO-2	176.87 ± 7.80	-44.73 ± 0.97
GO-3	156.07 ± 6.10	-52.80 ± 1.13

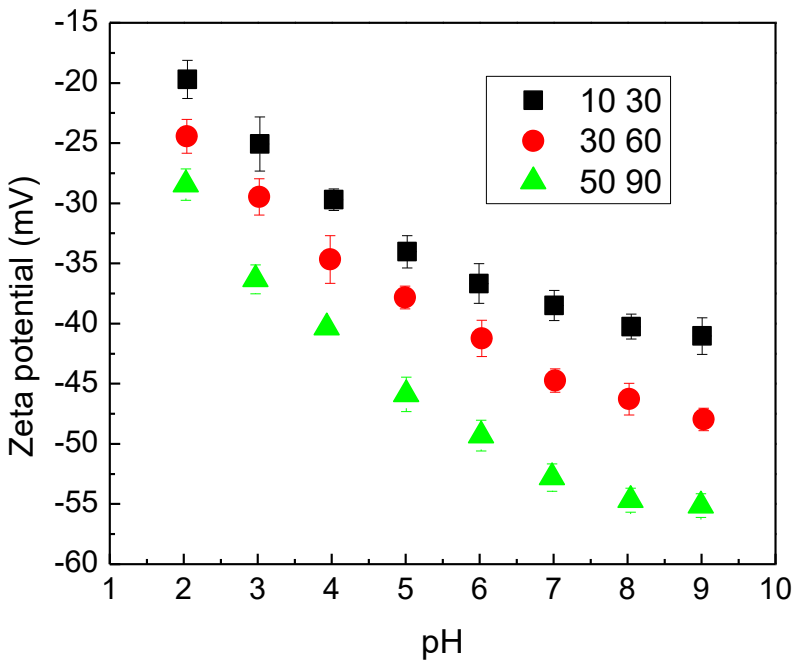

Figure 2.17 Zeta potential of GO under different pH levels. The GO is synthesized at temperature of 10 °C and 30 °C (GO-1), 30 °C and 60 °C (GO-2) and 50 °C and 90 °C (GO-3). Other reaction conditions are: reaction time of 2 hours for stage 1 and 60 min for stage 2, oxidant ratio of 3:1 and sonication for 2 hours.

As a promising material with a wide range of potential applications in water, the aqueous stability regimes of GO is crucial to understand. There have been studies regarding the colloidal stability of GO over the past years[106, 134-138]. However, this critical property has not been correlated with the surface chemistry of the material. Here we chose three types of GO synthesized at different temperatures (as GO-1, GO-2 and GO-3 stated in Experimental section) to explore the colloidal stability, as evaluated by critical coagulation concentration (CCC) values as a function of Na^+ and Mg^{2+} catiosn, which are commonly used in evaluating the stability and coagulation behavior of nano-materials. Figure 2.18 and Figure 2.19 shows the attachment efficiency of graphene oxide with Na^+ and Mg^{2+} and the extrapolation lines from the diffusion

limited regime and reaction limited regimes. The CCC values for three types of graphene oxide were summarized in Table 2.4; as the quantity of functional group increased, the CCC value for both Na^+ and Mg^{2+} increased, being 195.0 mM and 10.58 mM for GO-1, 237.4 mM and 13.33 mM for GO-2, and 306.3 mM and 18.64 mM for GO-3.

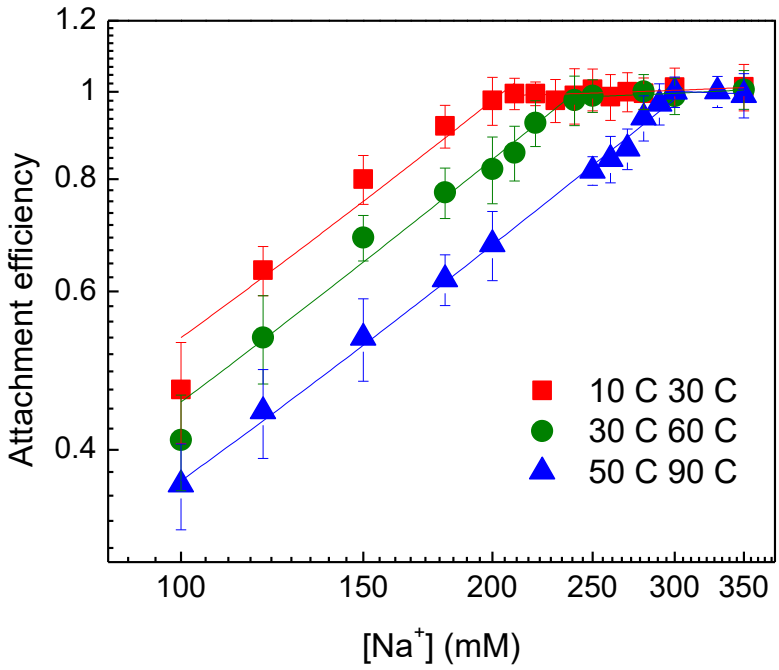

Figure 2.18 Critical coagulation of GO with Na^+. The GO is synthesized at temperature of 10 °C and 30 °C (GO-1), 30 °C and 60 °C (GO-2) and 50 °C and 90 °C (GO-3). Other reaction conditions are: reaction time of 2 hours for stage 1 and 60 min for stage 2, oxidant ratio of 3:1 and sonication for 2 hours.

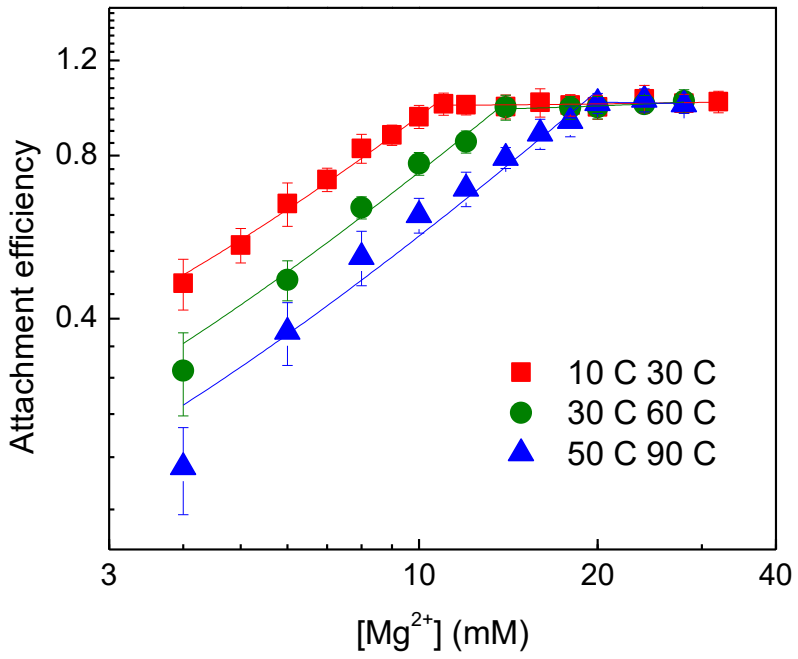

Figure 2.19 Critical coagulation of GO with Mg^{2+}. The GO is synthesized at temperature of 10 °C and 30 °C (GO-1), 30 °C and 60 °C (GO-2) and 50 °C and 90 °C (GO-3). Other reaction conditions are: reaction time of 2 hours for stage 1 and 60 min for stage 2, oxidant ratio of 3:1 and sonication for 2 hours.

Table 2.4 Critical coagulation concentration of GO with Na^{+} and Mg^{2+}

	Na^{+} / mM	Mg^{2+} / mM
GO-1	202.9	10.6
GO-2	237.4	13.6
GO-3	306.3	19.0

2.4 Conclusion

In this chapter, key factors in graphene oxide synthesis process were explored and described, including temperature in two stages, reaction time, oxidant ratio, sonication ratio, and sonication time. It was found that as temperature increased, the relative oxidation state and yield also increased. Reaction time and oxidant ratio increases the oxidation state but overall they have more impact on the total (final) yield of graphene oxide. The oxidant ratio also has significant impact on the yield. Sonication can also change the oxidation rate and yield as the last step in the synthesis process. Longer sonication time led to less oxidized graphene oxide but higher yields. Characterization methods were established and describe different properties of graphene oxides, including hydrodynamic size, zeta potential, colloidal stability, structural disorder, and functional groups types and relative amounts.

Chapter 2: Supporting Information

Table S2.1 XPS result for temperature effect on synthesized graphene oxide, other conditions are: reaction time of 2 hours in stage 1 and 60 min in stage 2, oxidant ratio of 3:1 and sonication for 2 hours.

	T1 / °C	T2 / °C		
		30	60	90
C-C	10	56.33	54.56	49.02
	30	55.87	50.11	46.55
	50	52.66	47.32	45.21
C-O	10	36.26	36.88	40.95
	30	35.79	40.33	42.56
	50	38.57	41.98	43.66
C=O	10	7.41	8.56	10.03
	30	8.34	9.56	10.89
	50	8.77	10.7	11.13
C/O	10	3.01	2.75	2.64
	30	2.86	2.68	2.59
	50	2.73	2.62	2.34

Table S2.2. XPS result for reaction time effect on synthesized graphene oxide, other conditions are: 30 °C in stage 1 and 60 °C in stage 2, oxidant ratio of 3:1 and sonication for 2 hours.

	t2 / min	t1 / h			
		1	2	3	4
C-C	0	53.82	51.63	50.84	50.4
	30	53.38	50.55	49.98	49.85
	60	52.87	50.11	49.43	49.33
	90	52.46	49.88	49.53	49.03
	120	51.8	49.74	49.42	49.05
C-O	0	36.43	39.02	40.4	40.98
	30	37.5	39.98	40.8	41.38
	60	38.12	40.33	41.25	41.36
	90	38.65	40.69	41.47	41.53
	120	38.96	40.8	41.35	41.37
C=O	0	9.75	9.35	8.76	8.62
	30	9.12	9.47	9.22	8.77
	60	9.01	9.56	9.32	9.31
	90	8.89	9.43	9	9.44
	120	9.24	9.46	9.23	9.58
C/O	0	2.9	2.74	2.68	2.6
	30	2.83	2.65	2.58	2.55
	60	2.75	2.68	2.46	2.49
	90	2.68	2.63	2.48	2.38
	120	2.72	2.53	2.45	2.43

Table S2.3. XPS result for oxidant ratio effect on synthesized graphene oxide, other conditions are: 30 °C in stage 1 for 2 hours, 60 °C in stage 2 for 60 min, and sonication for 2 hours.

	Ratio	GO-1	GO-2	GO-3
C-C	1	57.38	53.35	47.45
	3	56.33	50.11	45.21
	5	55.42	48.33	42.99
C-O	1	35.24	38.62	41.42
	3	36.26	40.33	43.66
	5	37.5	41.5	45.87
C=O	1	7.38	8.03	11.13
	3	7.41	9.56	11.13
	5	7.08	10.17	11.14
C/O	1	3.26	2.93	2.71
	3	3.01	2.68	2.34
	5	2.79	2.49	2.25

Chapter 3: Photoenhanced Transformation of Graphene Oxide by Free Chlorine: Reaction Kinetics and Product Characterization

Abstract

Herein, reactions of graphene oxide (GO) with free chlorine are described under both dark and ultraviolet (UV) irradiated conditions. For all cases investigated, GO reacts with free chlorine and reaction rates are considerably enhanced under UV irradiation. Relative reaction kinetics are observed to be second order overall, while being first order to graphene oxide and pseudo first order to the initial chlorine concentration. In addition to light, rate constants are affected by pH, dissolved oxygen, and the size of initial graphene oxide coupon. Product characterization using UV-vis spectroscopy, TEM, FTIR, TOC, Raman spectroscopy, mass spectrometry, and XPS indicate graphene oxide is significantly transformed, being further oxidized - including partial mineralization. Further, fractions of the product(s) are identified to eventually stop reacting with free chlorine, suggesting a final, (relatively) recalcitrant reaction product. For all reactions, carbon mass conservation between the gas (as CO_2) and liquid (as GO products) phases is confirmed. Observed reactivity has direct implications for water treatment technologies, such as membrane separation processes, which utilize graphene oxide-based materials and free chlorine and/or UV, in addition to other aqueous graphene oxide based technologies.

3.1 Introduction

Chlorination is commonly applied technology for water treatment due to low cost, wide availability, and high efficacy.[139, 140] In particular, chlorine is a globally applied disinfectant in its

molecular (Cl_2) form or as hypochlorite salts (NaClO).[141] In water, hypochlorite salts undergo hydrolysis to generate free chlorine, which consists of aqueous molecular chlorine (Cl_2), hypochlorite ion (ClO^-) and hypochlorous acid (HOCl), depending on solution pH.[142] Also after GO is released into the environment, sunlight irradiation may also cause GO to transform. With the presence of free chlorine and sunlight irradiation, ·Cl and ·OH are the primary radical products, which can subsequently lead to the formation of other oxygen and/or chlorine based radicals, including $\cdot O^-$ and ClO·, among others.[143] As demonstrated by Kim et al., such radicals have been hypothesized to attack and transform the graphene basal plane, resulting in sp^3 carbon with varying functionality.[144] Additionally, there have been reports regarding radical reactions with graphene and graphene oxide under UV irradiation. Zhao et al reported more defect on the GO plane after UV irradiation, indicated by higher D/G ratio in Raman spectra.[145] Ma et al. applied UV irradiation/H_2O_2 to GO and found that the characteristic peak of GO in UV-vis spectra decreased and the peak (absorbance) position was blue shifted by 5 nm (230 nm to 225 nm), indicating that GO was partially oxidized.[146] Under relatively harsher conditions (0.065 W/cm^2 for over 180 h), graphene oxide has been observed to undergo mineralization (i.e. CO_2 product), as reported by Hou.[147, 148] Further, Li et al. demonstrated a reaction of GO with free chlorine and chloramine (at 10 mg/L free chlorine), under dark conditions, resulting in a partial reaction.[149] Wu et al has demonstrated that fullerene, another carbonaceous material, could be transformed in the presence of free chlorine, both in the dark and under UV irradiation.[150-152] It is reasonable to assume GO could be transformed by free chlorine under light irradiation and Du et al have studied the GO transformation in the presence of low concentration of free chlorine under light irradiation and characterized the product.[153] However, the reaction kinetics and factors affecting the reaction were not fully explored, such as pH, radicals, coupon size,

dissolved oxygen. Also CO_2, as the possible product, was not identified. In this work, graphene oxide reactivity with free chlorine under both dark and UV irradiation is quantitatively described. High free chlorine concentration was used to better clarify the reaction kinetics and mechanism between GO and free chlorine under light irradiation. Reaction kinetics are described as a function of pH and initial GO coupon size, with involvement of radicals, in addition to the presence of UV light with resulting products characterized via a suite of complimentary spectral analyses and carbon mass balance(s). In the presence of high free chlorine under simulated sunlight irradiation we also observe GO to be partially mineralized to CO_2 with good mass balance. Smaller molecules are detected as reaction product by mass spectrometry and filtration method.

3.2 Materials and Methods

3.2.1 Materials

Graphite powder, sulfuric acid, potassium permanganate, and hydrogen peroxide solution were purchased from Sigma-Aldrich. Sodium hypochlorite solution (15% in Cl) was also purchased from Sigma-Aldrich as stock solution. All chemicals were reagent grade or higher and used without further purification, unless otherwise noted.

3.2.2 Synthesis of Graphene Oxide

A modified Hummers method was used to produce graphene oxide. First 2 g graphite flakes and 50 mL concentrated sulfuric acid were added into a beaker and kept at 0 °C using an ice bath. Then 6 g potassium permanganate were slowly added into the beaker and the temperature was increased to room temperature. After stirring for 2 h, the mixture was diluted with 350 mL water and the temperature was increased to 60 °C, and the mixture was stirred for 30 min. Then the mixture was cooled down to room temperature. Hydrogen peroxide (30%) was slowly added

until the gas evolution ceased to reduce the residual permanganate to soluble manganese ions. The mixture was filtered and washed with milli-Q water. After drying in a vacuum chamber at room temperature for 24 h, recovered solid of 300 mg was dissolved into 300 mL milli-Q water and sonicated for 2 h. After centrifuge, the supernatant containing the graphene oxide was collected as a stock solution. The concentration of the stock solution was about 500 mg/L, determined by UV-vis spectrometer at 230 nm and Total Organic Carbon analysis (TOC).

3.2.3 Graphene Oxide Reaction with Free Chlorine under Light Irradiation

Graphene oxide (reported here as 50 mg/L as total organic carbon; the concentration of GO throughout this work is all referred to via total organic carbon) with different concentrations of free chlorine (as NaClO) for varied pH levels was added into a 100 mL customized quartz reactors (Technical Glass Products) and placed in a custom-built, bench-scale photo-reactor with UVA lamps (centered at 351 nm, 2000 $\mu W/cm^{-2}$, similar to sunlight irradiation intensity). A phosphate buffer solution ($HNO_3/NaH_2PO_4/ Na_2HPO_4/NaOH$ 10 mM) was used to control the pH. Sample aliquots of 2 mL were withdrawn at appropriate time intervals for further characterization.

3.2.4 Product Characterization

During the reaction, samples were withdrawn for UV-visible spectroscopy measurement for kinetic study. Upon reaction termination, the reaction solution was washed in a stir cell using a membrane with MWCO of 1,000 Da for 5 times, each time with 200 mL of MilliQ water, to remove any complicating salts, reactants, buffer and possible small products. Samples with high molecular weight (remaining as particles) were characterized by Fourier transform infrared spectroscopy (FTIR), Transmission electron microscopy (TEM), Raman spectroscopy and X-ray photoelectron spectroscopy (XPS). For the product with small molecular weight, Matrix-Assisted

Laser Desorption/Ionization (MALDI) Time-of-Flight Mass Spectrometry was used to detect them using the samples right after reaction is completed and without washing. The CO_2 product was detected and measured by Gas Chromatography after sampling from the gas phase during the reaction in closed system. Gas samples for GC and liquid sample for TOC analysis were taken at certain time interval with airtight syringes and needles. For coupon size dependence experiments, GO stock solutions were filtered using polyethersulfone membrane syringe filters (450 nm and 220 nm) to obtain GO with smaller sizes (than the parent stock solution). To explore potential ·OH radical involvement, *tert*-butanol (200 mM) was used as the scavenger.[154] In the anaerobic reactions, sealed quartz reactor with GO solution (50 mg/L) and phosphate buffer (10 mM) was purged using N_2 for 1 hour. Then hypochlorite solution as source of free chlorine was injected with airtight syringe and needle.

3.2.5 Chlorine Concentration Measurement

Based on the reported method water treatment, we used DPD colorimetric method to determine the free chlorine concentration.[155] The detail of the method is described in the Supporting Information.

3.2.6 Carbon Dioxide Quantification

For gas phase CO_2 quantification, we also took the dissolved CO_2 in the solution into consideration. It was assumed that the pressure in the bottle remained 1 atm over the course of the reaction, which results in ±3% error due to dissolved CO_2 generation. In the solution, the dissolved CO_2 exists in the following chemical equilibriums[92]:

$$H_2CO_3^* \leftrightharpoons H^+ + HCO_3^- \quad pK_a = 6.35$$

$$H_2CO_3^- \leftrightharpoons H^+ + CO_3^{2-} \quad pK_a = 10.33$$

As it was considered that, the Henry's law constant for CO_2 at room temperature is 0.034 mol/(L*atm)[92] for an open system with a constant pressure. By assuming the CO_2 in gas phase and liquid phase reached equilibrium, the dissolved CO_2 was calculated based on the gas phase CO_2 concentration as following:

$$dissolved\ CO_2 = 1\ atm \times [CO_2/ppm] \times H_{CO_2} \times \left[1 + \frac{K_{a1}}{[H^+]} + \frac{K_{a2}}{[H^+]^2}\right]$$

The total CO_2 generated from the reaction of GO with free chlorine under UV irradiation was calculated as the summation of dissolved CO_2 in the aqueous phase and the gas phase data, with units of mg carbon/L.

3.2.7 Instrumentation

Graphene oxide and products after reaction with free chlorine under light irradiation were characterized with UV-vis spectroscopy, transmission electron microscope (TEM), total organic carbon analysis (TOC), Fourier transform infrared spectroscopy (FTIR), Raman spectroscopy, X-ray Photoelectron Spectroscopy (XPS) and Matrix-Assisted Laser Desorption/Ionization (MALDI) Time-of-Flight Mass Spectrometry. The CO_2 concentration in the gas phase was measured by gas chromatography (GC). The detailed methods and instrument types were described in Supporting Information.

3.3 Results and Discussion

3.3.1 Reaction Kinetics

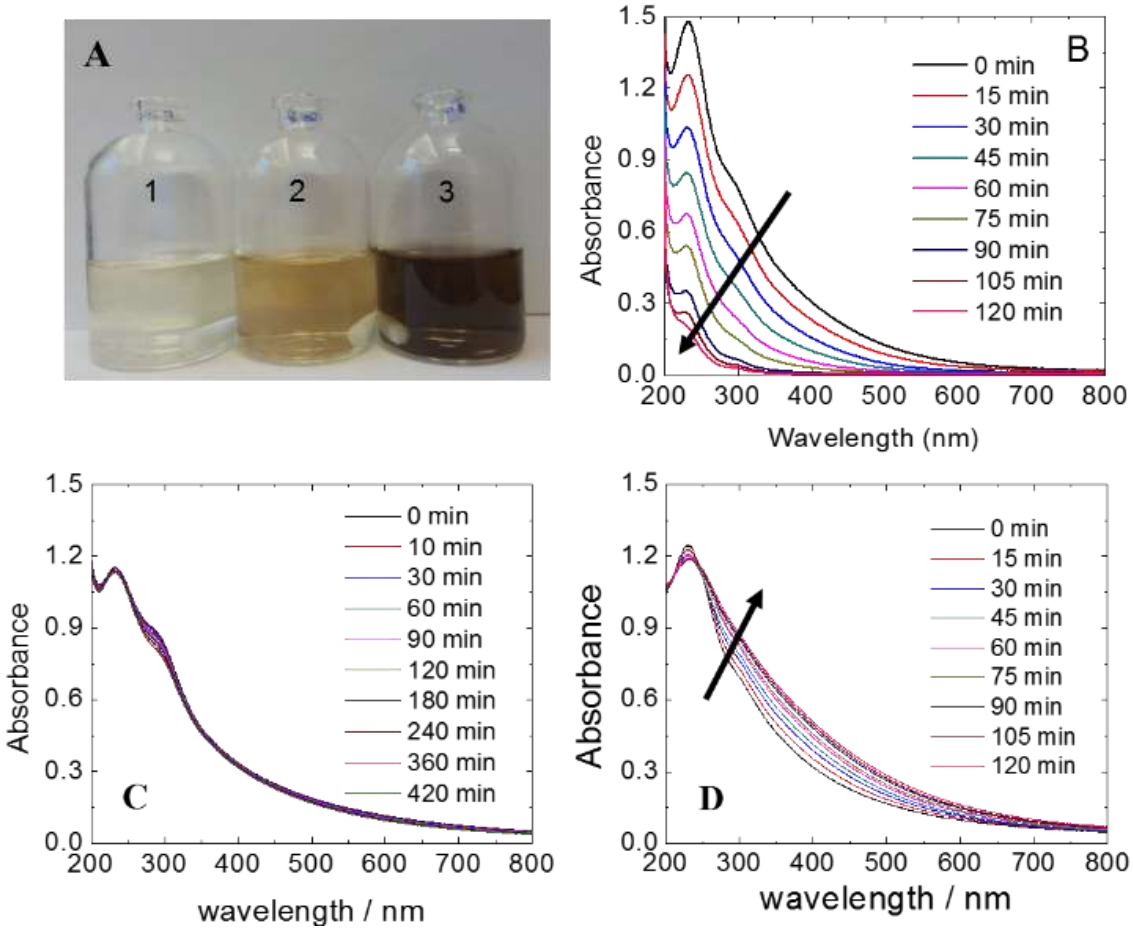

Figure 3.1 UV-vis spectra and photo of graphene oxide in UV/free chlorine system. 1A(1), 1B: GO (50 mg/L) with 200 mg/L free chlorine at pH 5 under UV irradiation (2000 μW/cm^2) for 2 h. 1A(2), 1C: GO (50 mg/L) with 200 mg/L free chlorine in dark. 1A(3), 1D: GO (50 mg/L) under UV irradiation (2000 μW/cm^2).

A graphene oxide suspension reacting with free chorine under UV irradiation (351 nm, 2000 μW/cm^{-2}) can be simply observed via solution color change (Figure 3.1A, samples 1), consistent with Du's report. [153] Corresponding UV-vis spectra change over time is shown in Figure 3.1B. According to Huang et al.,[116] the 230 nm peak in graphene oxide UV-vis spectrum corresponds to π-π* transitions, which is also observed for other nano-scale sp^2 carbon clusters.[154] In contrast

to the report by Li et al[149], where the UV-vis spectra did not significantly change, the loss of the 230 nm peak indicates sp^2 π carbon environment(s) are significantly altered, which is consistent with our previous research demonstrating fullerene oxidation in water[154] and others describing graphene oxide photo-transformation.[145] For control experiments without UV light (dark), absorbance response did not significantly change over time (Figure 3.1C), even with elevated concentrations of free chlorine (100 – 200 mg/L). We hypothesize that chlorine radicals generated by UV irradiation[143] and/or photo-excited GO[148] facilitate observed reactivity, whereby photoexcited GO is more vulnerable to the radical attack. Similar enhanced reactivity was observed for fullerene clusters under in the presence of free chlorine and UV irradiation.[143] In other control experiments, using the same intensity of UV light without free chlorine, the absorbance curve actually increases (Figure 3.1D), turning relatively darker, which is consistent with other researchers, suggesting graphene oxide (photo)reduction.[145, 148, 156] For these reactions, peak shifts were also observed (Figure 3.2) - a blue-shift was observed in GO-UV-free chlorine system while a red shift was observed in the control GO-UV system, consistent with the results of Yang et al[157] and Chen et al,[158] indicating that GO was oxidized in light-free chlorine system, as the material's band gap increased.

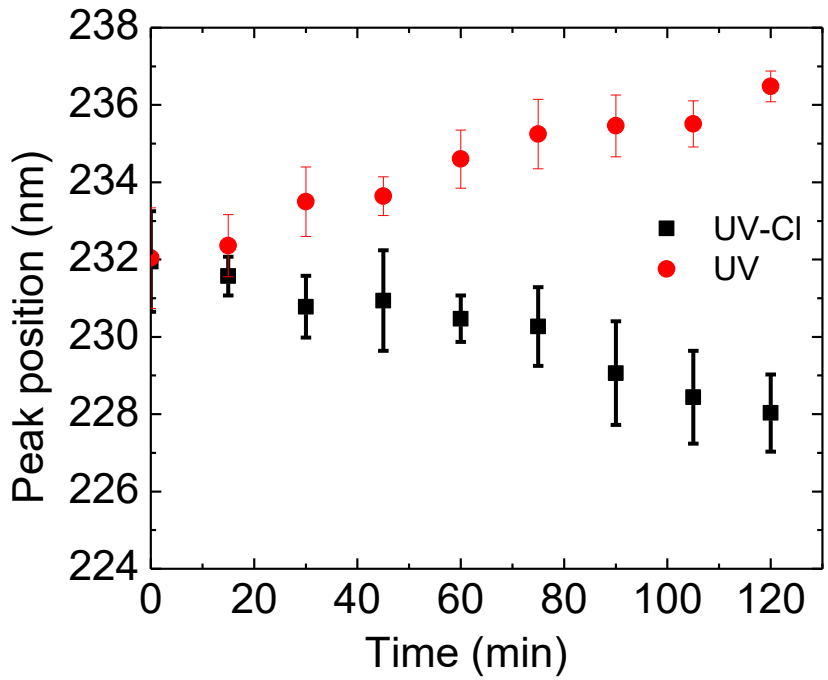

Figure 3.2 Peak position change in UV-vis spectra of GO with reaction time for 50 mg/L GO under UV irradiation (2000 μW/cm^2) for 2 hours at pH 5, with/without 200 mg/L free chlorine.

Peak UV-vis absorbance spectra around 230 nm was employed to monitor bulk, relative kinetics under varied concentrations of free chlorine (Figure 3.3A)[149, 159]. At given free chlorine concentrations, reactions are 1st order and can be described by the reaction rate (i.e. relative loss of sp^2 carbon) as:

$$-\frac{d[GO]}{dt} = k'[GO]$$

The k' for each free chlorine concentration was determined to be proportional to the initial free chlorine concentration (Figure 3.3B), and thus k' can be expressed as:

$$k' = k[Cl_2]_0$$

The overall relative reaction rate is expressed as:

$$-\frac{d[GO]}{dt} = k[GO][Cl_2]_0$$

This expression is 1st order with respect to GO and pseudo 1st order with respect to free chlorine (initial concentration). Note that in Figure 3A, at a given chlorine concentration, the reaction followed the stated kinetics until the free chlorine was consumed, whereby the absorbance stopped decreasing.

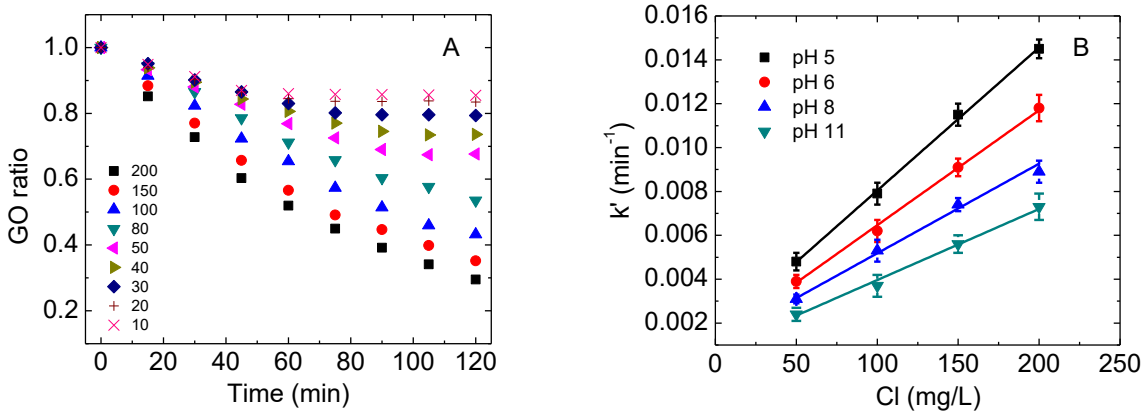

Figure 3.3 Kinetics of GO in UV/free chlorine system. 3.3A: GO ratio remained in the solution, which was taken from the absorbance of 230 nm in UV-vis spectra, under different free chlorine concentrations (mg/L) at pH 6 with UV irradiation (2000 μW/cm2). 3.3B: pseudo first order rate constants of GO with different free chlorine concentrations at different pH levels under UV irradiation (2000 μW/cm^2).

Rate constants (k) are observed to be sensitive to solution pH, with faster reactions occurring at lower pH (Figure 3.4). This trend is likely due (at least partially) to the different reaction mechanisms of radical generation from HOCl under different pH conditions, as:[143]

$$HOCl \xrightarrow{hv} \cdot OH + \cdot Cl$$

$$ClO^- \xrightarrow{hv} \cdot O^- + \cdot Cl$$

To explore the role of potential radicals, *tert*-butanol was employed as a scavenger to quench ·OH radicals.[160] Reaction rate constants in the presence of *tert*-butanol are shown in Figure 3.4, which decrease by over 60%, suggesting significant radical involvement. The difference of reaction rate constants between low pH and high pH after quenching with *tert*-butanol was not much, which is as expected since the reaction after quenching should only be the result of chlorine radical and other oxygen containing radicals. Note that the at higher pH, the HOCl produced negatively charged oxygen radical, which might be more difficult to react with negatively charged graphene oxide, and this contributed to the lower reaction rate under higher pH. In the control experiment with just *tert*-butanol and GO under light irradiation, GO was not significantly transformed based on the result of UV-vis spectra and XPS, suggesting that *tert*-butanol did not play a role in the transformation of GO other than quenching the radicals.

Since the reaction is between carbon species and chlorine, it is also important to include the scavenging effect of carbonate and chloride ions on the hydroxyl radical, as reported by Liao et al. [161] According to their research, at higher pH, chloride ions would have less scavenging effect but carbonate would have higher scavenging effect on hydroxyl radical. Since the chloride concentration used in this study was much lower than need to have effect on the hydroxyl radical, carbonate ion scavenging could be one of the reasons to lead to lower reaction rate at higher pH.

For gas-purged systems (i.e. low oxygen), rate constants were calculated and shown in Figure 3.4. Here rate constants decreased by ca. 30%, which indicated oxygen also plays a key role in the observed conversion of graphene oxide.

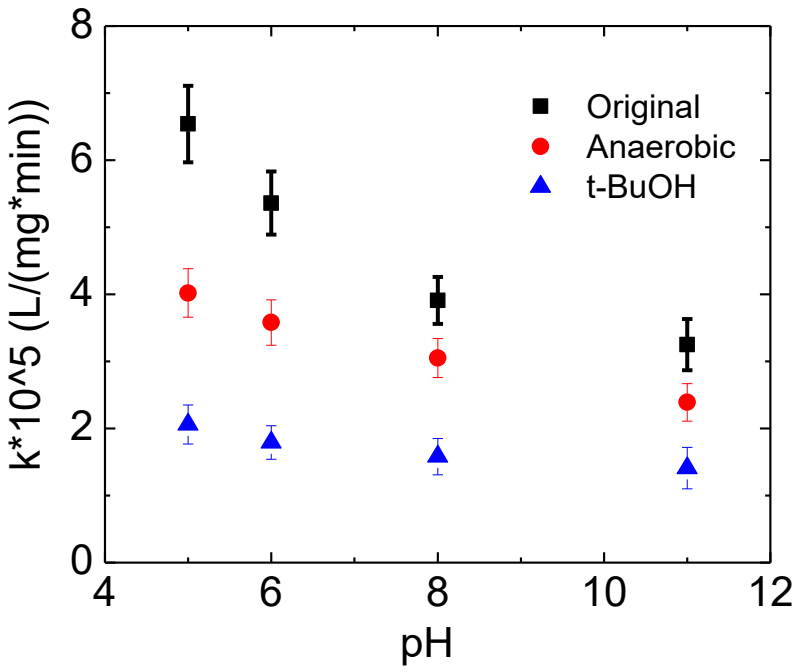

Figure 3.4 Reaction rate constants of GO reaction in UV/free chlorine system under different pH and the effect of dissolved oxygen and quenching agent *t*-BuOH (200 mM)

In addition to the aforementioned reaction variables, reaction kinetics are also significantly affected by the initial GO coupon size. According to dynamic light scattering (DLS) data, the average hydrodynamic diameter of parent GO was 352.6 nm and after filtering with 450 nm and 220 nm syringe filters, the diameters decreased to 327.3 nm and 147.5 nm, respectively. The reaction rate constants as a function of (initial) GO coupon size are summarized in Table 3.1. The reactions were conducted under same condition as discussed above. For these, smaller GO coupons were observed to be (relatively) more reactive. The rate constant increased from 6.54 to 14.30 × 10^{-5} L/(mg*min) when the average size decreased from 352.6 nm to 147.5 nm (at pH 5, 50 mg/L GO, 10 mM PBS and 50, 100, 150 and 200 mg/L free chlorine under light irradiation (2000 μW/cm^{-2}) for 2 hours). Similar increases in reaction rate (>100%) were

observed for all pH values. Note that before and after filtering with a 450 nm filter, rate constants did not significantly change as the average coupon size of GO after filtration (450 nm). As discussed by Li et al. for smaller coupon sizes, a relatively larger fraction of available edge-based carbon atoms, which are relatively more reactive, are available as active reaction site. [149]

Table 3.1 Reaction rate constants under different pH with GO in different size

pH	5	6	8	11
Parent GO (352.6 nm)*	6.54	5.36	3.91	2.84
450 nm filtered (327.3 nm)	6.57	5.88	4.29	3.13
220 nm filtered (147.5 nm)	14.30	11.68	8.56	6.34

Unit: 10^{-5} * L/(mg*min)
* Hydrodynamic diameter was measured by DLS.
** All kinetics study experiments were carried out with 50 mg/L GO (both before and after filtration), 10 mM PBS and 50, 100, 150 and 200 mg/L free chlorine under UV irradiation (2000 μW/cm^{-2}) for 2 hours.

In the reaction rate equation, the initial chlorine concentration was used. We also measured the actual chlorine decay during the photoreaction. The reaction kinetics is shown in Figure 3.5 with the squares representing chlorine concentration in GO/free chlorine system under light irradiation, while the circles representing chlorine concentration in water under light irradiation as control. In all conditions tested, after the chlorine was consumed i.e., concentration dropped to almost zero, another dose of free chlorine was added to perform another cycle of

reaction. First observation was the chlorine decay reaction was first order, which is consistent with the report by Feng et al.[162] With more cycles of reaction performed, the reaction rate constant in the GO/UV/free chlorine system increased, as shown in Figure 3.6. In the control experiment of chlorine decay without GO but under light irradiation, the reaction rate constant decreased as more cycles of reaction performed. One of the reasons could be that as the ionic strength became higher, the activity coefficients of the related species decreased, thus leading to lower observed reaction rate. Also this the observed net effect, even with more chloride ions in the system to scavenging the radicals, as reported by Liao et al, [161] which means the actual increase of the reaction rate due to more light penetration could be higher. But in all cases, the rate constant is always lower with the presence of GO, as summarized in Figure 3.6. One of the reasons could be that GO also absorbs energy from light irradiation and the quantum yield of free chlorine producing radicals would be lower compared to the control experiment without GO. That also explains why the chlorine decay rate increased in the GO/free chlorine system under light with more cycles of reaction since as GO was transformed and became transparent, it no longer competed with free chlorine in absorbing light energy, making the observed chlorine decay rate faster. In the control experiments with GO/free chlorine system and water/free chlorine system both in dark, the free chlorine concentration did not change much over 24 hours, indicating the importance of light irradiation in this reaction.

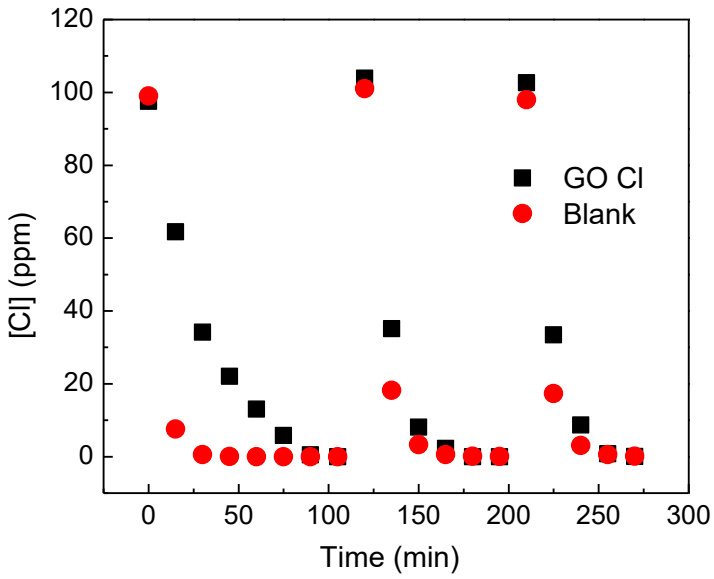

Figure 3.5 Free chlorine concentration during the GO/UV/free chlorine reaction. 100 ppm free chlorine was added at time 0, 120 and 210 min.

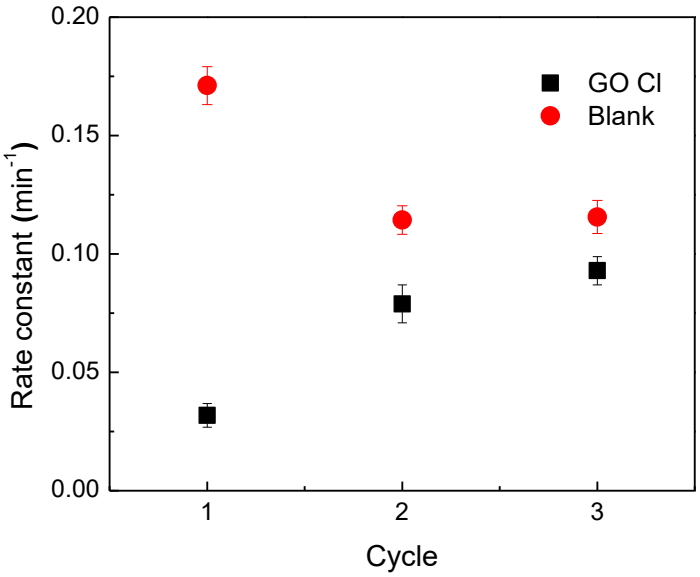

Figure 3.6 First order reaction rate constant of free chlorine decay under UV irradiation with and without GO in the system, for 3 cycles.

3.3.2 Product Characterization

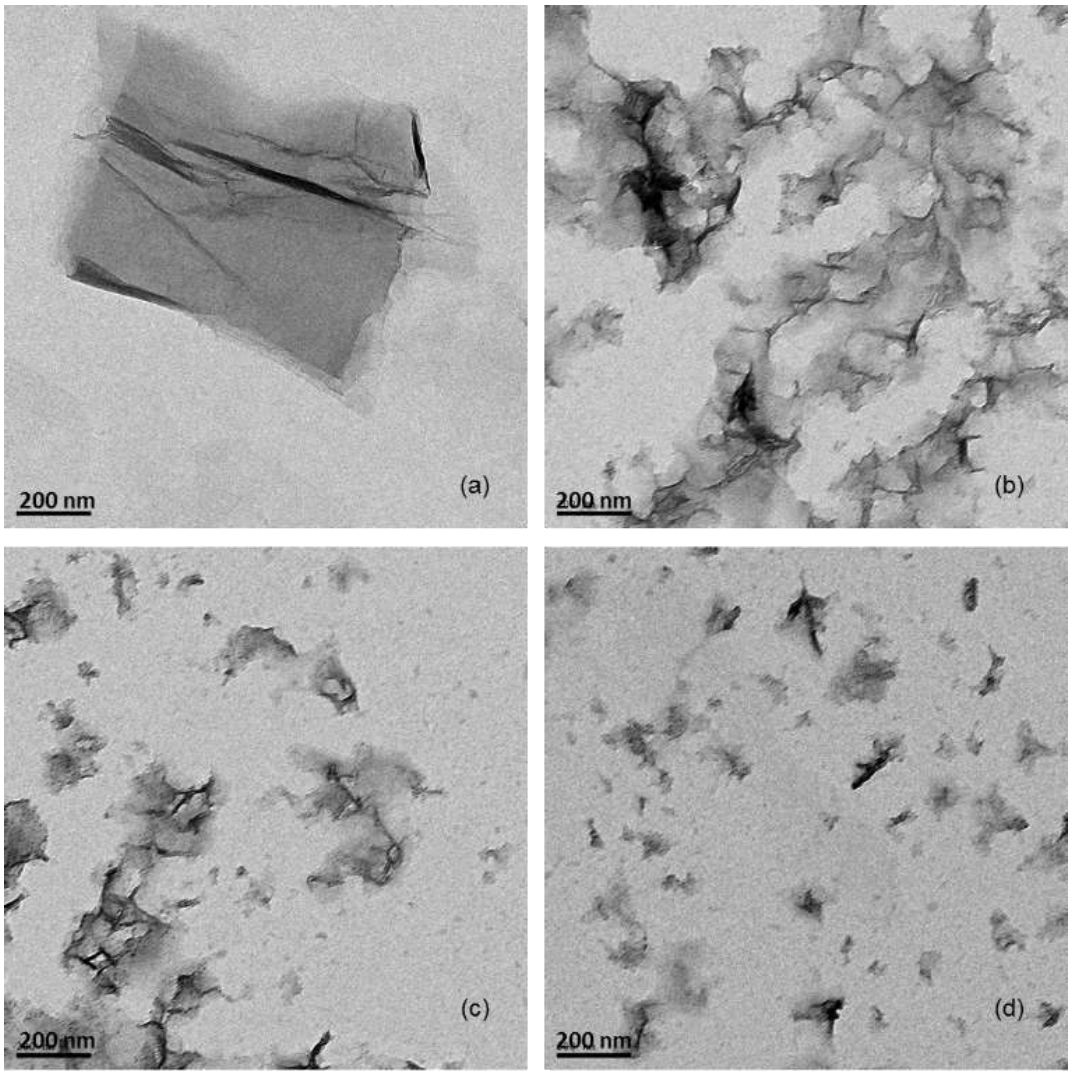

Figure 3.7 TEM images of GO and product with free chlorine under UV irradiation (2000 μW/cm^2) for 2 hours. (a) GO, (b) with 100 mg/L free chlorine at pH 5, (c) with 150 mg/L free chlorine at pH 5, (d) with 200 mg/L free chlorine at pH 5. All scale bars are 200 nm.

Figure 3.7 shows TEM micrographs before (a) and after (b, c and d) reactions with 100, 150 or 200 mg/L free chlorine under UVA irradiation (2000 μW/cm^2) for 2 hours at pH 5. After the reaction, GO (partial) products were observed as smaller coupons (not seen in the original GO samples, shown in Figure 3.7(a)), which is consistent with our UV-vis spectra (kinetic)

observations (Figure 3.2) whereby GO was transformed. Figure 3.8a shows Raman spectra of GO before and after the UV/chlorination reactions (200 mg/L free chlorine at pH 5). For graphene and graphene oxide materials, the D band at 1355.22 cm^{-1} indicates sp^3 carbon (defects) and the G band at 1602.86 cm^{-1} represents sp^2 regions (base graphene structure).[156] From Chapter 2, it was proved that the defect density of synthesized graphene oxide was in the region where I_D/I_G would decrease with more defect in the structure, thus the FWHM of G peak was used here to relative quantify the defect density.[51, 121, 163] As shown in Figure 3.8B, FWHM of original GO is 71.35 cm^{-1}, while after a UV/chlorination reaction the FWHM increased significantly for all conditions (up to 98.74 cm^{-1} with 200 mg/L free chlorine at pH 5 after 2 hours), indicating relatively more defects or smaller sp^2 domains in terms of average size, further confirming sp^2 network disruption and/or destruction. This is consistent with the result by Zhao et al. [145]

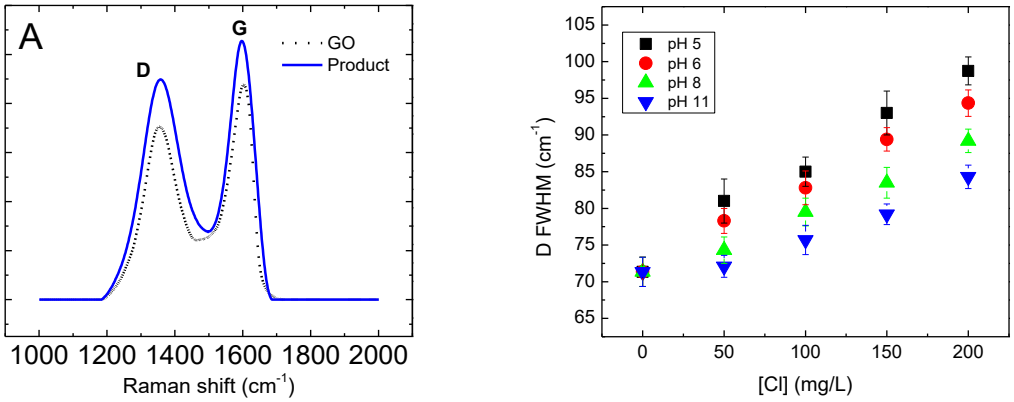

Figure 3.8 Raman spectra of GO and product. A: GO before and after reaction with 200 mg/L free chlorine at pH 5 under UV irradiation (2000 μW/cm^2). B: D/G ratio of GO after reaction with free chlorine at different pH levels under UV irradiation (2000 μW/cm^2) for 2 hours.

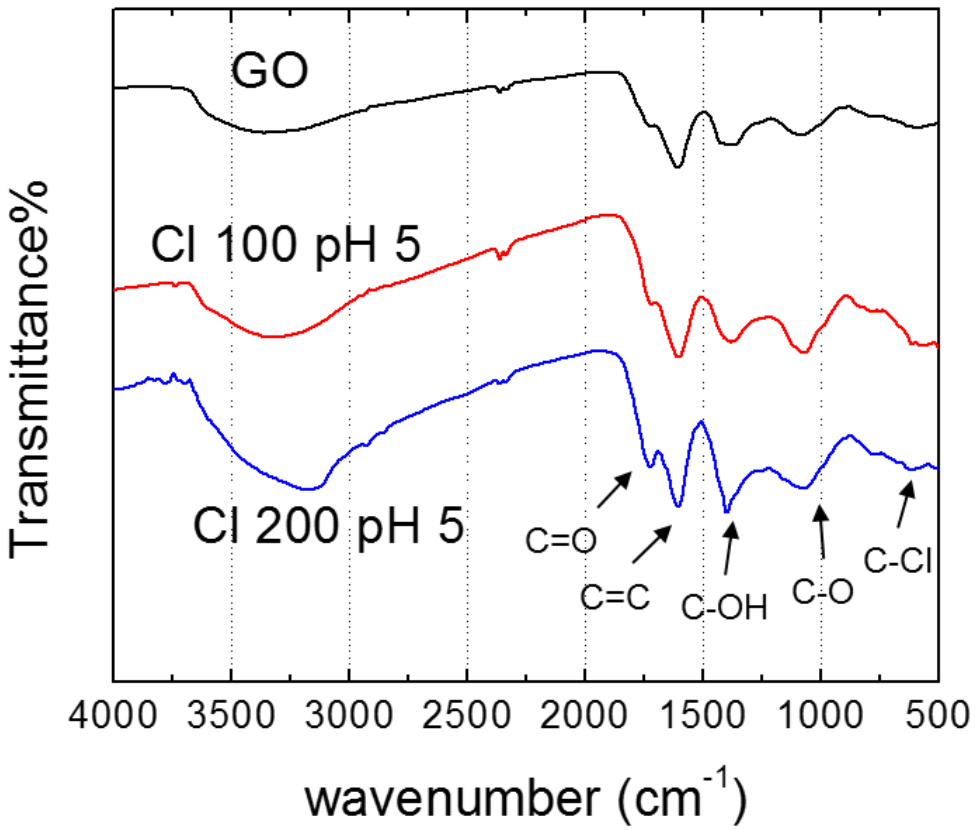

Figure 3.9 FTIR spectra of GO reactions at pH 5 with 100 mg/L and 200 mg/L free chlorine under UV irradiation (2000 μW/cm^2) for 2 hours.

Figure 3.9 shows FTIR spectra of GO before and after reactions (with 100 and 200 mg/L free chlorine under UV irradiation), using a DRIFTS technique (described above), from 500 – 4000 cm^{-1}. For parent material, characteristic C-O (1060 cm^{-1}), C-OH (1365 cm^{-1}), C=C (1600 cm^{-1}), C=O in carboxyl group (1720 cm^{-1}) and O-H (3400 cm^{-1}) were clearly observed.[164] Upon reactions with UV/free chlorine, peaks representing C-O, C-OH, C=O and O-H group all relatively increased compared to C=C abs. peak. Also observed absorbance at 500 – 800 cm^{-1} can be attributed to C-Cl stretching.[143, 165, 166] Higher chlorine concentration (200mg/L) resulted in relatively more oxygen functionality (i.e. larger abs. peaks). XPS was employed to (relatively)

quantify the carbon oxidation state (Figure 3.10). For these measurements, the 284.8 eV peak was assigned to the sp^2 hybridized carbon atoms, the 286.6 eV peak was assigned to the monooxidized carbon (e.g. C-O, C-OH) and the 288.3 eV peak was assigned to the deoxidized carbon atoms (e.g. C=O).[108] Upon reacting with 200 mg/L free chlorine under UVA, the total (relative) oxidized carbon (C-O and C=O) increased from 24.24% to 60.15%, in contrast to Li et al.[149] While there was still ca. 40% of the C=C/C-C environments remained (decreased from 75.76% to 39.85%), and carbon in C=C vs. C-C were not distinguished here in the XPS spectra, as the difference between the two peaks is very small and is reported differently by researchers[167]. We also note that while monooxidized carbon increased, dioxidized carbon relatively decreased, which may be due to the fact that the carbon in a C=O bond is more electrophilic (compared to monooxided carbon), thus more readily attacked by radical species. Also note that in the spectrum, we did not find strong chlorine signal, indicating the final product is not chlorinated.

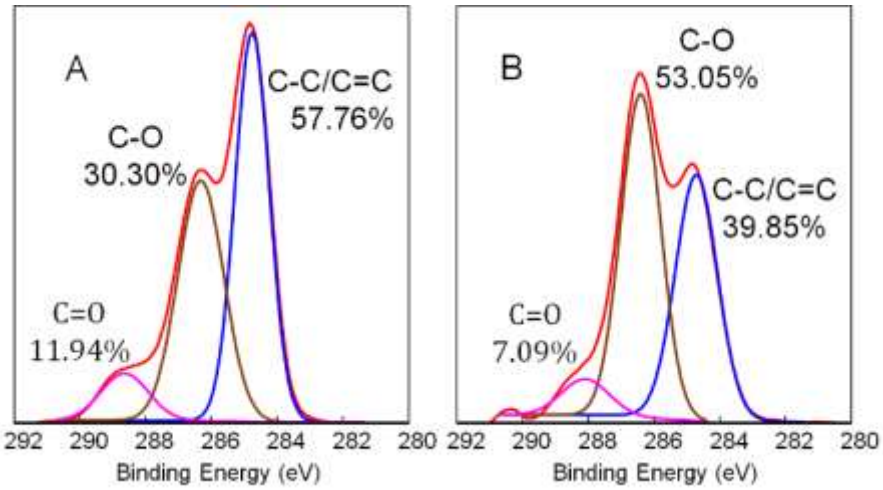

Figure 3.10 XPS spectra of (a) GO and (b) GO after reaction with 200 mg/L free chlorine at pH 5 under UV irradiation (2000 μW/cm^2) for 2 hours.

3.3.3 Carbon Mass Balance Analysis

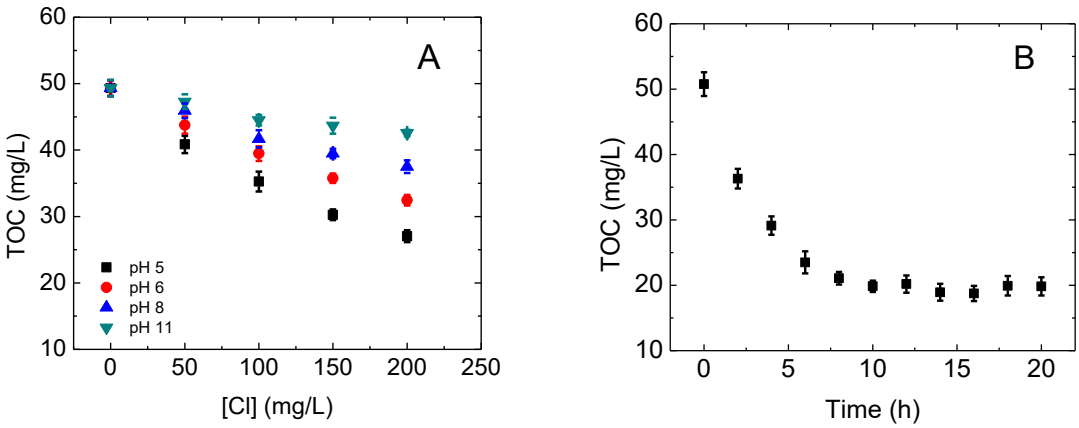

Figure 3.11 Total organic carbon after reaction with free chlorine under UV irradiation in open system. A: TOC after reaction with free chlorine under UV irradiation (2000 μW/cm^2) for 2 hours at different pH levels. B: Long-term study of TOC change for the reaction of GO with free chlorine at pH 5 under UV irradiation (2000 μW/cm^2). Additional 200 mg/L free chlorine was applied to the solution every 2 hours.

To confirm the assumption of GO mineralization during this reaction, Total Organic Carbon (TOC) analysis over the course of a typical reaction is shown in Figure 3.11. After 2 h reaction, with varied concentrations of free chlorine under light irradiation and different pH levels, TOC decreased from 50 mg/L (C_0) to as low as 30 mg/L (200 mg/L free chlorine at pH 5) suggesting partial mineralization (GO → CO_2). This is in line with Hou's research, whereby GO was also partially mineralized upon UV irradiation.[148] It should be noted that their light intensity (0.065 W/cm^2) was much higher than the intensity used in this study (2000 μW/cm^2). After 10 h, there is a ca. 25% carbon loss in their study; here, we observe nearly 40% carbon loss after 2 h in the UV/free chlorine system at pH 5 with 200 mg/L free chlorine. Interestingly, for a 20-hour reaction, the total organic carbon decreased to 20 mg/L after 10 h and remained steady, even though 200 mg/L free chlorine was added every 2 hours during the 20-hour reactions (total of 2000 mg/L free chlorine was added over the course of the reaction) shown in Figure 3.11B,

indicating that the product of GO transformation is resistant to radical transformation under such condition. Another possible reason that could prevent the further transformation is that as the chloride ions was accumulated in the system, the scavenging effect on hydroxyl radicals became more significant, according to Liao et al. [161]

Since GO could be treated as the derivative of poly-aromatic hydrocarbon (PAH) with molecular size of hundreds of nanometers, and based on the TEM we assume that GO could be transformed to smaller molecules in the presence of free chlorine and light irradiation, this transformation may lead to the production of PAHs, PAH oxides or chlorinated PAHs. To determine the product molecular weight distribution, we used stir cell and nano-filtration membranes to filter the solution after reaction and measured the TOC of the filtrate. The results are summarized in Figure 3.12. We can see that initially there was very little organic carbon with molecular weight less than 100 kDa. In the 6 hours reaction period, the total organic carbon decreased as confirmed in the previous content, the portion of small molecules (less than 100 kDa) was increasing, indicating that the graphene oxide was transformed into product with smaller molecular weight. After 6 hours reaction, product with molecular weight less than 1 kDa consisted 37.1% of the organic carbon remaining in the solution, indicating the production of small molecules.

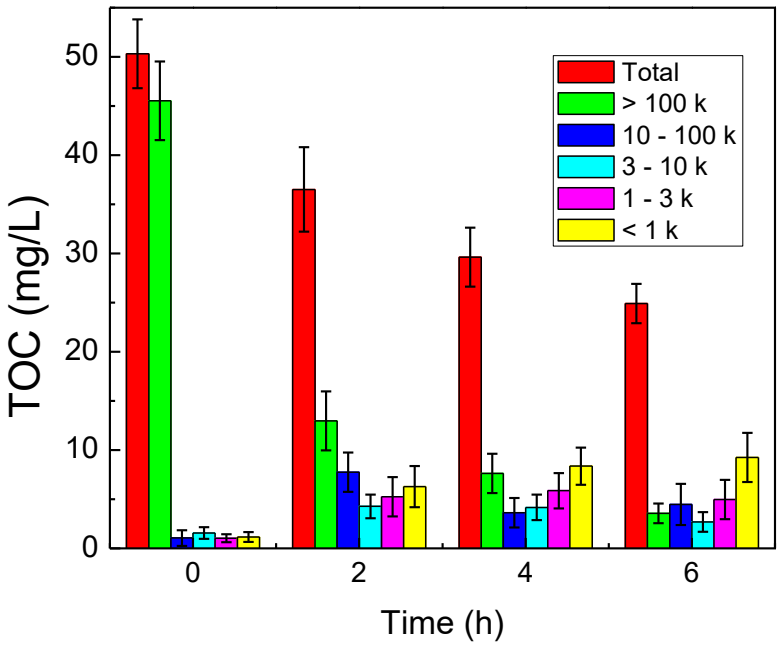

Figure 3.12 Product molecular weight distribution from filtration. GO (50 ppm) with 200 ppm free chlorine under light irradiation at pH 5.

To further explore GO transformation with regard to molecular weight analysis MALDI-TOF-MS was employed (Figure 3.13). For parent material, GO is beyond the detection range thus not shown on the spectrum. Further, during typical GO synthesis (modified Hummers method), smaller coupons are removed and thus we see no response in the 400 – 1500 m/z range. And in the control experiment without GO, i.e., only free chlorine in water under light irradiation, all peaks in the mass spectrum were below 90 m/z and no response in the 400 – 1500 m/z range, either. After the reaction, new mass (m/z) peaks in the range of 200 – 1000 m/z were observed, indicating small(er) molecular weight products were generated during the transformation of GO by UV/free chlorine. Also we included some possible molecular structures corresponding to each molecular weight peaks detected. Due to the lack of additional structural

information, we are unable to identify these exact products. Nevertheless, the results support the conclusion that GO is transformed into relatively smaller products under the stated conditions. One thing to notice is that we did not find any peaks with possible chlorinated molecules, to address the concern of possible production of toxic hazards.

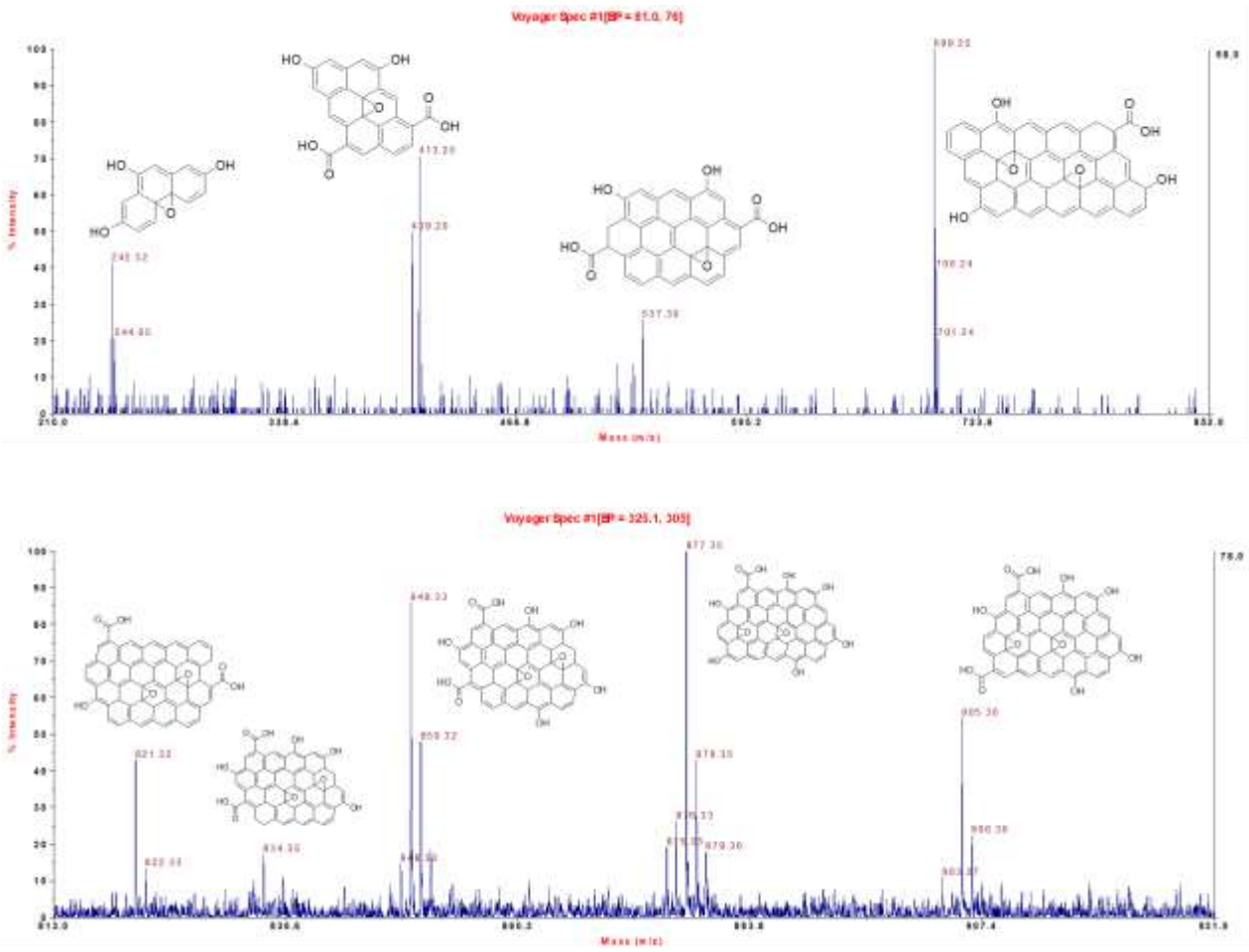

Figure 3.13 MALDI-TOF-MS results of GO after reaction with 200 ppm free chlorine at pH 6 under light irradiation (2000 μW/cm^2) for 2 hours, with possible product chemical structures based on the m/z value.

To close the carbon balance and confirm the CO_2 generation, CO_2 generation in gas phase for a closed reactor was monitored. Figure 3.14 shows increasing CO_2 concentration in the gas phase with correspondingly decrease in TOC (liquid phase) for 100 mg/L, 200 mg/L and 400

mg/L free chlorine with UV irradiation (2000 μW/cm^2). Detailed data is shown in supporting information (Table S3.1). The total carbon in the system remained constant throughout the 4 h reaction time with 400, 200, and 100 mg/L free chlorine. Two sets of control experiments were conducted. One was GO with chlorine under dark condition and the other was GO without chlorine under UV irradiation. For both, no significant CO_2 generation in the gas phase was observed (Figure 3.14D). Data for these control experiments are also summarized in supporting information in Table S3.1.

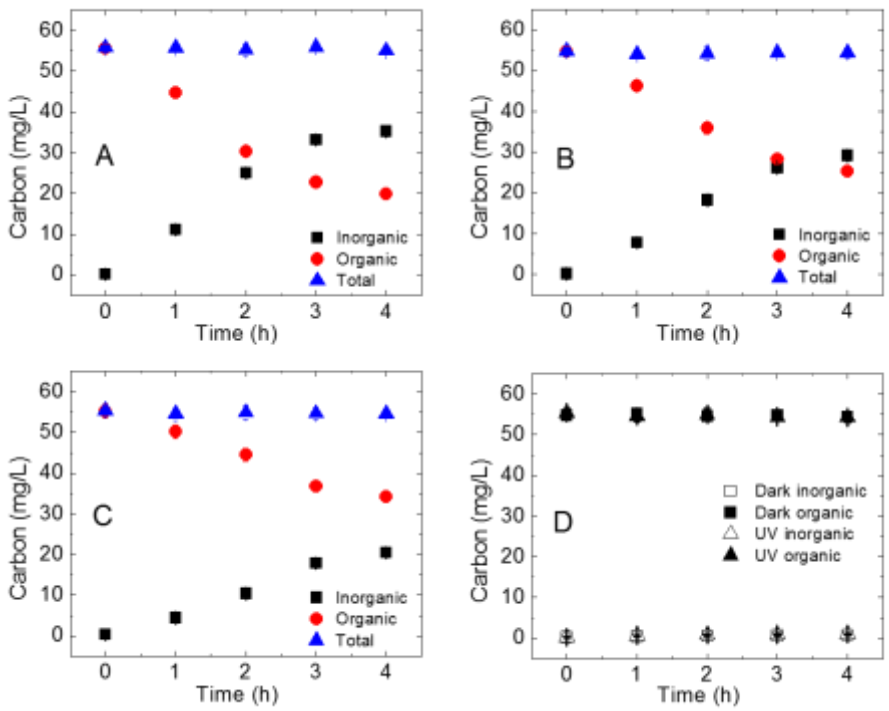

Figure 3.14 Carbon mass balance between the gas phase and liquid phase in closed system. Reaction were carried with 50 mg/L GO at pH 5 with 400 (10A), 200 (10B) and 100 (10C) mg/L free chlorine under UV irradiation (2000 μW/cm^2). The solid symbols represent the carbon remaining in the liquid phase (TOC and liquid CO_2) and the empty symbols represent the carbon in gas phase (CO_2) for each free chlorine concentration. 10D: control experiments (1) in dark with 400 mg/L free chlorine and (2) without free chlorine under UV irradiation (2000 μW/cm^2).

3.3.4 Reaction Mechanism

Given the above result and discussion, we proposed the following reaction mechanisms, as shown in Figure 3.15. The hydroxyl radical played an important role in the transformation of GO, while chlorine radical also contributed to the overall reaction. Being different from the reaction reported by Ma et al., [146] where hydroxyl radical was the only cause of the transformation, GO was significantly transformed and produced small molecules with the presence of free chlorine, even though the major product was not chlorinated, according to XPS and MS results. So we assume that GO was first activated by the chlorine radicals, forming chlorinated GO. The chlorinated carbon atoms would be more reactive than the carbon atoms in the original GO, especially on the basal plane， since it would be more electrophilic and vulnerable to radical reaction. Then under the attack of ·OH radical, the chlorinated GO was further transformed into CO_2 and smaller GO, even PAH oxides, with the dissociation of chlorine atoms as chloride ions. This mechanism could explain the importance of the chlorine radical as well as hydroxyl radical in transforming GO into smaller molecules.

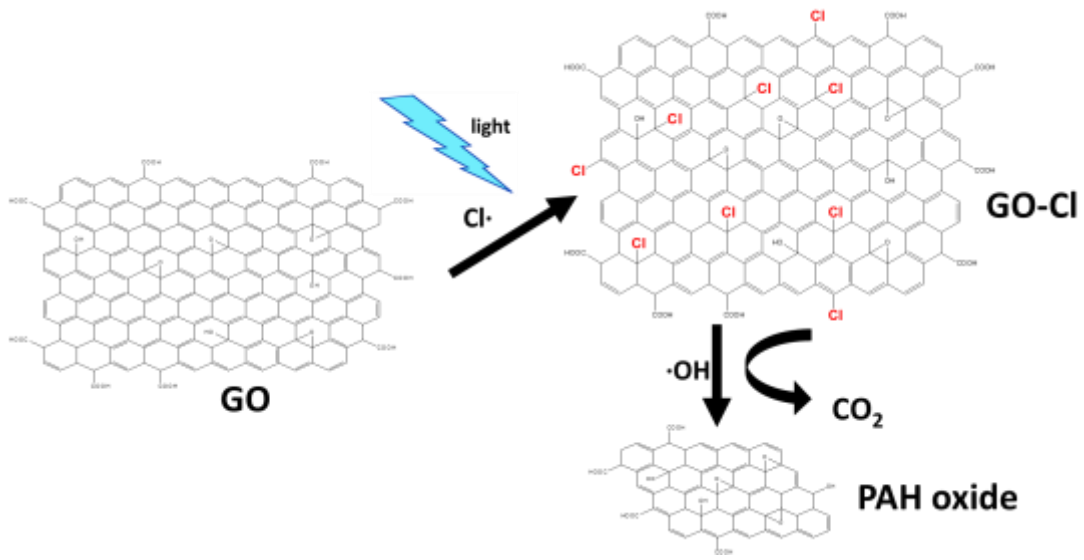

Figure 3.15 Proposed reaction mechanism for GO in the presence of free chlorine and light irradiation.

3.4 Conclusions

To date, the vast majority of reports regarding graphene materials are focused on the development of new technologies and the fate and transport in natural systems. In contrast, underwhelming attention has been paid to the potential chemical and physical transformations that graphene and graphene oxides will undergo when exposed to (environmentally) relevant conditions, including typical water treatment processes. In this work, data sets clearly demonstrated that graphene oxide is susceptible to extensive transformation when exposed to free chlorine and light irradiation. Under conditions described, partial mineralization was also observed with remaining products resistant to further oxidation (i.e. stable daughter product). Further, it is proved that upon such oxidation, graphene oxide will produce PAH oxides. Also it is hypothesized that GO will become more hydrophilic, thus its partitioning behaviour and reactivity will change accordingly (and likely significantly). Considering these results, aqueous-based technologies utilizing graphene oxide materials/composites should consider potential material transformation processes as stability and performance may be affected.

Chapter 3: Supporting Information

S3.1 Instrumentation.

The original GO and product were analyzed using transmission electron microscope (TEM). Instrument Tecnai G2 Spirit from FEI Company, operating at 120 kV. Total organic carbon analysis (TOC) was performed by TOC-L TOC analyzer from Shimadzu, with ASI-L auto sampler, using potassium hydrogen phthalate as a carbon standard. 0.1 M HCl was applied to the sample to facilitate removal inorganic carbon from the system (as CO_2). Fourier transform infrared spectroscopy (FTIR) was used for the oxygen containing functional groups on the GO molecules. After washing and drying under vacuum for 24 h, the powder was mixed with KBr to perform DRIFTS in the range of 4000 – 500 cm^{-1} at a resolution of 0.5 cm^{-1} for 4000 cycles. The instrument was Thermo Nicolet NEXUS 470 FTIR from Thermo Scientific. To quantitatively describe the reaction kinetics, UV-vis spectra was measured at each time interval during the reaction. Samples of 750 μL were put into a cuvette and measured for the absorbance over the wavelength range of 200 – 800 nm. The instrument was Varian Cary 50 Bio UV-Visible Spectrophotometer from Varian, Inc. Raman spectra were performed over a range of 3200 – 100 cm^{-1} with resolution of 1.2 cm^{-1}. The solution was dropped onto silicon wafer substrates and dried in a vacuum for 24 h before measuring. The instrument was InVia Confocal Raman microscope from Renishaw. X-ray Photoelectron Spectroscopy (XPS) was used to determine the relative quantity of each oxidation state of C atoms. The solution was dropped onto silica wafer and dried for 24 h before measuring. The instrument was PHI 5000 Versa Probe II from ULVAC-PHI, Inc. Three measurements at different positions were performed for each sample and the average value was calculated. The instrument was PHI 5000 Versa Probe II. The peaks were fit using a mixed fit of 80% Gaussian and 20% Lorentzian characters in the PHI Multipak

software. Peak position calibration was carried out by aligning the C 1s peak (C-C/C=C) with its reference position at 284.8 eV, and a Shirley background subtraction was performed. Gas phase CO_2 concentration was measured by gas chromatography. The instrument was Agilent 7890B GC System from Agilent Technologies. Matrix-Assisted Laser Desorption/Ionization (MALDI) Time-of-Flight Mass Spectrometry was used to examine products with smaller molecular weight. The instrument was Voyager-DE STR Biospectrometry Workstation from Applied Biosystems.

S3.2 DPD colorimetric method for free chlorine concentration measurement.

PBS: dissolve 24 g anhydrous Na_2HPO_4 and 46 g anhydrous KH_2PO_4 in distilled water. Combine with 100 mL distilled water in which 800 mg disodium EDTA is dissolved. Dilute to 1 L. DPD (N,N-Diethyl-p-phenylenediamine) solution: dissolve 1.1 g anhydrous DPD sulfate in distilled water containing 8 mL 1+3 H_2SO_4 and 200 mg disodium EDTA. Dilute to 1 L. 1 mL sample was added to the solution containing 8 mL water, 0.5 mL PBS and 0.5 mL PDP solution. After 5 min, the absorbance at 515 nm on UV-vis spectrum was measured and it is linearly related to the free chlorine concentration. Noted that the higher limit of this method is 3 ppm so the samples were diluted to make the chlorine concentration below 3 ppm, before adding it to the DPD solution. The calibration curve is shown in Figure S3.1.

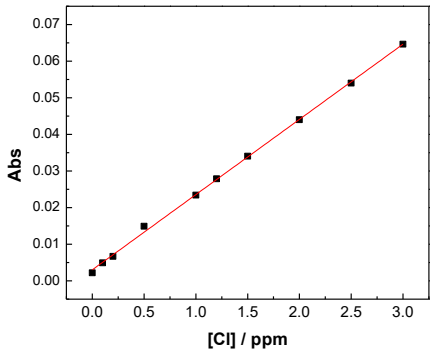

Figure S3.1 Calibration curve of free chlorine concentration measurement by DPD colorimetric method.

S3.3 Carbon mass balance result from gas phase and aqueous phase.

Table S3.1 Carbon mass conservation for 400 mg/L free chlorine reaction (sealed system)

Time/h	Gas phase	TOC	Dissolved CO2	Total
0	0.12	55.66	0.11	55.89
1	5.88	44.76	5.17	55.81
2	13.30	30.29	11.71	55.30
3	17.67	22.72	15.55	55.94
4	18.76	19.81	16.52	55.09

Unit: mg/L as carbon

Table S3.2 Carbon mass conservation for 200 mg/L free chlorine reaction (sealed system)

Time/h	Gas phase	TOC	Dissolved CO2	Total
0	0.10	54.68	0.08	54.86
1	4.15	46.26	3.66	54.07
2	9.73	35.97	8.57	54.27
3	13.95	28.27	12.28	54.50
4	15.52	25.28	13.67	54.47

Unit: mg/L as carbon

Table S3.3 Carbon mass conservation for 100 mg/L free chlorine reaction (sealed system)

Time/h	Gas phase	TOC	Dissolved CO2	Total
0	0.14	55.16	0.13	55.43
1	2.35	50.18	2.06	54.59
2	5.52	44.54	4.85	54.91
3	9.51	36.81	8.37	54.69
4	10.88	34.15	9.58	54.61

Unit: mg/L as carbon

Chapter 4: The Effect of Free Chlorine and Light Irradiation on Graphene Oxide Membrane: Stability and Water Flux

Abstract

In the previous chapter, free chlorine was demonstrated to readily and significantly transform aqueous-based graphene oxide, which has potential to impact graphene oxide membrane performance. In this chapter, simple graphene oxide membranes are synthesized via wet vacuum method and chlorination under light irradiation was subsequently applied and evaluated with regard to membrane integrity and performance. When exposed to free chlorine under UVA light irradiation membrane oxidation is observed while for the dark conditions no change in the carbon oxidation state occured. TOC showed 15.44% of the carbon was dissolved (separated from the membrane) after 2 hours reaction with 100 mg/L free chlorine under UVA irradiation. The transformation was more significant at lower pH. Water flux and surface roughness increased after reaction with free chlorine for 2 hours but decreased after 4 hours reaction due to the photo-reduction of graphene oxide upon the depletion of free chlorine.

4.1 Introduction

Given the potential of graphene oxide application in water treatment membranes, understanding GO chemical stability under cleaning/reactive conditions is critical. Fouling is the major obstacle for membrane application(s), which we describe as the accumulation of rejected components and even biofilm formation – which lead to decrease in water flux or increase in required pressure.[168] As a common strategy to control membrane fouling, adding free chlorine to the feed solution is widely used.[169, 170] However, for graphene/graphene oxide membranes, free chlorine will likely

react with available aromatic and nitrogen groups potentially degrading membrane integrity and performance.[171] Chae et al. synthesized graphene oxide embedded polyamide membrane and showed improved chlorine resistance, whereby the water flux increased from 14 L/(m*h*bar) to 21 L/(m*h*bar) after chlorination while it increased from 5 L/(m*h*bar) to 33 L/(m*h*bar) in the case of the membrane without graphene oxide.[172] Safarpour et al. applied interfacial polymerization of monomers with reduced graphene oxide and TiO_2 nanoparticles to synthesize thin-film membranes and found the rejection of salt decreased after chlorination.[173] However, the research was only done under dark conditions and the effect of possible sunlight irradiation or UV application has not been taken into consideration to date. In Chapter 3, the free chlorine under light irradiation was demonstrated to react with graphene oxide in aqueous solution, which was enhanced under light. We have extended that framework here to a simple GO membrane system.

In this chapter, graphene oxide was deposited onto substrate to form a laminate type membrane, and then free chlorine and light irradiation were applied. The effects of pH and reaction time are also explored and described. The oxidation state of graphene oxide, chemical stability, and surface roughness of the membrane and water flux before and after the reaction were evaluated and reported.

4.2 Materials and Methods

4.2.1 Materials

Graphite powder, sulfuric acid, potassium permanganate and hydrogen peroxide solution were purchased from Sigma-Aldrich and used for graphene oxide synthesis. Polyallylamine solution (PAA, average Mw ~ 17,000 Da, 20 wt. % in H_2O, ρ = 1.02 g/mL) was also purchased from

Sigma Aldrich. All chemicals were reagent grade or higher and used without further purification, unless otherwise noted.

4.2.2 Graphene Oxide Membrane Synthesis

Graphene oxide was synthesized with temperature of 30 °C in stage 1 and 60 °C in stage 2, reaction time of 2 hours in stage 1 and 60 min in stage 2, oxidant ratio of 3:1, followed by washing, drying, sonication (2 hours) and centrifuge, as described in the previous chapter.

Graphene oxide was deposited on the poly(ether sulfone) (PES) support membrane (Sterlitech, nominal pore size 0.03 μm as provided by the manufacture) using wet vacuum filtration. As previously reported in our lab, polyallylamine (PAA, Sigma Aldrich, Mw ~ 17000, 20 wt. % in H2O) was used as a cross-linker to enhance graphene oxide assembly stability during the membrane synthesis.[90] PAA is a long alkyl polymer with reactive amine groups on the carbon chain which could readily react with the oxygen groups on the graphene oxide. The amine groups of PAA readily reacted with the oxygen-containing functional groups on graphene oxide materials. GO (1 mg) and PAA (10 μL) mixture was sonicated for 2.5 h in a bath sonicator (Branson 2510MT, Bransonic®), and then vacuum filtered onto a PES support membrane. The PES membrane was also soaked in a 2 wt. % PAA aqueous solution for 3 h before the deposition to enhance the interaction between the top layer (graphene oxide) and the support (PES). The final membrane assembly was then air-dried and used in subsequent characterization and performance evaluations.

4.2.3. Chlorination experiments

The graphene oxide membrane was attached onto the wall of quartz beaker, then the solution containing free chlorine and adjusted to target pH level was added into the beaker to ensure the membrane was immersed into the solution. The free chlorine concentration used in this study

included 10 mg/L, which was similar to the dose used in disinfection process in water treatment, and, 50 mg/L and 100 mg/L to accelerate the reaction to better illustrate the possible effect of free chlorine on the graphene oxide membrane. The pH level included 5, 7 and 9. For dark reaction, the beaker was wrapped with aluminum foil and kept in the dark. For the photo-reaction, the beaker was placed in a photo-reactor with UV lamp in it. The light irradiation wavelength was centered at 351 nm and the intensity was 2000 μW/cm^2, which intended to simulate the sunlight irradiation. The beaker was magnetically stirred for 2 hours and 4 hours, respectively.

4.2.4. Membrane Permeability

To evaluate the performance of graphene oxide membrane before and after reaction with free chlorine, the permeability was tested according to established procedures.[90] The water flux was measured under a direct flow dead-end filtration mode. MilliQ water was placed in the storage tank (Millipore Amicon 8050) and pressurized by N_2 and connected to the filter holder (47 mm, Pall Life Science) where the membrane was placed. The permeate was measured directly using an integrated electronic balance (Mettler Toledo ML1502E) with the weight data automatically logged at 60 second interval. The constant pressure of 1.5 bar was maintained throughout the measurement and kept the same for all conditions. Then water flux (L/(m^2 h bar)) was calculated as followed:

$$flux = \frac{(w_{t+dt} - w_t)}{\rho \times dt \times A \times p}$$

where w_t is the weight of accumulated permeate with unit of g, dt is the time interval (60 s), ρ is the density of water with unit of g/L, A is the effective membrane surface area with unit of m^2 and p is the pressure across the membrane, which is 1.5 bar here in this study.

4.2.5. Characterization

The oxidation state of the carbon on the membrane was characterized by X-ray photoelectron spectroscopy (XPS). The membrane sample was dried in vacuum chamber before measuring. After reaction, the solution was analyzed by total organic carbon analysis (TOC) to evaluate the chemical stability of the membrane. Atomic force microscopy (AFM) was used to characterize the surface roughness of the membrane before and after the reaction. The arithmetic average roughness (R_a) and geometric average roughness (R_q) were used to evaluate the effect on the surface.

4.3. Results and Discussion

4.3.1 Chemical Stability

As shown in Chapter 3, graphene oxide is transformed into smaller coupons and becomes more hydrophilic when exposed to chlorine under UVA. For studied graphene oxide membranes in contact with free chlorine under light irradiation, we also evaluated potential transformation and dissociation from the membrane surface into the aqueous phase. Total organic carbon (TOC) analysis was conducted on the solution after reactions under different conditions. TOC data and solution volume, the percentage of carbon dissolved in the aqueous phase is summarized in Figure 4.1. Under dark conditions, less than 2% of the carbon was dissolved after 2 hours in water. With the addition of the free chlorine, the carbon loss increased to 4.5% with 10 mg/L free chlorine. Given that the free chlorine concentration would likely be less than 10 mg/L in a typical disinfection process, less than 5% of the graphene oxide loss would may be expected per

dose, depending on the contact time. In contrast with the free graphene oxide in aqueous solution, which was not detected to be transformed in dark condition with 200 mg/L free chlorine, the carbon loss increased to 7.82% with 50 mg/L free chlorine and 9.11% with 100 mg/L free chlorine. The reason could be attributed to that the interaction between graphene oxide, the cross-linker polymer and the PES membrane was disrupted by the addition of free chlorine. The specific reason though was not explicitly determined.

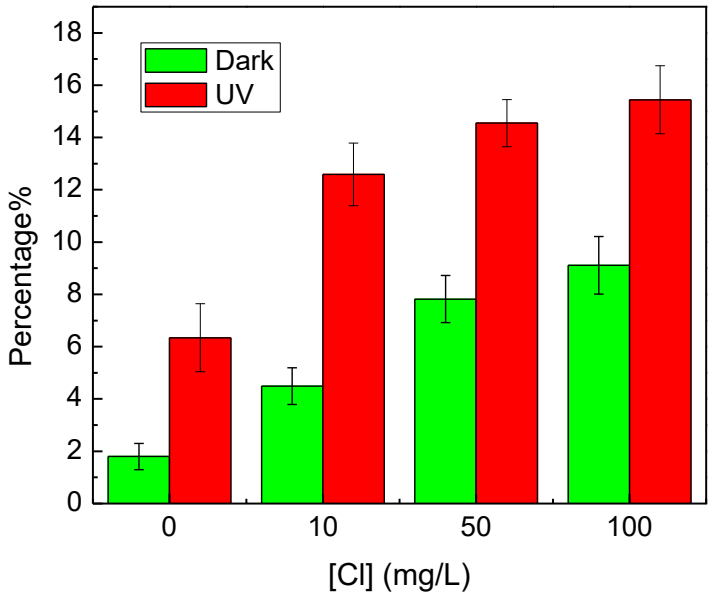

Figure 4.1 Carbon dissolved in the aqueous solution after 2 hours reaction of GO membrane with different concentration (0, 10, 50, 100 mg/L) of free chlorine at pH 7, both in dark and under light irradiation (2000 μW/cm^2)

4.3.2. Carbon Oxidation State Change

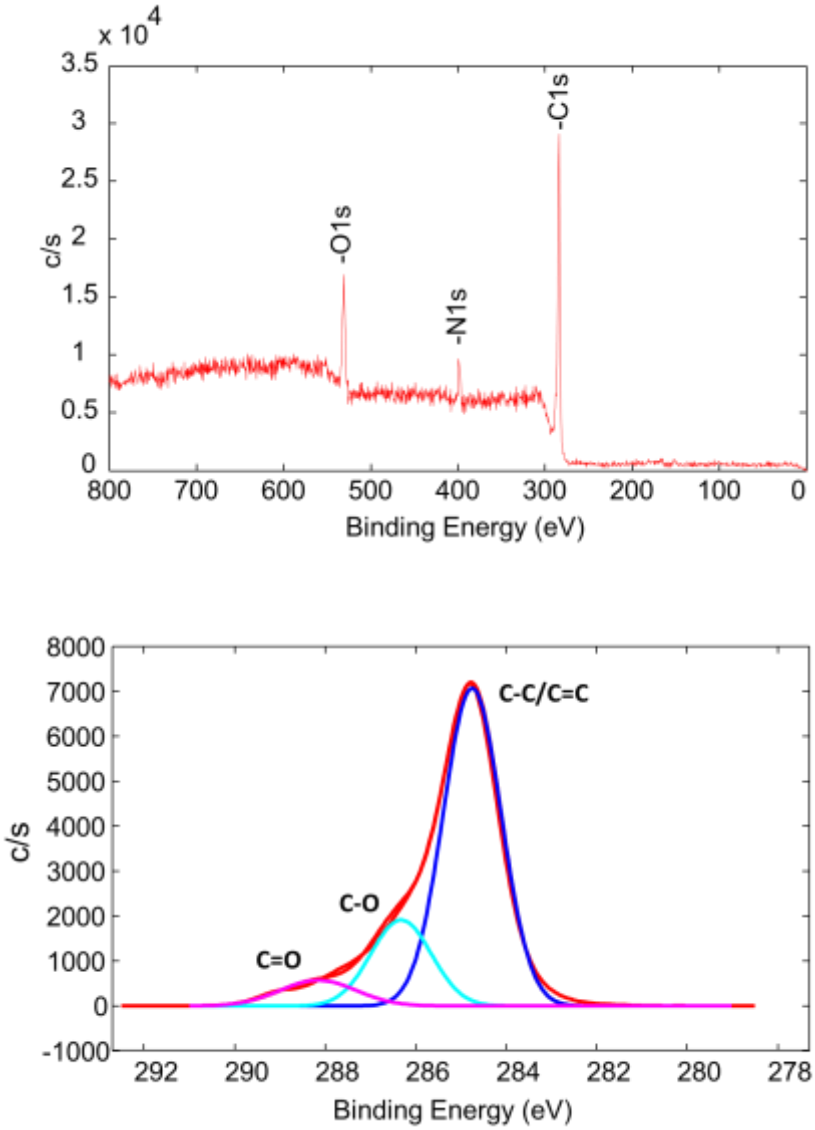

Figure 4.2 XPS survey scan (A) and fine scan of C 1s (B) of original graphene oxide membrane

To investigate the change of carbon oxidation state, XPS spectra were collected before and after chlorine reactions. Figure 4.2A showed the XPS survey scan of the original membrane with peaks for C 1s, O 1s and N 1s from the graphene oxide and the cross-linker polymer PAA. The elemental composition was determined to be carbon 76.8%, oxygen 15.2% and nitrogen 8.0%. Figure 4.2B showed the fine scan for C 1s of the original membrane and the relative ratio of

carbon in different oxidation state was 71.99% for C-C/C=C, 20.40% for C-O and 7.62% for C=O. The higher C-C/C=C percentage than the free-standing graphene oxide in aqueous (50.11%), as well as lower C-O and C=O percentage, were possibly due to the addition of PAA polymer and the reaction between $–NH_2$ and the C-O, C=O groups, according to research by Park et al.[174]

After 2 hours reaction with 100 mg/L free chlorine at pH 7 under UV light irradiation, the elemental composition changed to carbon 70.2%, oxygen 19.8% and nitrogen 10.0%, as shown in Figure 4.3A. The increased nitrogen content was possibly due to the dissociation of graphene oxide into the aqueous phase, as shown in the above section from the TOC data. Figure 4.3B shows the carbon oxidation state (C 1s spectrum) after 2 hours reaction with 100 mg/L free chlorine under light irradiation at pH 7. The C-C/C=C percentage decreases from 71.99% to 50.84%, while the C-O percentage increased from 20.40% to 41.88%. This indicates that the carbon in graphene oxide is further oxidized by free chlorine under UV light irradiation, which was consistent with the result discussed in Chapter 3. However, in Chapter 3, it was found that the C=O percentage decreased after reaction with free chlorine under light irradiation, due to the electron-deficiency of the carbon atom in C=O and vulnerable to radical attacking. However, the C=O percentage for membrane associate GO after the reaction did not show significant decrease (from 7.62% to 7.27%, as shown in Table S4.1 in Supporting Information). According to research by Hureiki et al, the –CO–NH– bond is relatively stable with the presence of free chlorine, and the result here seem consistent with their report.[175] Even though free chlorine can replace (via substitution) the hydrogen atom in N-H group, it did not affect the C-N bond and left the cross-linker relatively stable.[176, 177]

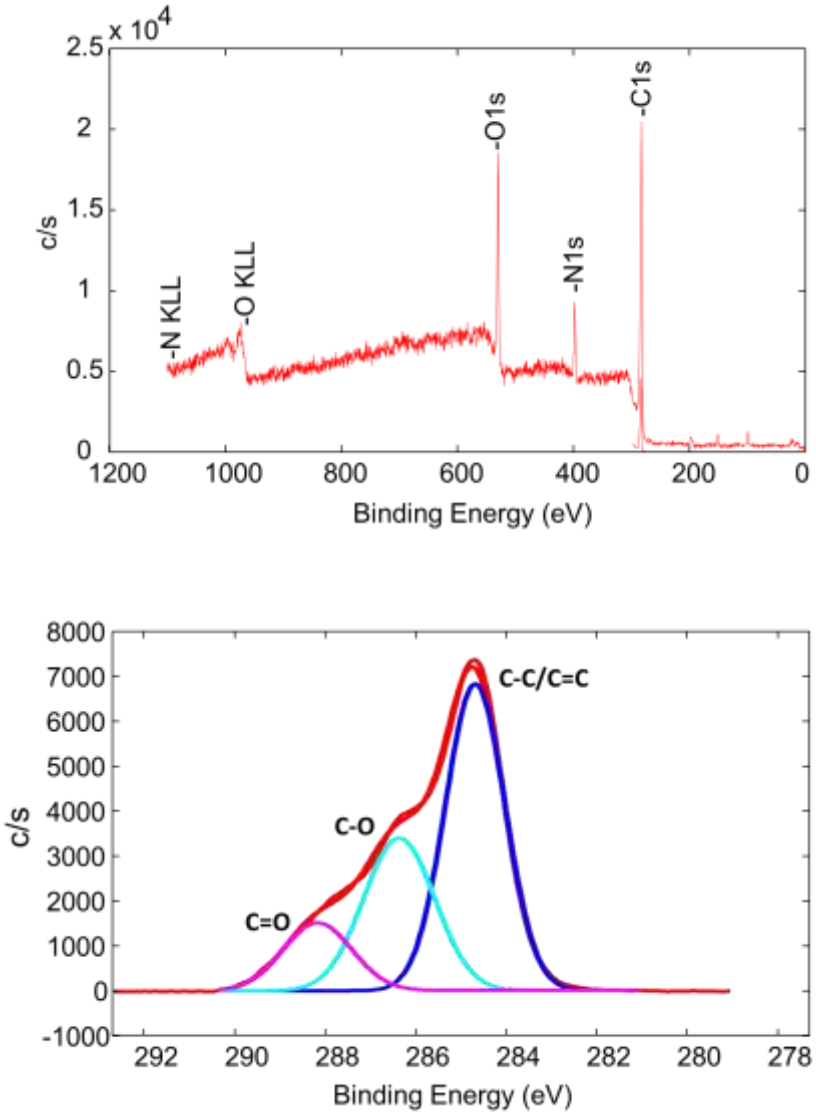

Figure 4.3 XPS survey scan (A) and C 1s scan (B) of the graphene oxide membrane after 2 hours reaction with free chlorine (100 mg/L) at pH 7 under light irradiation (2000 μW/cm^2).

The average carbon oxidation state change as a function of free chlorine concentration, in dark and under light irradiation, is shown in Figure 4.4 and the detailed data is summarized in Table S4.1 and Table S4.2. Under dark conditions, the carbon oxidation state of membrane associated graphene oxide largely remains unchanged, which was also consistent with the result in Chapter 3. Note that without the presence of free chlorine (0 mg/L), the C-C/C=C percentage

increased and C-O percentage decreased after 2 hours light irradiation, which suggested photo-reduction of graphene oxide occurred, consistent with our previous observation and by others.[148] For these, the C=O percentage still stayed relatively stable, as shown in Table S, indicating that the –CO – NH– was also resistant to the photo-transformation, as stated before. As the free chlorine concentration increased, the resulting graphene oxide oxidation state also increased, with lower C-C/C=C percentage and higher C-O percentage.

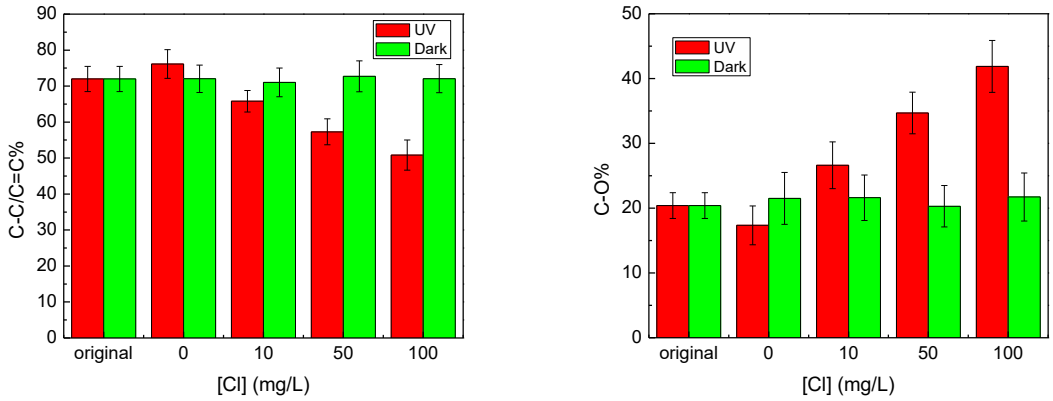

Figure 4.4 Average carbon oxidation state change (from XPS C1s scan) of the graphene oxide membrane after reaction with different concentration of free chlorine (0, 10, 50, 100 mg/L) in dark and under light irradiation (2000 μW/cm^2) for 2 hours at pH 7.

4.3.3. Effect of pH

To investigate the effect of pH on the reaction, experiments at pH 5, pH 7 and pH 9 were conducted with oxidation state change reported, represented by the C-C/C=C percentage, in Figure 4.5 and summarized in Table S4.3. As pH is increased, the resulting carbon oxidation state of graphene oxide was relatively lower, which was consistent with findings in Chapter 3 whereby higher pH leads to lower reaction rates. With 100 mg/L free chlorine, the C-C/C=C percentage decreased to 44.76% after 2 hours reaction at pH 5, while at pH 9, the C-C/C=C

percentage was 56.65% after the same reaction period. For all pH values, higher free chlorine dose concentration led to more oxidized graphene oxide.

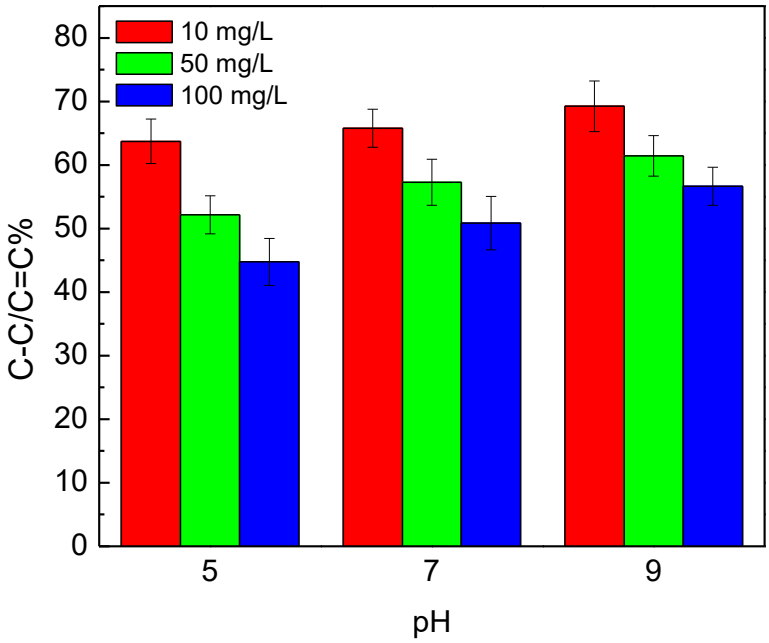

Figure 4.5 Carbon oxidation state change (from XPS C 1s scan) of graphene oxide transformation by free chlorine (10, 50 100 mg/L) under light irradiation (2000 μW/cm^2) for 2 hours under different pH conditions (5, 7, 9).

4.3.4. Reaction Time

Figure 4.6 shows the carbon oxidation state changing after reaction with free chlorine (10 mg/L and 100 mg/L) at pH 7 under light irradiation for 2 hours and 4 hours, respectively. Detailed XPS data was summarized in Table S4.4. Based on the above discussion, it was clear that graphene oxide membrane would be oxidized by free chlorine under light irradiation. However, after 4 hours reaction, the C-C/C=C percentage increased and the C-O percentage decreased, indicating that the free chlorine was completely consumed and photo-reduction of graphene oxide likely occurred.[148]

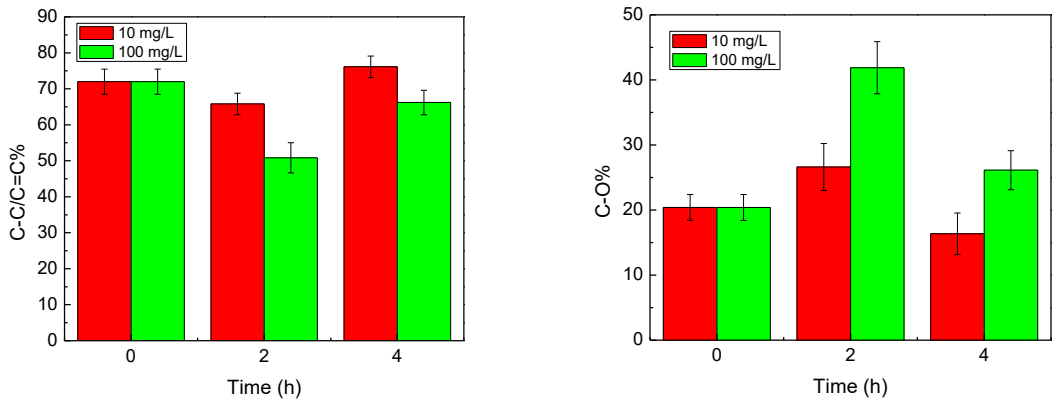

Figure 4.6 Carbon oxidation state change (from XPS C1s scan) of graphene oxide membrane after reaction with free chlorine (10 mg/L and 100 mg/L) at pH 7 under light irradiation (2000 μW/cm^2) for 2 hours and 4 hours

4.3.3 Surface Roughness

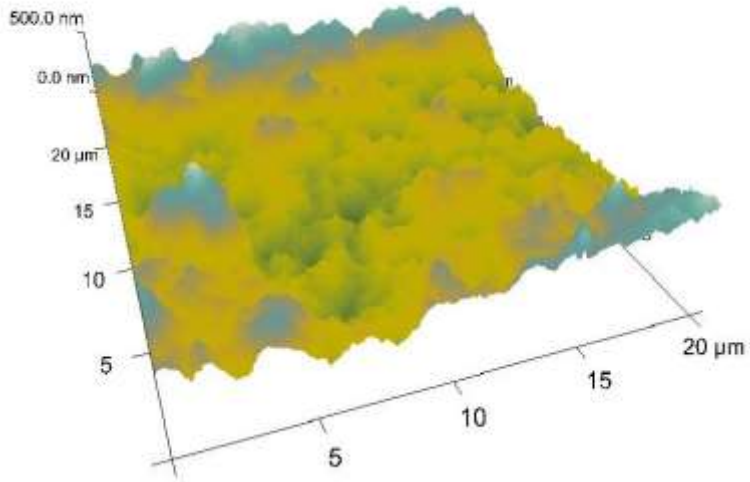

Figure 4.7 AFM image of the original graphene oxide membrane

Figure 4.7 shows an atomic force micrograph of a typical graphene oxide membrane and Figure 4.8 compares the surface roughness after reaction(s) with free chlorine (10 mg/L and 100 mg/L) under light irradiation for 2 hours and 4 hours, respectively. After 2 hours reaction, the surface roughness increased for both 10 mg/L and 100 mg/L free chlorine, from 101 nm to 104 nm with

10 mg/L and 132 nm with 100 mg/L. This is due to the oxidation and thus degradation of graphene oxide membrane.[178] After 4 hours of reaction, the surface roughness was observed to decrease, which is the result of photo-reduction after the free chlorine was depleted, which is also consistent with the XPS results.

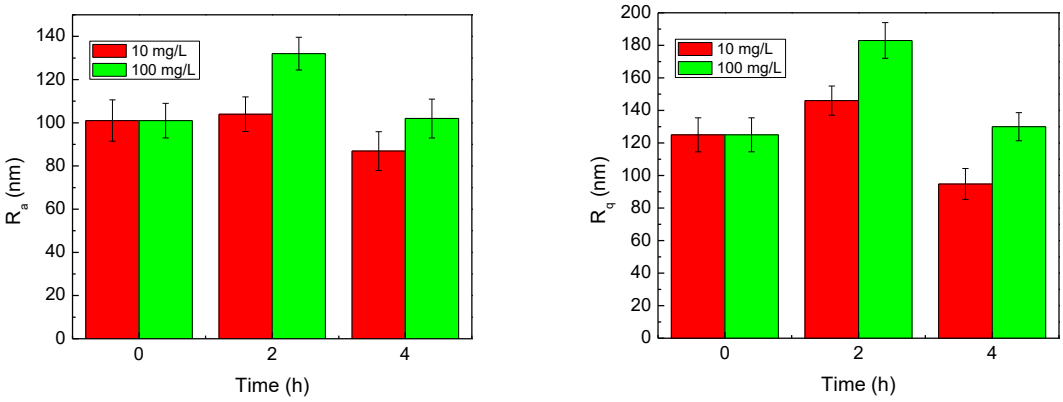

Figure 4.8 Surface roughness of graphene oxide membrane after reaction with free chlorine (10 mg/L and 100 mg/L) at pH 7 under light irradiation (2000 μW/cm^2) for 2 hours and 4 hours.

4.3.6. Water Flux

Figure 4.9 shows water flux before and after reactions with free chlorine (10 mg/L and 100 mg/L) at pH 7 under light irradiation for 2 hours and 4 hours, respectively. For both free chlorine concentrations tested, the flux increased after 2 hours of reaction, from 28.38 L/(m^2 h bar) to 30.93 L/(m^2 h bar) with 10 mg/L free chlorine and 36.22 L/(m^2 h bar) with 100 mg/L free chlorine. This was due to the oxidation of graphene oxide and the membrane became more hydrophilic, which would enhance water flux.[75, 84] However, after 4 hours reaction, the water flux decreased to 21.73 L/(m^2 h bar) with 10 mg/L free chlorine and 25.99 L/(m^2 h bar) with 100 mg/L free chlorine. This behavior is inline with XPS and AFM data, as the graphene oxide

membrane was photo-reduced after 4 hours due to the complete consumption of free chlorine and is thus less hydrophilic.

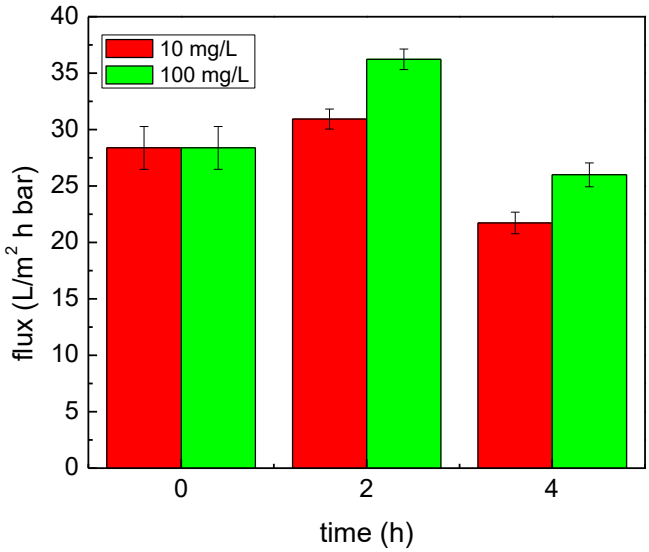

Figure 4.9 Water flux of the graphene oxide membrane before and after the reaction with free chlorine (10 mg/L and 100 mg/L) at pH 7 under light irradiation (2000 μW/cm^2) for 2 hours and 4 hours

4.4. Conclusion

The above data collectively clearly shows that graphene oxide membranes can be transformed by free chlorine under light irradiation. For a 2 hours reaction, graphene oxide membranes were oxidized and degraded, which increased surface roughness and water flux. However, after the free chlorine was depleted, the photo-reduction of graphene oxide membrane partially restored graphene (sp2) regions (i.e. loss of functional groups) which corresponds to lower water flux. While only being an initial report, this data provides an important proof of concept that GO-based membranes are likely to be susceptible to oxidation/degradation which must be incorporated into the design of related technologies.

Chapter 4: Supporting Information

Table S4.1 XPS result of graphene oxide membrane after 2 hours reaction with free chlorine at pH 7 under light irradiation (2000 μW/cm^2)

[Cl] (mg/L)	C/O	C-C/C=C	C-O	C=O
original	6.14	71.99	20.4	7.62
0	6.52	76.13	17.35	6.51
10	4.56	65.79	26.62	7.59
50	3.20	57.28	34.69	8.03
100	2.59	50.84	41.88	7.27

Table S4.2 XPS result of graphene oxide membrane after 2 hours reaction with free chlorine at pH 7 in dark condition

[Cl] (mg/L)	C/O	C-C	C-O	C=O
original	6.14	71.99	20.40	7.62
0	5.98	72.04	21.50	6.47
10	6.21	71.04	21.61	7.35
50	6.30	72.71	20.29	6.99
100	6.11	72.07	21.72	6.21

Table S4.3 XPS result of graphene oxide membrane after reaction with free chlorine (10 mg/L, 50 mg/L and 100 mg/L) under light irradiation for 2 hours under different pH conditions.

pH	[Cl] (mg/L)	C/O	C-C	C-O	C=O
	10	3.62	63.72	27.33	8.95
5	50	2.70	52.16	39.08	8.76
	100	2.01	44.76	46.26	8.98
	10	4.56	65.79	26.62	7.59
7	50	3.20	57.28	34.69	8.03
	100	2.59	50.84	41.88	7.27
	10	5.48	69.24	23.55	7.21
9	50	3.96	61.44	30.90	7.66
	100	3.22	56.65	35.67	7.68

Table S4.4 XPS result of graphene oxide membrane after reaction with free chlorine (10 mg/L and 100 mg/L) at pH 7 under light irradiation for 2 hours and 4 hours

time	[Cl] (mg/L)	C/O	C-C	C-O	C=O
0	n/a	6.14	71.99	20.4	7.62
2	10	4.56	65.79	26.62	7.59
	100	3.59	50.84	41.88	7.27
4	10	6.87	76.13	16.35	8.72
	100	5.24	66.22	26.13	8.46

Chapter 5: High Efficiency Aqueous Cerium(III) and Lanthanum(III) Adsorption on Graphene Oxide

Abstract

Herein, we systematically explore the adsorption behavior of graphene oxide (GO) towards aqueous cerium(III) and lanthanum(III), as Ce^{3+} and La^{3+}, respectively. Adsorption was modeled via a Langmuir isotherm approach with performance parameters (q_m and K_L) calculated for each condition explored. Adsorption was demonstrated to be affected by the surface chemistry of GO with higher quantity of oxygen-based functional groups correlating to higher adsorption capacities. The effect of pH and ionic strength were also explored; for all the sorption capacity decreased at lower pH and higher ionic strengths. Kinetic data shows that the equilibrium was established within 4 hours for all cases. Adsorption mechanisms are likely underpinned by ion exchange and outer sphere complexation processes. The adsorption capacities for both ions were superior to most synthesized absorbents or bio-sorbents to date, which reached maximum values of 451 mg/g for Ce and 436 mg/g for La.

5.1 Introduction

Rare earth metals are critical for many applications and have even been termed as the 'seeds of technology' or 'industrial vitamins'.[179] For example, in metallurgy, rare earth metals are added to aluminum, iron, and other host metals in order to improve the selected physical and chemical properties of the alloys. Among all the rare earth metals used in metallurgy, cerium (52%) and lanthanum (26%) are the two most commonly applied elements.[180] Cerium addition in aluminum alloy increases the castability and high temperature strength.[181] Rare earth metals are also applied

by the glass industry for absorbing UV light, altering the refractive index and coloring or decoloring, as well as other specialty glasses and optics, among which cerium accounting for 67% and lanthanum accounted for 29% of rare earth metal usage. Cerium oxide is also used for glass polishing applications and accounts for 40 – 99% in polishing powders.[182] Lanthanum oxide as additive in optical materials is used to improve the density, micro-hardness, refractive index, chemical durability (resistance to alkali), and mechanical strength.[183-185] Also negative electrode of nickel-metal-hydride (NiMH) rechargeable batteries consist of rare earth metals (lanthanum accounts for 50% and cerium contributed 33% total rare earth metals used in NiMH batteries).[180] American's best-selling hybrid car Toyota Prius requires 10 – 15 kg of lanthanum per vehicle for the NiMH batteries and this value is expected to double as the engineers further boost the fuel efficiency.[186] Cerium is also an important component of the NiMH battery.[187] Taken together, it is clear that rare earth metal are crucial to many industries, and cerium and lanthanum are amongst the most important.

While the demand for rare earth metal keeps increasing, the supply is decreasing.[188] Over the past decade, removal and recovery of the rare earth metal from aqueous solution has drawn considerable attention and different types of absorbents have been studied, such as commercial and hybrid materials, nanoparticles, nanocomposites, and bio-sorbents.[179] Sepehrian et al. studied the adsorption behavior of Ce on modified mesoporous aluminosilicate and calculated the Langmuir monolayer capacity of 0.032 mmol/g (4.48 mg/g).[189] Kecili et al. prepared ion imprinted cryogel which has the Ce(III) adsorption capacity of 36.58 mg/g.[190] Nishihama et al. used a solvent-impregnated resin for La adsorption and the capacity reached 0.345 mmol/g (48.3 mg/g).[191] Borai et al. synthesized emulsion polymer of carboxy methyl cellulose grafted with methyl acrylate, acrylic acid, and nitrilio tri-acetic acid and applied it in rare earth metal

adsorption, which achieved the capacity of 110 mg/g for La(III) and 121 mg/g for Ce(III).[192] Chen et al. synthesized nanoscale palygorskite grafted polymethacrylic acid with Ce adsorption capacity of 160.2 mg/g.[193] Cheng et al. synthesized chrysotile nanotubes for Ce adsorption and the Langmuir adsorption capacity was 1.21 mmol/g (173.6 mg/g).[194] Lahiji et al. reported chitosan modified with poly(vinyl alcohol) and 3-mercaptopropyltrimethoxysilane for Ce(III) and La(III) adsorption and achieved the capacity of 251.41 mg/g and 263.16 mg/g, respectively.[195] Khalil et al. applied zirconium titanate and polyacrylonitrile zirconium to evaluate the adsorption on Ce^{3+} and La^{3+}.[196] They also reported the application of chitosan acryloylthiourea derivative for La adsorption with a capacity of 2.1 mmol/g (294 mg/g).[197] Li et al. applied poly(acrylic acid) brushes-decorated attapulgite for the adsorption of Ce^{3+} and the capacity reached 295.4 mg/g, while the equilibrium was achieved within 20 min.[198] Besides the synthesized absorbents, bio-adsorption also drew attention for its natural availability. Sert et al. explored two bio-sorbents: leaf powder from Pinus brutia and Platanus orientalis. The adsorption capacity was reported as Ce 17.24 mg/g and La 22.94 mg/g for Pinus brutia, and Ce 32.05 mg/g and La 28.65 mg/g for Platanus orientalis.[199, 200] Further they modified the Pinus brutia leaf powder with citric acid and the capacity for Ce was increased to 62.1 mg/g.[201] Birungi and Chirwa reported adsorption of La with micro algal cells of *D. multivariabilis* and the capacity reached 100 mg/g.[202] Khosravi et al. conducted research on the bio-adsorption of Ce and La on grapefruit peel and the capacity reached 159.30 mg/g for Ce and 171.20 mg/g for La.[203] Das et al. also used bio-sorbents for La adsorption and they found the capacity to be 200.0 mg/g for fish scales and 160.2 mg/g for neem sawdust.[204] Meisam reported the adsorption of Ce and La on tangerine peel with the capacity of 162.79 mg/g for Ce and 154.86 for La.[205]

Carbon materials, such as carbon nanotubes (CNT) and graphene oxide (GO), have properties suitable for adsorption because of their abundant and favorable surface functional groups, which are tunable, and large specific surface area. Zhao et al. applied graphene oxide on aqueous Cd(II) and Co(II) adsorption and achieved the adsorption capacity of 106.3 mg/g and 68.2 mg/g, respectively.[206] Chen et al. reported Gd(III) adsorption on colloid graphene oxide and the capacity was 286.86 mg/g.[207] Amirov et al. also applied graphene oxide for aqueous Gd(III) adsorption and achieved the capacity of 1.45 mmol/g (228.01 mg/g) at pH 7.[208] Sun et al. also used graphene oxide for Eu(III) adsorption and achieved a capacity of 115.9 mg/g.[209, 210] Behdani et al. used oxidized multiwalled carbon nanotubes for Ce adsorption and achieved capacity of 92.59 mg/g.[211] Rakov and Lyu reported Ce(III) and La(III) adsorption on oxidized carbon nanotubes and achieved the sorption capacity of 950 mg/g for Ce and 840 mg/g for La.[212] However, they used particularly low sorbent concentration (6 ppm) and thus very low sorbent to sorbate ratio, leading to reduced accuracy of measurement. The authors admitted this concern in their report yet did not report the variance of their measurements. The adsorption mechanism was assigned to the functional groups on the oxidized CNT and they expected more oxidized CNT would have higher adsorption capacity, yet they did not give information about the functional group quantity of the CNT they used. In fact, most of the studies mentioned above failed to provide information on the properties of the adsorbent, especially the oxidation state (functional groups quantity) and zeta potential, which are important in optimizing adsorption process of trivalent cations. Graphene oxide application in aqueous Ce(III) and La(III) adsorption has not yet been systematically explored; however, it possesses significant potential based on the previous research. As GO can vary significantly with regard to oxidation state (oxygen density) and zeta potential, it’s important to evaluate adsorption capacities as they relate

to key GO properties, such as the quantity of functional groups and zeta potential. In this chapter, GO was synthesized with degrees of oxidation, as described in chapter 2, and applied as sorbents for Ce^{3+} and La^{3+}. The effects of GO oxidation state, contact time, solution pH, and ionic strength were systematically explored and described. Different isotherm models were compared and the maximum adsorption capacity under each condition was calculated based on the isotherm model which best fit the experimental data.

5.2 Materials and Methods

5.2.1 Material.

Graphite powder, sulfuric acid, potassium permanganate, and hydrogen peroxide solution were purchased from Sigma-Aldrich and used for graphene oxide synthesis. Cerium(III) nitrate hexahydrate and lanthanum(III) nitrate hexahydrate were also purchased from Sigma-Aldrich and dissolved in Milli-Q water to make 10 mM stock solution. All chemicals were reagent grade or higher and used without further purification, unless otherwise noted.

5.2.2 Graphene oxide synthesis.

The graphene oxide synthesis process was modified based on the widely used Hummers method.[34] Graphite powder was oxidized by $KMnO_4$ with the presence of concentrated H_2SO_4 to achieve graphitic oxide. The solid was washed and dried in vacuum, and then dissolved in water for probe sonication (2 hours). The suspension was then centrifuged at 10,000 rpm for 2 hours and the supernatant was collected as GO stock solution. We changed the temperature to control the oxidation state of GO as discussed in Chapter 2. Here, we used 3 types of GO: less oxidized GO as GO-1 which was synthesized with the reaction temperature of 10 °C and 30 °C, medium oxidized GO as GO-2 which was synthesized with the reaction temperature of 30 °C and 60 °C, and more oxidized GO as GO-3 which was synthesized with the reaction temperature of 50 °C

and 90 °C. The oxidant ratio was 3:1 w/w of $KMnO_4$/graphite and sonication time was 2 hours for all the 3 types of GO, which followed standard Hummers method. [34] The concentration of the GO stock solution was measured by filtering with the 10 nm membrane. The (dried) weight difference of the membrane before and after the filtration was taken as the weight of GO, which was divided by the filtered volume to calculate the concentration (mg/L) of the GO stock solution.

5.2.3 Graphene oxide characterization.

The carbon oxidation state is characterized by X-ray Photoelectron Spectroscopy (XPS). The sample solution was drop cast onto silica wafer and dried in vacuum chamber. Three measurements at different positions were performed for each sample and the average value was calculated. The instrument was PHI 5000 Versa Probe II. The peaks were fit using a mixed fit of 80% Gaussian and 20% Lorentzian characters in the PHI Multipak software. Peak position calibration was carried out by aligning the C 1s peak (C-C/C=C) with its reference position at 284.8 eV, and a Shirley background subtraction was performed. The zeta potential of GO nanoparticles is critical in adsorption process since GO is negatively charged and they will have electrostatic interaction with the target ions (Ce^{3+} and La^{3+}). Dynamic Light Scattering (DLS) is used to measure GO hydrodynamic radius (173° backscatter, refractive index: 1.333) [105] and zeta potential (Smoluchowski model)[55]. All samples were measured at 25 °C for 5 cycles and each cycle consists of 5 measurements. The instrument was Malvern Zetasizer Nano ZS.

5.2.4 Adsorption experiments.

GO stock solution (500 mg/L as total mass) of 1 mL was added into the 15 mL centrifuge tube containing solution with target ion (Ce^{3+} or La^{3+} from 0.7 to 168 mg/L) and NaCl (1, 10, 100, 600 mM) for controlling the ionic strength. The pH of the solution was then adjusted to the target

level (± 0.1) with HNO_3 (1%) and NaOH (100 mM). The tube was then sealed, wrapped with aluminum foil to prevent photo-reaction with light and put on the rotator for adsorption test. All adsorption tests were performed at 25 °C and allowed 24 hours to reach equilibrium. The pH level is re-adjusted to the target level after 8 hours, except for the kinetic experiment where the change in pH was recorded. After the test, the sorbent was separated using an ultra-centrifuge at 40,000 rpm for 2 hours. The supernatant was collected and the ion concentration was measured by Inductively Coupled Plasma Atomic Emission Spectroscopy (ICP-OES) with Scandium as internal standard. The instrument was Perkin Elmer Optima 7300 DV Optical Emission Spectrometer. All samples were diluted to below 100 ppm with respect to the target ions. The absorbed amount of target ion was calculated with the following equation:

$$q_e = (C_0 - C_q)\frac{V}{m}$$

where q_e is the amount of target ion absorbed on the absorbent at equilibrium with the unit of mg/g. C_0 is the initial concentration of the target ion and C_q is the aqueous concentration at equilibrium, with the unit of mg/L. V is the volume of the solution with the unit of L and m is the mass of GO in the solution with the unit g. For each condition, we also have control experiment where GO was absent, to eliminate the effect of precipitation.

5.3 Results and Discussion

5.3.1 Graphene oxide characterization before and after the adsorption.

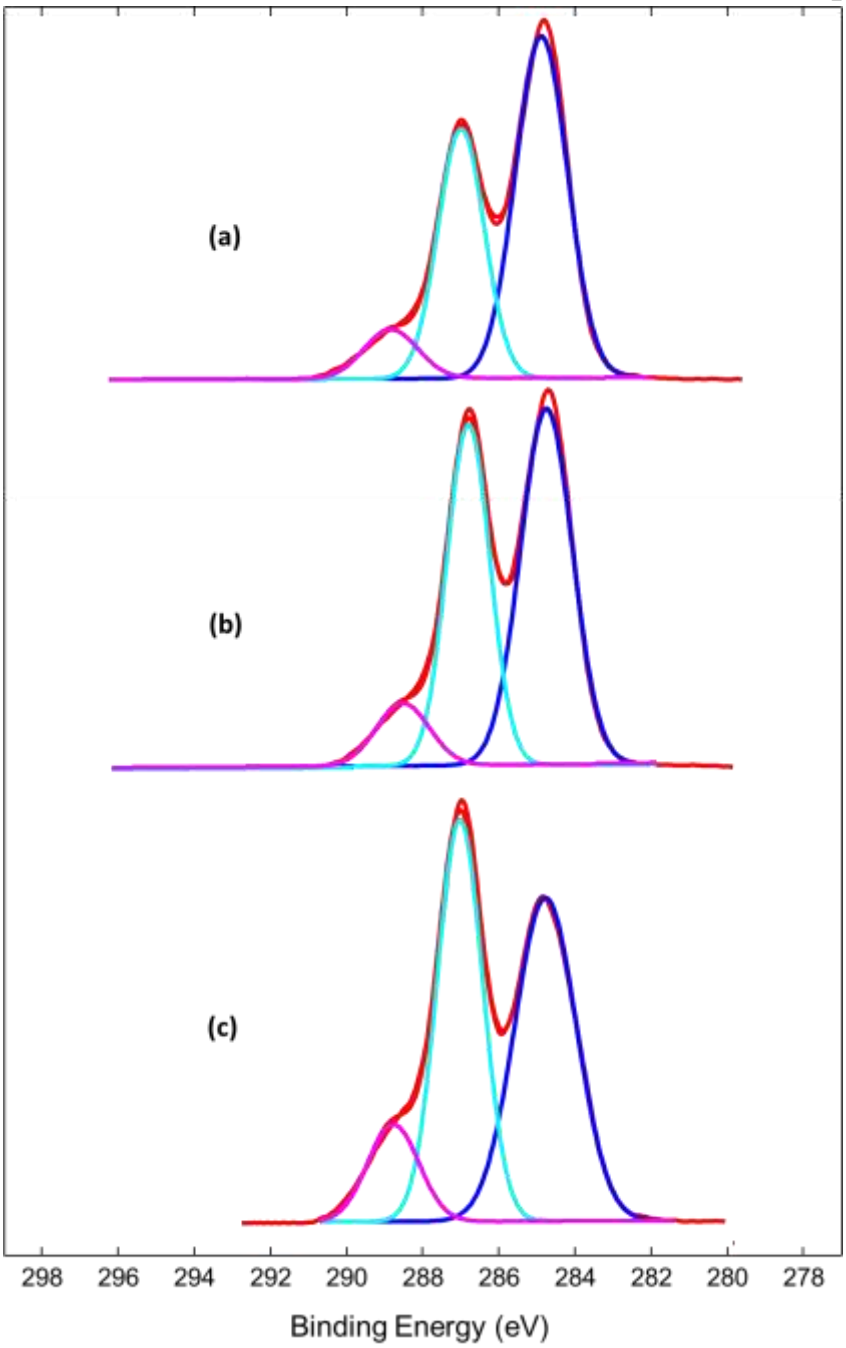

Figure 5.1. XPS (C 1s) of the 3 types of GO before adsorption. (a) low oxidized GO-1 (b) medium oxidized GO2 (c) high oxidized GO-3

Figure 5.1 shows the XPS data (C 1s spectra) describing the relative oxidation state of carbon in GO materials used. For these measurements, the 284.8 eV peak was assigned to the sp^2 hybridized carbon atoms, the 286.6 eV peak was assigned to the monooxidized carbon (e.g. C-O, C-OH), and the 288.8 eV peak was assigned to the deoxidized carbon atoms (e.g. C=O).[108] The relative quantity of the 3 peaks in the 3 types of GO is summarized in Table 5.1. Higher oxidized GO with is hypothesized to have higher adsorption capacity towards the target ions.

Table 5.1. XPS result (C 1s scan) of the GO before and after adsorption with Ce and La

		C-C/C=C	C-O	C=O
GO-1	Before	55.33 ± 1.24	36.26 ± 2.07	8.41 ± 0.91
	After	54.83 ± 1.93	37.50 ± 1.87	7.67 ± 0.24
GO-2	Before	50.11 ± 1.46	40.33 ± 0.94	9.56 ± 0.70
	After	50.41 ± 2.54	40.08 ± 1.32	9.51 ± 1.49
GO-3	Before	45.96 ± 2.14	42.33 ± 2.05	11.71 ± 0.41
	After	46.29 ± 1.26	42.93 ± 0.82	10.77 ± 1.20

After adsorption, the average oxidation state did not change much, as the XPS data also shown in Table 5.1. We conducted t-test to confirm this statement and with 99% confidence interval, it failed to reject the hypothesis that there was no difference between the oxidation state of GO before and after adsorption. This supports a non-redox based sorption mechanism(s). The hydrodynamic diameter and zeta potential data at pH 7 was summarized in Table 5.2. It showed

that the average hydrodynamic diameter decreased and zeta potential became more negative as the average oxidation state of GO decreased, i.e., had higher quantity of functional groups.

Table 5.2. Hydrodynamic diameter and zeta potential of GO at pH 7

	Hydrodynamic diameter / nm	Zeta potential / mV
GO-1	184.70 ± 8.17	-38.50 ± 0.81
GO-2	176.87 ± 7.80	-44.73 ± 0.97
GO-3	156.07 ± 6.10	-52.80 ± 1.13

5.3.2 Isotherm Modeling.

The adsorption results for the three types of GO at pH 7 was shown in Figure 5.2 for Ce and Figure 5.3 for La. The plateau at high Ce/La concentration indicated that the maximum adsorption capacity has been reached. We used both Langmuir model and Freundlich model to fit the adsorption isotherm for Ce and La. The Langmuir isotherm is fitted using the following equation:

$$q_e = \frac{q_m K_L C_q}{1 + K_L C_q}$$

$$\frac{1}{q_e} = \frac{1}{q_m K_L}\frac{1}{C_q} + \frac{1}{q_m}$$

where q_m is the maximum adsorption capacity of the absorbent and K_L is the binding constant for Langmuir model, with unit of L/mg. We plot $1/q_e$ vs $1/C_e$ and fit it with linear regression. The slope would be $1/(q_m K_L)$ while the intercept in the y axis being $1/q_m$.

The Freundlich isotherm is fitted using the following equation:

$$q_e = K_F C_q^{1/n}$$

$$lnq_e = lnK_F + \frac{1}{n} lnC_q$$

where K_F ($mg^{1-1/n}L^{1/n}g^{-1}$) and n are Freundlich constant, representing adsorption capacity and adsorption intensity, respectively.[198] We plot lnq_e vs lnC_e and fit the data with linear regression. The slop would be 1/n while the intercept in y axis being lnK_F.

The Langmuir model was plotted with solid line in Figure 5.2 for Ce and Figure 5.3 for La. The Freundlich model was plotted with dash line in Supporting Information Figure S5.1 for Ce and Figure S5.2 for La. The fitting parameters for both models and all 3 types of GO are summarized in Table 5.3 for Ce and Table 5.4 for La. It was clear that Langmuir model fits the data better than Freundlich model for both Ce and La with higher R^2 values. This is consistent with the other research.[212] So for the latter part of this chapter and discussion, we use and discuss only Langmuir model to fit the isotherms, and thus the adsorption capacity under each condition was given based on the q_m in Langmuir model.

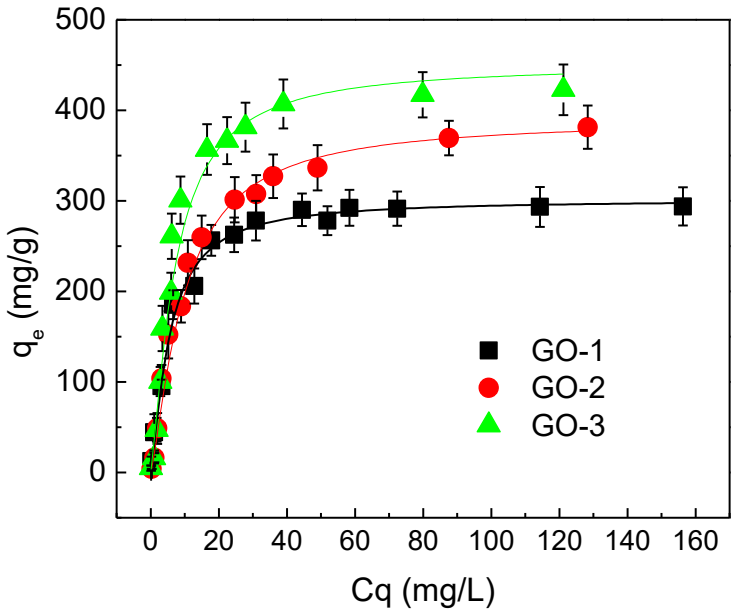

Figure 5.2 Adsorption isotherm for Ce^{3+} on three types of GO at pH 7, with isotherm fitted by Langmuir model.

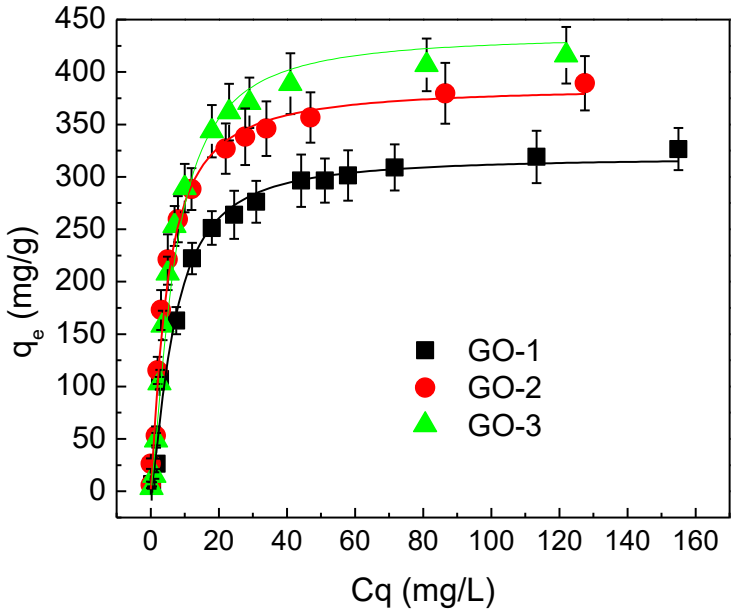

Figure 5.3 Adsorption isotherm for La^{3+} on three types of GO at pH 7, fitted with Langmuir model.

Table 5.3. Isotherm model fit result of Ce adsorption on GO at pH 7

Isotherm	Parameters	GO-1	GO-2	GO-3
Langmuir	q_m (mg/g)	301.39 ± 5.82	390.33 ± 9.56	451.07 ± 20.28
	K_L (L/mg)	0.109 ± 0.009	0.052 ± 0.002	0.078 ± 0.011
	R^2	0.9939	0.9947	0.9840
Freundlich	1/n	0.344 ± 0.45	0.800 ± 0.035	0.507 ± 0.073
	K_F ($mg^{1-1/n}L^{1/n}g^{-1}$)	68.87 ± 12.07	11.15 ± 1.19	51.05 ± 14.26
	R^2	0.8943	0.7799	0.8144

Table 5.4. Isotherm model fit result of La adsorption on GO at pH 7

Isotherm	Parameters	GO-1	GO-2	GO-3
Langmuir	q_m (mg/g)	318.89 ± 13.43	386.30 ± 22.45	435.77 ± 29.90
	K_L (L/mg)	0.067 ± 0.010	0.156 ± 0.030	0.067 ± 0.010
	R^2	0.9835	0.9705	0.9682
Freundlich	1/n	0.510 ± 0.069	0.402 ± 0.046	0.646 ± 0.085
	K_F ($mg^{1-1/n}L^{1/n}g^{-1}$)	34.62 ± 9.49	73.39 ± 12.47	27.81 ± 8.79
	R^2	0.8211	0.8845	0.6887

Based on the XPS result of the GO in Table 5.1, we obtained the information about the quantity of the functional groups (–OH and –COOH). The more oxidized GO-3 has the most oxygen functional groups and GO-1 has the least functional groups. The adsorption capacity for Ce could reach 451.07 mg/g with GO-3 at pH 7 and 435.77 mg/g for La under same condition. Note that even the less oxidize GO-1 could achieve 301.39 mg/g for Ce and 318.89 mg/g for La, which is still higher than most of the synthetic absorbents and bio-sorbents. This was because of the large surface area, low density and the large amount of functional groups in the GO structure overall.

5.3.3 Sorption Kinetics.

Adsorption kinetics provides key information about the mechanism and is key for potential applications.[213] In this work, the adsorption kinetic experiments were conducted at pH 7 for Ce^{3+} and La^{3+} with GO-3, which had the highest adsorption capacity for both cations. The adsorption capacity at each time interval q (mg/g) is shown in Figure 5.4 with solid squares and solid circles. It showed that after 4 hours the system reached equilibrium. Due to the long centrifuge time needed (2 hours) in the separation step after adsorption, we were not able to investigate the kinetics with time interval shorter than 2 hours.

Figure 5.4 also showed the pH change during the 48 hours adsorption process with empty squares and empty circles. We can see that the pH initially decreased then reached steady state after 4 hours, consistent with the time needed for equilibrium in the kinetics shown in Figure 5.5. This also suggest that during the adsorption process, H^+ was produced which could come from the ion exchange between the aqueous Ce^{3+}/La^{3+} and the carboxyl groups on GO. This is consistent with other research on adsorption with GO, whereby carboxyl groups were responsible for the adsorption of cations via ion exchange.[214, 215]

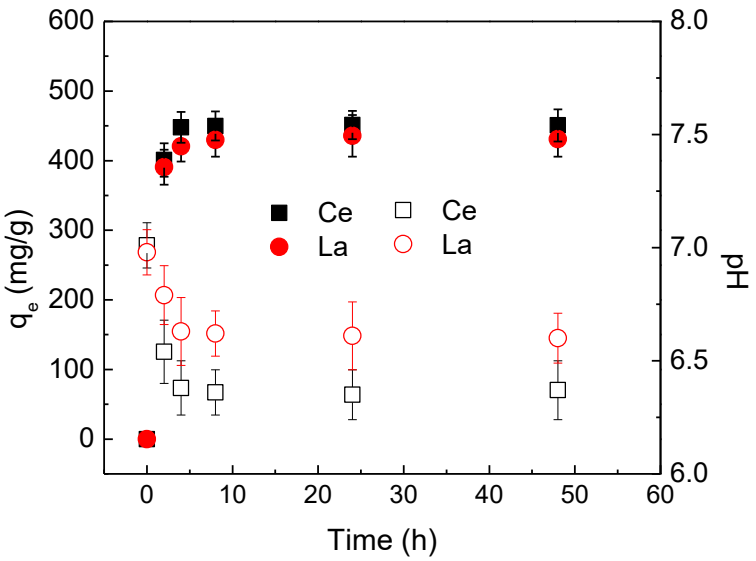

Figure 5.4 Sorption kinetics of Ce and La on GO-3 at initial pH of 7 and pH change during the 48 hours adsorption period

5.3.4 Effect of pH.

We performed adsorption experiments over a pH range 3 – 9. For pH 8 and 9, even though we did not observe precipitation in either the blank (without GO) samples nor for the samples with GO, the Ce^{3+} or La^{3+} concentration in the aqueous solution dropped to nearly 0 ppm after ultra-centrifuge for both samples. As pH increases, the trivalent ion undergoes complexation with OH^- and changes from M^{3+} to $M(OH)^{2+}$ to $M(OH)_2^+$ to $M(OH)_3$. Cerium (Ce^{3+}) starts to precipitate at pH 7.6 as $Ce(OH)_3$ [216] and lanthanum (La^{3+}) starts to precipitate at around pH 8.5 as $La(OH)_3$.[217] The general hydrolysis reactions of Ce^{3+} and La^{3+} are as follows:

$$M^{3+} + H_2O \overset{\beta_1}{\leftrightarrow} M(OH)^{2+}$$

$$M^{3+} + 2H_2O \overset{\beta_2}{\leftrightarrow} M(OH)_2^+$$

$$M^{3+} + 3H_2O \overset{\beta_3}{\leftrightarrow} M(OH)_3$$

The M^{3+} represents Ce^{3+} or La^{3+}. The individual species percentage could be calculated as followed:

$$M^{3+} = \frac{1}{1 + 10^{pH+log\beta_1} + 10^{2pH+log\beta_2} + 10^{3pH+log\beta_3}}$$

$$M(OH)^{2+} = 10^{pH+log\beta_1} M^{3+}$$

$$M(OH)_2^{+} = 10^{2pH+log\beta_2} M^{3+}$$

$$M(OH)_3 = 10^{3pH+log\beta_3} M^{3+}$$

The complexation (hydrolysis) constants for Ce and La were summarized in Table 5.5 and the species diagrams were shown in Figure 5.5, assuming all species remaining dissolved.

Table 5.5 Hydrolysis constants of Ce^{3+} and La^{3+} with OH^-.[216, 217]

	Ce^{3+}	La^{3+}
$\log\beta_1$	-8.41	-8.5
$\log\beta_2$	-17.6	-17.2
$\log\beta_3$	-27.23	-25.9

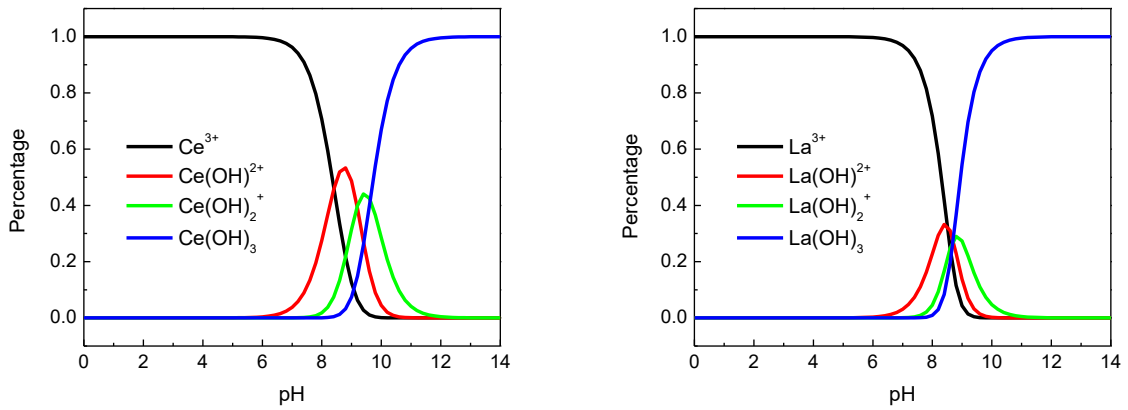

Figure 5.5 Species diagram of aqueous Ce(III) and La(III) at different pH without precipitation and redox reaction. Calculation based on the complexation of Ce^{3+} and La^{3+} with OH^- only.

Based on our observation and these calculations, we thus limited our focus on pH regions without the precipitation potential, i.e., pH 3 – 7. We used adsorption capacity to evaluate the effect of pH on the adsorption. The q_m at different pH for the 3 type of GO is shown in Figure 5.6A for Ce and Figure 5.7B for La, and the detailed isotherm of each condition (pH level, GO type) is provided in the Supporting Information. It is clear that as pH is increased, adsorption capacity also increased. Specifically, as pH level increased from 3 to 7, the adsorption capacity increased by 3.5 – 5.5 times for Ce and 3.2 – 4.3 times for La. This trend is consistent with the other reports.[189, 194, 198] The reason for this increase in adsorption capacity is due to more deprotonated –COOH groups which have stronger electrostatic interaction with the trivalent cations (compared to the acidic form). This is also consistent with the zeta potential data in Chapter 2 that as pH increased, the zeta potential of GO became more negative. Another reason could be that at lower pH, GO became less negatively charged and the nanoparticles aggregate, thus lose available surface area.[198] Even though Ce^{3+} and La^{3+} could undergo complexation with

OH^-, the dominant species were still positive charged ions below pH 7, which kept the adsorption preferable under for an electrostatic-based interaction.[216, 217]

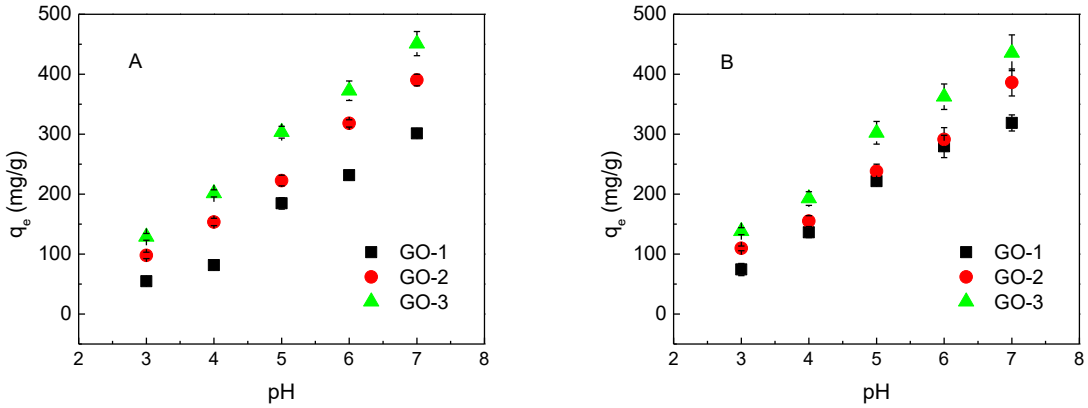

Figure 5.6 Ce^{3+} (A) and La^{3+} (B) adsorption capacity of three types of GO (as stated in the Experimental section) under different pH level (pH 3 – 7). Capacity was calculated based on the q_e in Langmuir isotherm.

5.3.5 Effect of Ionic Strength.

For target cation adsorption with GO, coexisting cations will potentially have competing effects during adsorption processes. Here we used NaCl to control the ionic strength, mimicing different environmental scenarios: 1 mM NaCl for drinking water, 10 mM NaCl for surface water, 100 mM NaCl for groundwater and 600 mM NaCl for seawater, at both pH 5 and pH 7.[218, 219] We used maximum capacity to evaluate the effect of ionic strength on the adsorption. The q_m value for each type of GO under different ionic strength level is tabulated in Table 5.6 for Ce and Table 5.7 for La, and the detailed isotherm for each condition is provided in the Supporting Information. It is clear that as ionic strength increases, the adsorption capacity decreases, since the addition of Na^+ would compete the limited adsorption sites with the target ions. This trend is also consistent with other reports.[212] Note that the decrease of the adsorption capacity was more severe at pH 7 than at pH 5. One reason could be that at higher pH, Ce^{3+} and La^{3+} formed

complex with OH^- and the negative charge was neutralized to -2, -1 and 0, thus to be more vulnerable to the Na^+ competing the adsorption sites, given that electrostatic forces play an important role in these adsorption process. This result also suggests that adsorption was due to outer sphere complexation and ion exchange, rather than more stable inner sphere complexation.[215, 220]

Table 5.6 Adsorption capacity of Ce on GO under different ionic strength

	pH 5			pH 7		
NaCl (mM)	GO-1	GO-2	GO-3	GO-1	GO-2	GO-3
0	185.01	220.55	304.01	301.39	392.42	448.82
1	172.75	210.46	286.21	297.08	396.44	438.82
10	132.44	169.64	257.12	237.15	314.59	360.49
100	76.66	131.24	172.09	152.13	195.74	234.13
600	49.81	84.85	105.60	83.80	144.06	161.47

Table 5.7 Adsorption capacity of La on GO under different ionic strength

	pH 5			pH 7		
NaCl (mM)	GO-1	GO-2	GO-3	GO-1	GO-2	GO-3
0	221.48	238.28	302.23	318.89	386.30	435.77
1	207.75	237.17	297.54	326.54	378.49	421.15
10	181.69	227.36	256.23	271.57	308.57	358.47
100	102.97	135.21	157.59	174.74	192.05	213.42
600	50.38	78.19	102.68	91.93	96.44	125.35

5.4 Conclusion

Work in this chapter collectively show that graphene oxide has high potential for rare earth element sorption and separation, with adsorption capacities for aqueous Ce(III) and La(III), being as high as 451.07 mg/g for Ce and 435.77 mg/g for La. The adsorption equilibrium followed Langmuir isotherm for all types of GO explored. The more oxidized GO, with higher quantity of functional groups, possessed higher adsorption capacity for all cases. The adsorption capacity increased as solution pH increased from 3 to 7. We proposed that adsorption mechanism is likely due to ion exchange and outer sphere complexation since the capacity decreased significantly with increasing solution ionic strength.

Chapter 5: Supporting information.

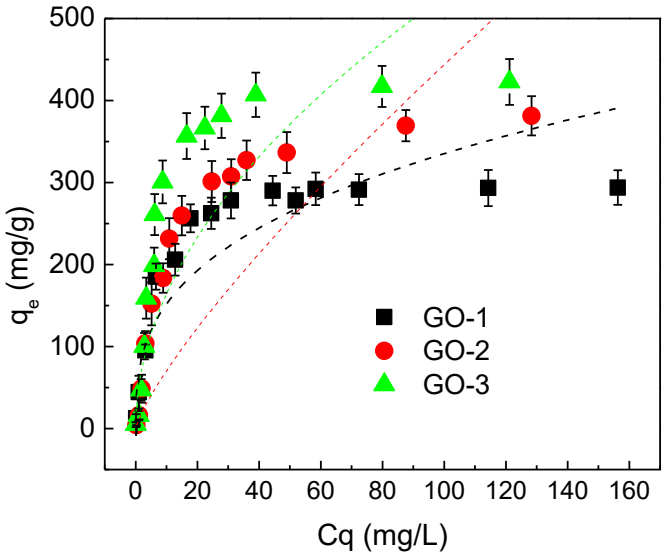

Figure S5.1. Adsorption isotherm for Ce^{3+} on 3 types of GO at pH 7, fitted with Freundlich model.

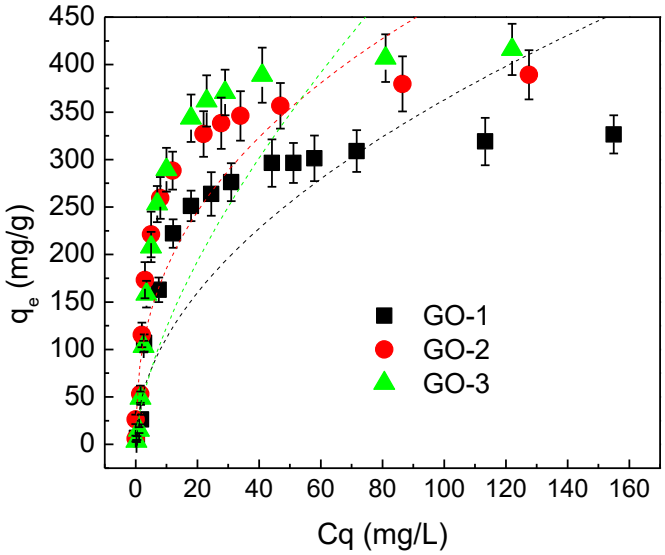

Figure S5.2. Adsorption isotherm for La^{3+} on 3 types of GO at pH 7, fitted with Freundlich model.

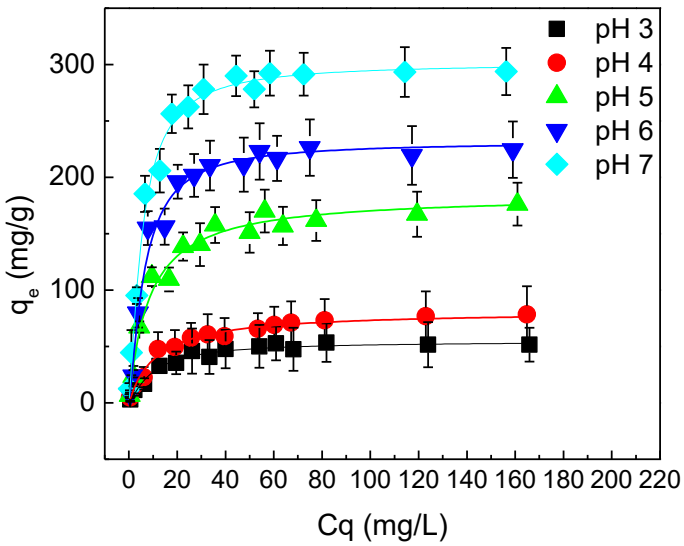

Figure S5.3 GO-1 adsorption isotherm for Ce^{3+} at different pH level (3 – 7), fitted with Langmuir isotherm.

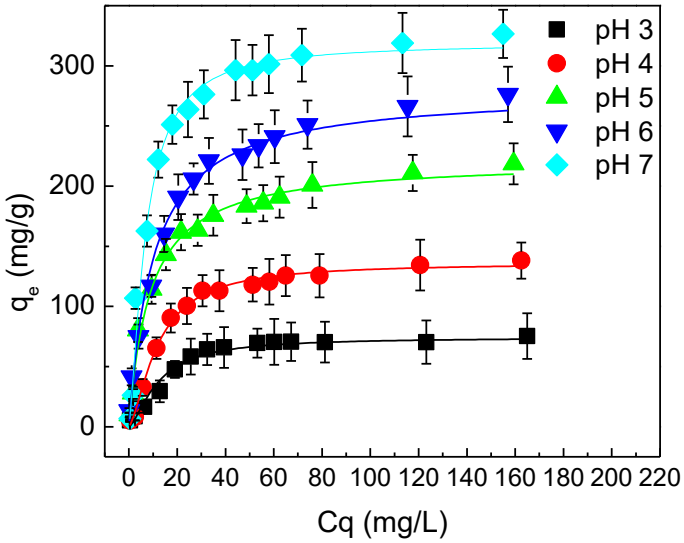

Figure S5.4 GO-1 adsorption isotherm for La^{3+} at different pH level (3 – 7), fitted with Langmuir isotherm

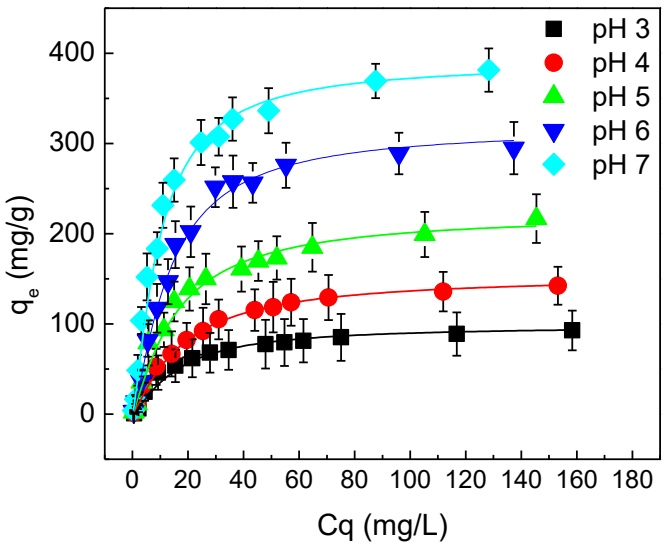

Figure S5.5 GO-2 adsorption isotherm for Ce^{3+} at different pH level (3 – 7), fitted with Langmuir isotherm

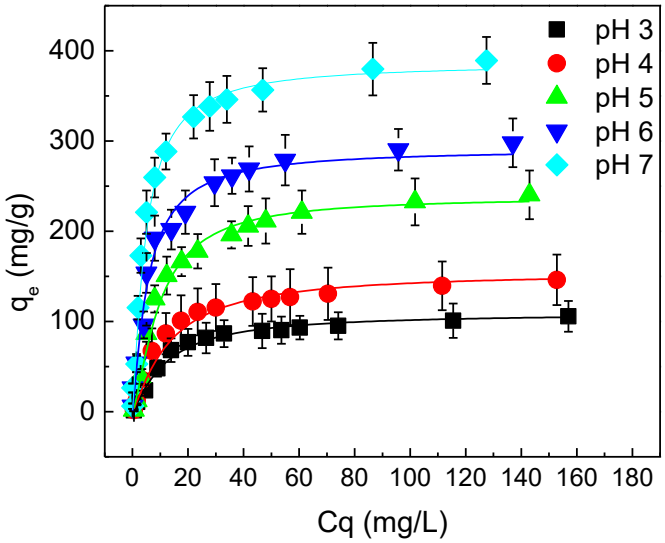

Figure S5.6 GO-2 adsorption isotherm for La^{3+} at different pH level (3 – 7), fitted with Langmuir isotherm

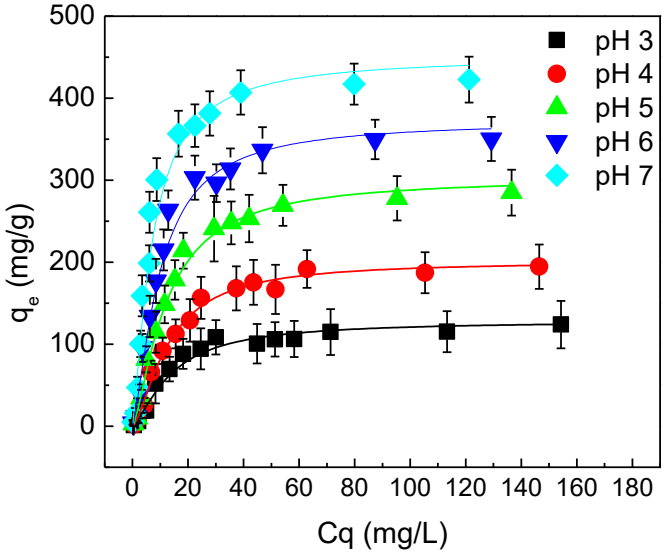

Figure S5.7 GO-3 adsorption isotherm for Ce^{3+} at different pH level (3 – 7), fitted with Langmuir isotherm

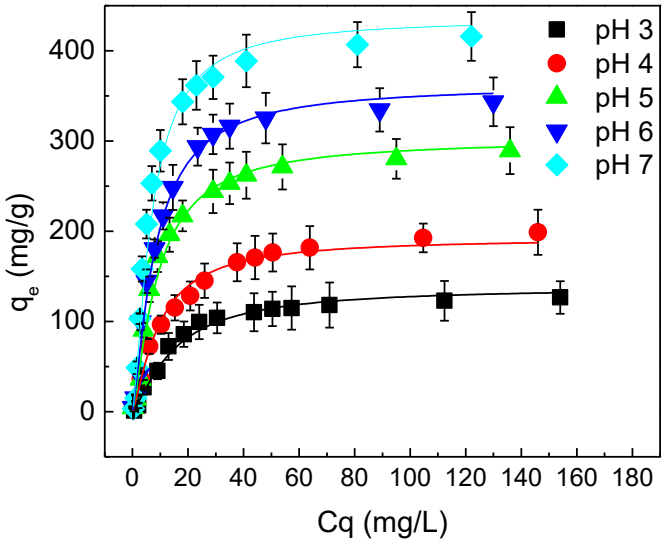

Figure S5.8 GO-3 adsorption isotherm for La^{3+} at different pH level (3 – 7), fitted with Langmuir isotherm

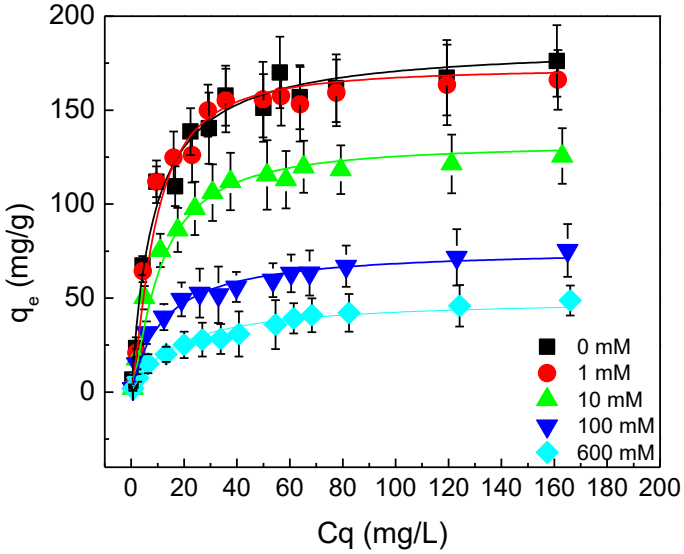

Figure S5.9 Ce^{3+} adsorption on GO-1 at pH 5 with increasing ionic strength (0, 1, 10, 100, 600 mM), fitted with Langmuir isotherm

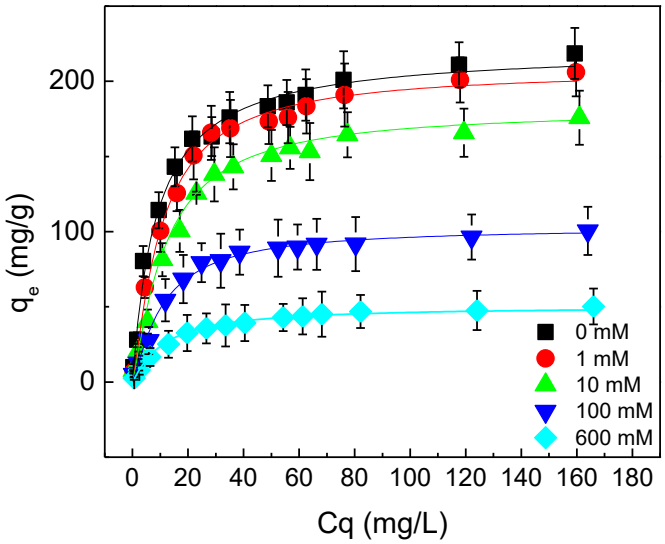

Figure S5.10. La^{3+} adsorption on GO-1 at pH 5 with increasing ionic strength (0, 1, 10, 100, 600 mM), fitted with Langmuir isotherm

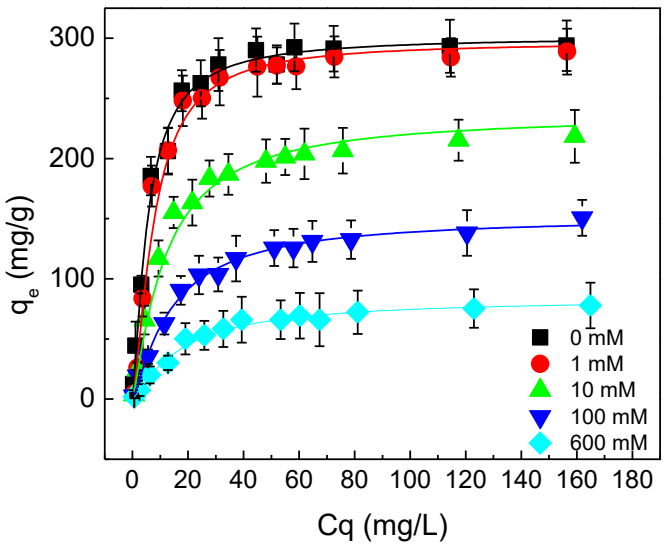

Figure S5.11 Ce^{3+} adsorption on GO-1 at pH 7 with increasing ionic strength (0, 1, 10, 100, 600 mM), fitted with Langmuir isotherm

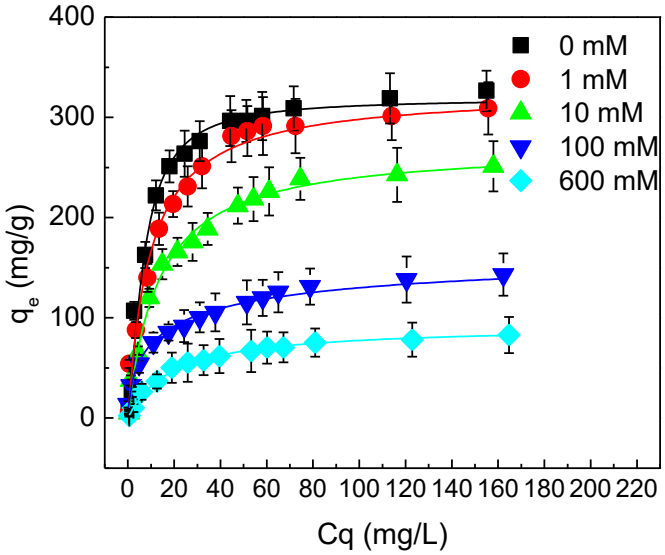

Figure S5.12 La^{3+} adsorption on GO-1 at pH 7 with increasing ionic strength (0, 1, 10, 100, 600 mM), fitted with Langmuir isotherm

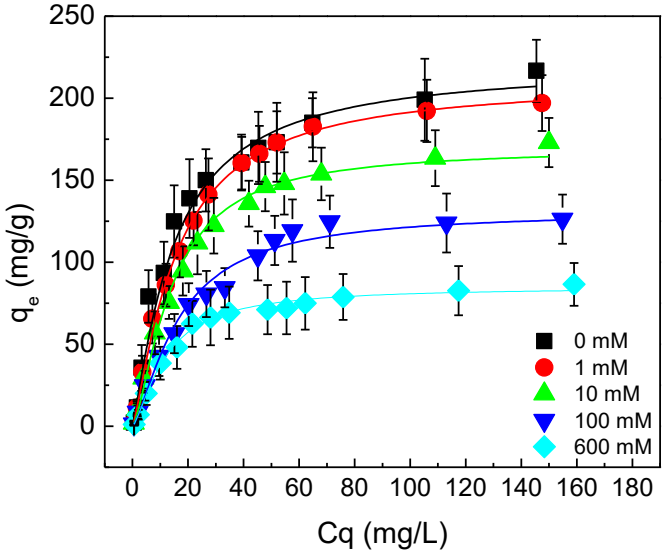

Figure S5.13 Ce^{3+} adsorption on GO-2 at pH 5 with increasing ionic strength (0, 1, 10, 100, 600 mM), fitted with Langmuir isotherm

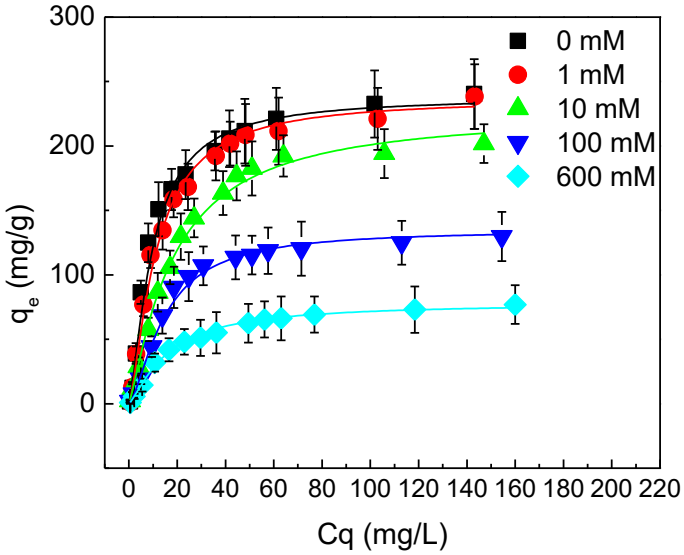

Figure S5.14 La^{3+} adsorption on GO-2 at pH 5 with increasing ionic strength (0, 1, 10, 100, 600 mM), fitted with Langmuir isotherm

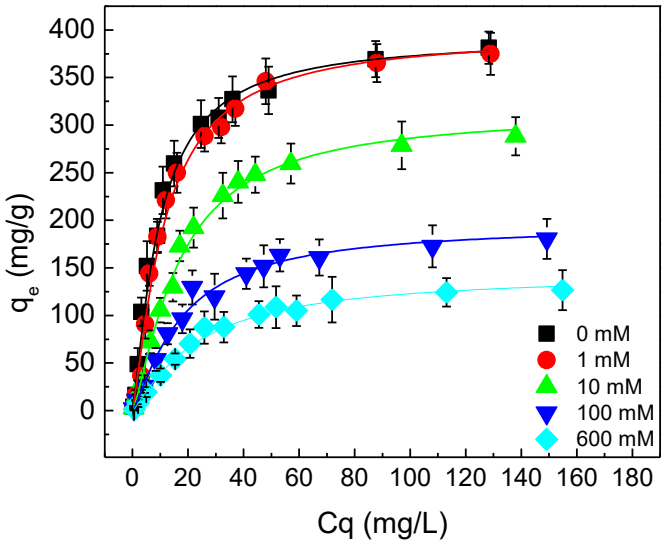

Figure S5.15 Ce^{3+} adsorption on GO-2 at pH 7 with increasing ionic strength (0, 1, 10, 100, 600 mM), fitted with Langmuir isotherm

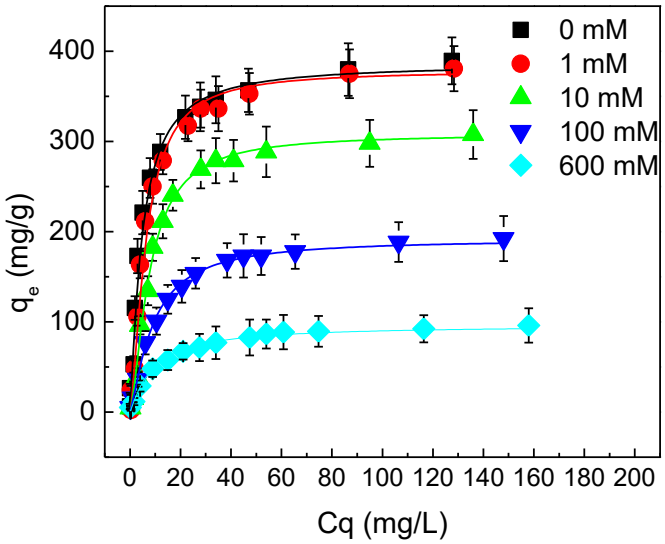

Figure S5.16 La^{3+} adsorption on GO-2 at pH 7 with increasing ionic strength (0, 1, 10, 100, 600 mM), fitted with Langmuir isotherm

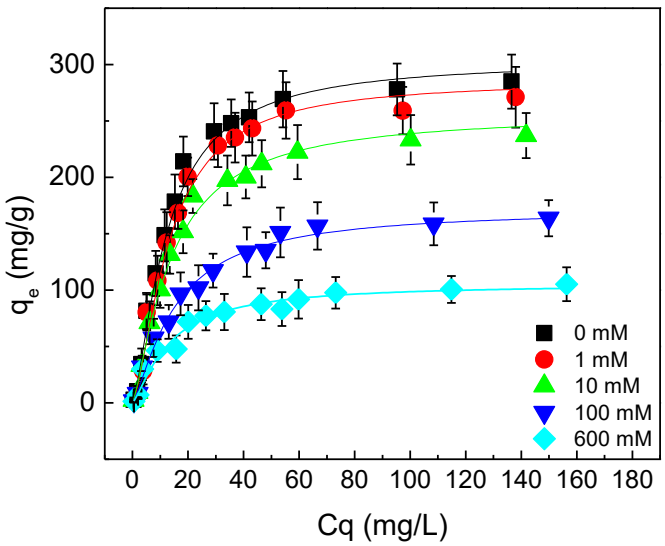

Figure S5.17 Ce^{3+} adsorption on GO-3 at pH 5 with increasing ionic strength (0, 1, 10, 100, 600 mM), fitted with Langmuir isotherm

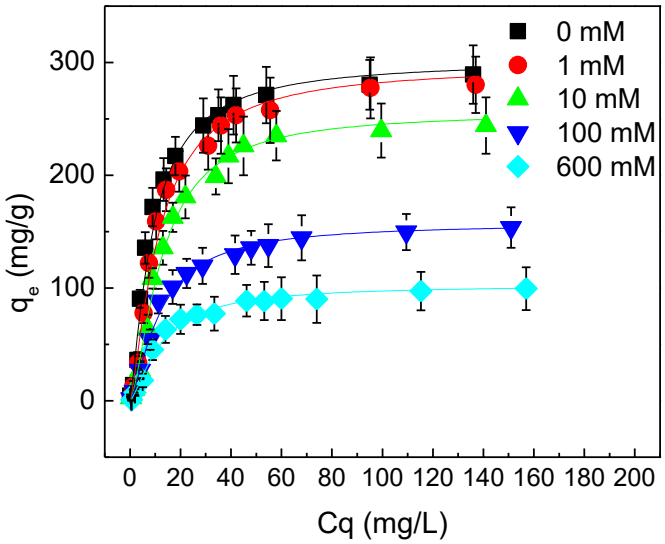

Figure S5.18 La^{3+} adsorption on GO-3 at pH 5 with increasing ionic strength (0, 1, 10, 100, 600 mM), fitted with Langmuir isotherm

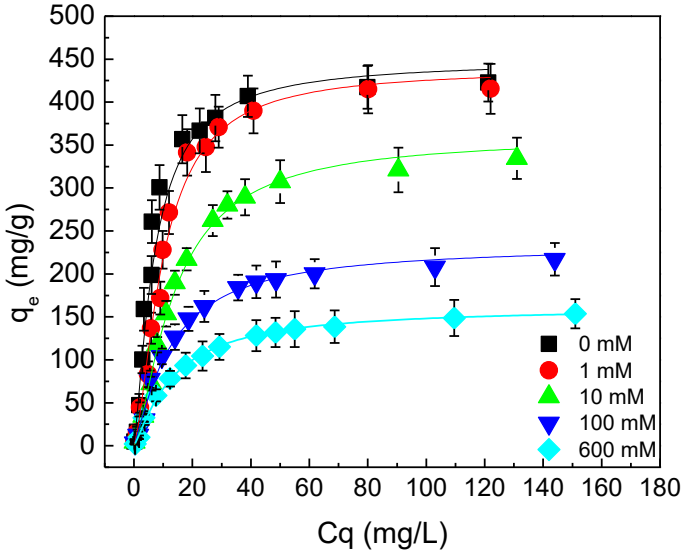

Figure S5.19 Ce^{3+} adsorption on GO-3 at pH 7 with increasing ionic strength (0, 1, 10, 100, 600 mM), fitted with Langmuir isotherm

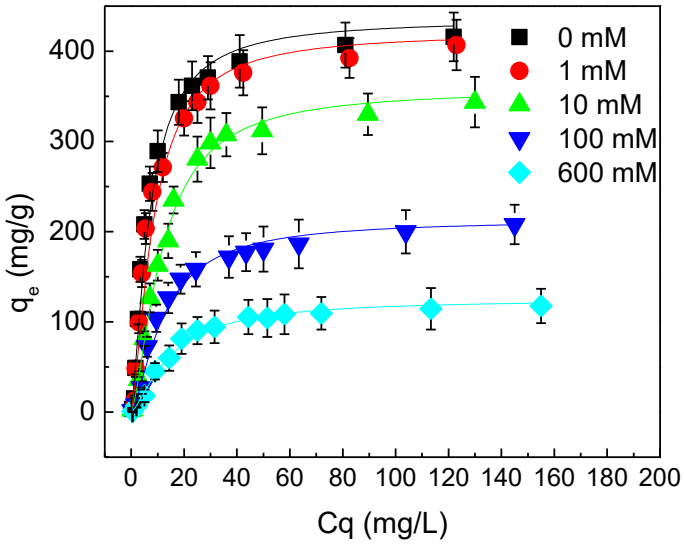

Figure S5.20 La^{3+} adsorption on GO-3 at pH 7 with increasing ionic strength (0, 1, 10, 100, 600 mM), fitted with Langmuir isotherm

Table S5.1 Langmuir model parameters for Ce^{3+} adsorption on GO

	GO-1			GO-2			GO-3		
pH	q_m	K_L	R^2	q_m	K_L	R^2	q_m	K_L	R^2
3	54.54	0.064	0.9795	97.91	0.028	0.9805	128.62	0.025	0.9875
4	81.44	0.088	0.9896	153.56	0.032	0.9903	201.30	0.022	0.9941
5	184.54	0.119	0.9826	222.64	0.037	0.9913	303.30	0.030	0.9929
6	231.64	0.090	0.9898	317.99	0.035	0.9977	372.50	0.041	0.9860
7	301.39	0.109	0.9939	390.33	0.052	0.9947	451.07	0.078	0.9840

Table S5.2 Langmuir model parameters for La^{3+} adsorption on GO

	GO-1			GO-2			GO-3		
pH	q_m	K_L	R^2	q_m	K_L	R^2	q_m	K_L	R^2
3	74.23	0.024	0.8478	109.55	0.050	0.9915	138.22	0.030	0.9895
4	136.18	0.024	0.9661	155.09	0.045	0.9775	192.69	0.053	0.9769
5	221.48	0.114	0.9940	238.28	0.042	0.9831	302.23	0.057	0.9748
6	279.62	0.099	0.9750	291.37	0.127	0.9598	362.54	0.065	0.9806
7	318.89	0.067	0.9835	386.30	0.156	0.9705	435.77	0.067	0.9682

Table S5.3 Langmuir model parameters for Ce^{3+} adsorption on GO with presence of NaCl at pH 5

	GO-1			GO-2			GO-3		
NaCl	q_m	K_L	R^2	q_m	K_L	R^2	q_m	K_L	R^2
0	185.01	0.119	0.9849	220.55	0.039	0.9915	304.01	0.029	0.9938
1	172.75	0.048	0.9782	210.46	0.032	0.9988	286.21	0.021	0.9904
10	132.44	0.044	0.9616	169.64	0.022	0.9968	257.12	0.033	0.9948
100	76.66	0.082	0.9756	131.24	0.020	0.9931	172.09	0.028	0.9954
600	49.81	0.058	0.9892	84.85	0.031	0.9982	105.60	0.035	0.9880

Table S5.4 Langmuir model parameters for Ce^{3+} adsorption on GO with presence of NaCl at pH 7

	GO-1			GO-2			GO-3		
NaCl	q_m	K_L	R^2	q_m	K_L	R^2	q_m	K_L	R^2
0	301.39	0.109	0.9939	392.42	0.059	0.9951	448.82	0.079	0.9854
1	297.08	0.052	0.9945	396.44	0.047	0.9932	438.82	0.032	0.9912
10	237.15	0.052	0.9896	314.59	0.025	0.9955	360.49	0.025	0.9918
100	152.13	0.041	0.9940	195.74	0.028	0.9961	234.13	0.047	0.9910
600	83.80	0.032	0.9939	144.06	0.023	0.9979	161.47	0.044	0.9919

Table S5.5 Langmuir model parameters for La^{3+} adsorption on GO with presence of NaCl at pH 5

	GO-1			GO-2			GO-3		
NaCl	q_m	K_L	R^2	q_m	K_L	R^2	q_m	K_L	R^2
0	221.48	0.114	0.9940	238.28	0.042	0.9831	302.23	0.057	0.9748
1	207.75	0.059	0.9848	237.17	0.033	0.9818	297.54	0.037	0.9881
10	181.69	0.052	0.9973	227.36	0.030	0.9979	256.23	0.022	0.9913
100	102.97	0.057	0.9899	135.21	0.018	0.9926	157.59	0.031	0.9953
600	50.38	0.071	0.9955	78.19	0.027	0.9979	102.68	0.029	0.9934

Table S5.6 Langmuir model parameters for La^{3+} adsorption on GO with presence of NaCl at pH 7

	GO-1			GO-2			GO-3		
NaCl	q_m	K_L	R^2	q_m	K_L	R^2	q_m	K_L	R^2
0	318.89	0.067	0.9835	386.30	0.156	0.9705	435.77	0.067	0.9682
1	326.54	0.105	0.9288	378.49	0.063	0.9741	421.15	0.046	0.9672
10	271.57	0.077	0.9847	308.57	0.047	0.9859	358.47	0.025	0.9954
100	174.74	0.183	0.9920	192.05	0.058	0.9913	213.42	0.026	0.9853
600	91.93	0.053	0.9971	96.44	0.088	0.9782	125.35	0.023	0.9949

Chapter 6: Conclusions and Recommendations

6.1 Conclusions

Taken together, this research provided fundamental understanding that directly expanded the current state of art graphene oxide material synthesis, environmental reaction pathways and applications including water treatment membranes and heavy metal adsorption. The findings framed the basic chemical-physical guidelines and corresponding properties for graphene oxide synthesis and application in advanced water treatment process, among others.

6.1.1 Graphene Oxide Synthesis and Characterization

1) The temperature of the reaction of graphite oxidation by $KMnO_4$ could lead to carbon oxidation state and yield change of the produced graphene oxide. The C-C/C=C percentage changed from 56.33% at low temperature to 45.21% at high temperature up to 50 °C in stage 1 and 90 °C in stage 2, while the yield was from 33.9% to 65.4%.

2) The increase of reaction time had less evident effect on carbon oxidation state of produced graphene oxide. However, longer reaction time improved the yield significantly, from 26.4% to 55.3% at medium temperature as the reaction time increased from 1 h in stage 1 and 0 min in stage 2, to 4 h in stage 1 and 120 min in stage 2.

3) The oxidation ratio did not change the carbon oxidation state much due to the sufficient surface oxidation of graphite, but changed the yield significantly due to the capacity of oxidizing the inner part of graphite particles, resulting the yield vary from less than 10% to 50% – 75% when the oxidant ratio changed from 1:1 to 5:1.

4) Longer sonication time achieved higher yield yet less oxidized graphene oxide, due to the exfoliation of the less oxidized inner layer of graphitic oxide.

5) More oxidized graphene oxide more negative zeta potential, slightly smaller hydrodynamic size distribution, higher critical coagulation concentration against Na^+ and Mg^{2+}, broader Raman peaks, smaller I_D/I_G ratio and lower ratio of weight left in TGA after the temperature increased to 1000 °C

6.1.2 Graphene Oxide Photo-Transformation by Free Chlorine.

1) Graphene oxide was readily transformed within 2 hours by free chlorine under light irradiation. The reaction was mainly due to radical attacking and graphene oxide was further oxidized.

2) The reaction was first order to graphene oxide and pseudo-first order to initial free chlorine. The reaction rate constant increased with lower pH, higher dissolved oxygen concentration and smaller initial graphene oxide coupon size.

3) Graphene oxide fragmentation was confirmed by TEM and product with smaller molecular weight was detected by mass spectrometry, with molecular weight of 200 Da to 1000 Da.

4) Carbon dioxide was detected as product to confirm partial mineralization of graphene oxide. The carbon balance was well established between the gas phase and the aqueous phase.

6.1.3 Chlorination Effect on Graphene Oxide Membrane under Light Irradiation

1) Graphene oxide membrane was synthesized and after reaction with 100 mg/L free chlorine under light irradiation, ~15% carbon loss was detected in the aqueous solution, while less than 10% carbon loss was detected in dark condition.

2) The graphene oxide membrane was further oxidized by free chlorine under light irradiation and lower pH led to more oxidized carbon. After the free chlorine was depleted, the photo-reduction occurred and the functional groups on the membrane surface were partially removed.

3) After oxidation by free chlorine under light irradiation, the surface roughness and water flux increased, while after photo-reduction, the surface roughness and water flux decreased, indicating a direct relationship between the functional group (hydrophilicity), surface roughness and the water flux.

6.1.4 Graphene Oxide Application on Rare Earth Metal Adsorption

1) The adsorption of cerium and lanthanum onto graphene oxide was described with Langmuir isotherm rather than Freundlich isotherm. The adsorption capacity reached 451.07 mg/g for cerium and 435.77 mg/g for lanthanum.

2) More oxidized graphene oxide had higher adsorption capacity due to more functional groups providing adsorption site. As pH increased, the adsorption capacity increased, due to more negative zeta potential of graphene oxide.

3) As ionic strength increased, the adsorption capacity decreased, suggesting that the adsorption was due to electrostatic interaction, ion exchange and outer-sphere complexation, rather than inner sphere complexation or chemical bonding.

6.2 Recommended Future Work

6.2.1 Graphene Oxide Synthesis and Characterization

1) For graphene oxide with multiple functional groups, it would be beneficial to quantify the –OH, -COOH, C-O-C group separately, among others, to better illustrate the mechanisms of reactions.

2) By tuning the synthesis parameters, design of graphene oxide nanoparticles would be achieved, with size control, desirable functional groups, mechanical properties and electronic properties, among others.

6.2.2 Graphene Oxide Environmental Fate and Transport

1) To better understand the reaction mechanisms, better product identification method should be established, to clarify the chemical structure of the product.

2) Other environmental components could be taken into consideration, such as NOM, ionic strength and light intensity.

3) The toxicity and transport properties of the product could be evaluated to better understand the environmental implication.

6.2.3 Graphene Oxide Composite Membrane Modification and Stability

1) The reaction in the presence of high concentration of salt, NOM and micro-organisms could be evaluated, to better simulate the actually operation environment.

2) The rejection of salt, organic compound (methylene blue) and proteins (BSA) before and after reaction could be investigated for better evaluation of the performance change.

3) The possible restoration by photo-reduction of graphene oxide membrane after oxidation of free chlorine could be explored to establish the pathway of membrane clean (with free chlorine) and regeneration.

4) The reaction could be investigated with membrane with graphene oxide/reduced graphene oxide/modified graphene oxide composite with other polymer/metal oxide/ionic liquid to establish the library of membranes with possible chlorine-resistance.

6.2.4 Graphene Oxide Composite for Heavy Metal Adsorption

1) Graphene oxide could be chemically modified to have other functional groups, such as $–NH_2$ or –SH, among others, or grafted with polymers/metal oxides/ionic liquids for better adsorption and separation performance, such as higher adsorption capacity, shorter equilibrium time and higher selectivity toward specific element.

2) Desorption and regeneration of the graphene oxide would be another important aspect for research, as well as the recovery of the rare earth metal for recycling and reuse.

Reference

1. A. K. Geim and K. S. Novoselov, The rise of graphene, *Nature Materials*, 2007, **6**, 183-191.
2. K. S. Novoselov, A. K. Geim, S. V. Morozov, D. Jiang, Y. Zhang, S. V. Dubonos, I. V. Grigorieva and A. A. Firsov, Electric field effect in atomically thin carbon films, *Science*, 2004, **306**, 666-669.
3. K. S. Novoselov, V. I. Fal'ko, L. Colombo, P. R. Gellert, M. G. Schwab and K. Kim, A roadmap for graphene, *Nature*, 2012, **490**, 192-200.
4. A. S. Mayorov, R. V. Gorbachev, S. V. Morozov, L. Britnell, R. Jalil, L. A. Ponomarenko, P. Blake, K. S. Novoselov, K. Watanabe, T. Taniguchi and A. K. Geim, Micrometer-Scale Ballistic Transport in Encapsulated Graphene at Room Temperature, *Nano Letters*, 2011, **11**, 2396-2399.
5. C. Lee, X. Wei, J. W. Kysar and J. Hone, Measurement of the elastic properties and intrinsic strength of monolayer graphene, *Science*, 2008, **321**, 385-388.
6. A. A. Balandin, Thermal properties of graphene and nanostructured carbon materials, *Nature Materials*, 2011, **10**, 569-581.
7. R. R. Nair, P. Blake, A. N. Grigorenko, K. S. Novoselov, T. J. Booth, T. Stauber, N. M. R. Peres and A. K. Geim, Fine structure constant defines visual transparency of graphene, *Science*, 2008, **320**, 1308-1308.
8. J. S. Bunch, S. S. Verbridge, J. S. Alden, A. M. van der Zande, J. M. Parpia, H. G. Craighead and P. L. McEuen, Impermeable atomic membranes from graphene sheets, *Nano Letters*, 2008, **8**, 2458-2462.
9. J. Moser, A. Barreiro and A. Bachtold, Current-induced cleaning of graphene, *Applied Physics Letters*, 2007, **91**.
10. Y. Wang, Z. Shi, Y. Huang, Y. Ma, C. Wang, M. Chen and Y. Chen, Supercapacitor Devices Based on Graphene Materials, *Journal of Physical Chemistry C*, 2009, **113**, 13103-13107.
11. K. Zhang, L. L. Zhang, X. S. Zhao and J. Wu, Graphene/Polyaniline Nanoriber Composites as Supercapacitor Electrodes, *Chemistry of Materials*, 2010, **22**, 1392-1401.
12. Y. Zhu, S. Murali, M. D. Stoller, K. J. Ganesh, W. Cai, P. J. Ferreira, A. Pirkle, R. M. Wallace, K. A. Cychosz, M. Thommes, D. Su, E. A. Stach and R. S. Ruoff, Carbon-Based Supercapacitors Produced by Activation of Graphene, *Science*, 2011, **332**, 1537-1541.
13. H. A. Becerril, J. Mao, Z. Liu, R. M. Stoltenberg, Z. Bao and Y. Chen, Evaluation of solution-processed reduced graphene oxide films as transparent conductors, *Acs Nano*, 2008, **2**, 463-470.
14. Y. Zhu, S. Murali, W. Cai, X. Li, J. W. Suk, J. R. Potts and R. S. Ruoff, Graphene and Graphene Oxide: Synthesis, Properties, and Applications, *Advanced Materials*, 2010, **22**, 3906-3924.
15. X. Wang, L. Zhi and K. Muellen, Transparent, conductive graphene electrodes for dye-sensitized solar cells, *Nano Letters*, 2008, **8**, 323-327.
16. J. T. Robinson, F. K. Perkins, E. S. Snow, Z. Wei and P. E. Sheehan, Reduced Graphene Oxide Molecular Sensors, *Nano Letters*, 2008, **8**, 3137-3140.

17. Y. Shao, J. Wang, H. Wu, J. Liu, I. A. Aksay and Y. Lin, Graphene Based Electrochemical Sensors and Biosensors: A Review, *Electroanalysis*, 2010, **22**, 1027-1036.
18. M. Zhou, Y. Zhai and S. Dong, Electrochemical Sensing and Biosensing Platform Based on Chemically Reduced Graphene Oxide, *Analytical Chemistry*, 2009, **81**, 5603-5613.
19. Y. Li, H. Wang, L. Xie, Y. Liang, G. Hong and H. Dai, MoS2 Nanoparticles Grown on Graphene: An Advanced Catalyst for the Hydrogen Evolution Reaction, *Journal of the American Chemical Society*, 2011, **133**, 7296-7299.
20. Y. Liang, Y. Li, H. Wang, J. Zhou, J. Wang, T. Regier and H. Dai, Co3O4 nanocrystals on graphene as a synergistic catalyst for oxygen reduction reaction, *Nature Materials*, 2011, **10**, 780-786.
21. E. Yoo, T. Okata, T. Akita, M. Kohyama, J. Nakamura and I. Honma, Enhanced Electrocatalytic Activity of Pt Subnanoclusters on Graphene Nanosheet Surface, *Nano Letters*, 2009, **9**, 2255-2259.
22. G. Eda, G. Fanchini and M. Chhowalla, Large-area ultrathin films of reduced graphene oxide as a transparent and flexible electronic material, *Nature Nanotechnology*, 2008, **3**, 270-274.
23. X. Li, X. Wang, L. Zhang, S. Lee and H. Dai, Chemically derived, ultrasmooth graphene nanoribbon semiconductors, *Science*, 2008, **319**, 1229-1232.
24. Q. Xiang, J. Yu and M. Jaroniec, Graphene-based semiconductor photocatalysts, *Chemical Society Reviews*, 2012, **41**, 782-796.
25. X. Huang, Z. Yin, S. Wu, X. Qi, Q. He, Q. Zhang, Q. Yan, F. Boey and H. Zhang, Graphene-Based Materials: Synthesis, Characterization, Properties, and Applications, *Small*, 2011, **7**, 1876-1902.
26. K. P. Loh, Q. Bao, G. Eda and M. Chhowalla, Graphene oxide as a chemically tunable platform for optical applications, *Nature Chemistry*, 2010, **2**, 1015-1024.
27. X. Huang, X. Qi, F. Boey and H. Zhang, Graphene-based composites, *Chemical Society Reviews*, 2012, **41**, 666-686.
28. A. F. Ghanem and M. H. A. Rehim, Assisted Tip Sonication Approach for Graphene Synthesis in Aqueous Dispersion, *Biomedicines*, 2018, **6**, 15.
29. G. V. Research, *Graphene Market Size And Trend Analysis By Product (Nanoplatelets, Oxide), By Application (Electronics, Composites, Energy), By Region (North America, Europe, Asia Pacific, Rest of the World), And Segment Forecasts, 2018 - 2025*, 2016.
30. AZONANO, Global demand for graphene after commercial production to be enormous, says report, http://www.azonano.com/news.aspx?newsID=29510, (accessed February 28, 2014, 2014).
31. B. Yuan, C. Bao, X. Qian, P. Wen, W. Xing, L. Song and Y. Hu, A facile approach to prepare graphene via solvothermal reduction of graphite oxide, *Materials Research Bulletin*, 2014, **55**, 48-52.
32. O. C. Compton and S. T. Nguyen, Graphene Oxide, Highly Reduced Graphene Oxide, and Graphene: Versatile Building Blocks for Carbon-Based Materials, Small Volume 6, Issue 6.*Journal*, 2010, **6**, 711-723.
33. W. Gao, L. B. Alemany, L. Ci and P. M. Ajayan, New insights into the structure and reduction of graphite oxide, *Nature Chemistry*, 2009, **1**, 403-408.
34. W. S. Hummers and R. E. Offeman, PREPARATION OF GRAPHITIC OXIDE, *Journal of the American Chemical Society*, 1958, **80**, 1339-1339.

35. S. Pei and H.-M. Cheng, The reduction of graphene oxide, *Carbon*, 2012, **50**, 3210-3228.
36. I. Grand View Research, *Graphene Market Size And Trend Analysis By Product (Nanoplatelets, Oxide), By Application (Electronics, Composites, Energy), By Region (North America, Europe, Asia Pacific, Rest of the World), And Segment Forecasts, 2014 - 2025*, Grand View Research, Inc., Grand View Research, Inc., 2016.
37. Y. X. Chen, P. C. Chuang and R. C. Wang, Cu particles induced distinct enhancements for reduced graphene oxide-based flexible supercapacitors, *Journal of Alloys and Compounds*, 2017, **701**, 603-611.
38. S. Dhibar and C. K. Das, Silver nanoparticles decorated polypyrrole/graphene nanocomposite: A potential candidate for next-generation supercapacitor electrode material, *Journal of Applied Polymer Science*, 2017, **134**.
39. X. Q. Zhang, X. X. Huang, L. Xia, B. Zhong, X. D. Zhang, T. Zhang and G. Q. Wen, Flexible freestanding cotton-graphene composites for lithium-ion batteries, *Journal of Applied Polymer Science*, 2017, **134**.
40. J. H. Li, Z. F. Xu, M. Q. Liu, P. H. Deng, S. P. Tang, J. B. Jiang, H. B. Feng, D. Qian and L. Z. He, Ag/N-doped reduced graphene oxide incorporated with molecularly imprinted polymer: An advanced electrochemical sensing platform for salbutamol determination, *Biosensors & Bioelectronics*, 2017, **90**, 210-216.
41. L. Shabnam, S. N. Faisal, A. K. Roy, E. Haque, A. I. Minett and V. G. Gomes, Doped graphene/Cu nanocomposite: A high sensitivity non-enzymatic glucose sensor for food, *Food Chemistry*, 2017, **221**, 751-759.
42. S. D. Wu, F. F. Su, X. D. Dong, C. Ma, L. Pang, D. L. Peng, M. H. Wang, L. H. He and Z. H. Zhang, Development of glucose biosensors based on plasma polymerization-assisted nanocomposites of polyaniline, tin oxide, and three-dimensional reduced graphene oxide, *Applied Surface Science*, 2017, **401**, 262-270.
43. N. Seifvand and E. Kowsari, TiO2/in-situ reduced GO/functionalized with an IL-Cr complex as a ternary photocatalyst composite for efficient carbon monoxide deterioration from air, *Applied Catalysis B-Environmental*, 2017, **206**, 184-193.
44. P. F. Wang, S. H. Zhan, Y. G. Xia, S. L. Ma, Q. X. Zhou and Y. Li, The fundamental role and mechanism of reduced graphene oxide in rGO/Pt-TiO2 nanocomposite for high-performance photocatalytic water splitting, *Applied Catalysis B-Environmental*, 2017, **207**, 335-346.
45. W. Y. Zhu, F. Q. Sun, R. Goei and Y. Zhou, Facile fabrication of RGO-WO3 composites for effective visible light photocatalytic degradation of sulfamethoxazole, *Applied Catalysis B-Environmental*, 2017, **207**, 93-102.
46. Y. F. Fan, X. Quan, H. M. Zhao, S. Chen, H. T. Yu, Y. B. Zhang and Q. Zhang, Poly(vinylidene fluoride) hollow-fiber membranes containing silver/graphene oxide dope with excellent filtration performance, *Journal of Applied Polymer Science*, 2017, **134**.
47. K. C. Ho, Y. H. Teow, W. L. Ang and A. W. Mohammad, Novel GO/OMWCNTs mixed-matrix membrane with enhanced antifouling property for palm oil mill effluent treatment, *Separation and Purification Technology*, 2017, **177**, 337-349.
48. D. Hua, R. K. Rai, Y. Zhang and T. S. Chung, Aldehyde functionalized graphene oxide frameworks as robust membrane materials for pervaporative alcohol dehydration, *Chemical Engineering Science*, 2017, **161**, 341-349.
49. D. R. Dreyer, S. Park, C. W. Bielawski and R. S. Ruoff, The chemistry of graphene oxide, *Chemical Society Reviews*, 2010, **39**, 228-240.

50. S. Gilje, S. Han, M. Wang, K. L. Wang and R. B. Kaner, A chemical route to graphene for device applications, *Nano Letters*, 2007, **7**, 3394-3398.
51. S. Stankovich, D. A. Dikin, R. D. Piner, K. A. Kohlhaas, A. Kleinhammes, Y. Jia, Y. Wu, S. T. Nguyen and R. S. Ruoff, Synthesis of graphene-based nanosheets via chemical reduction of exfoliated graphite oxide, *Carbon*, 2007, **45**, 1558-1565.
52. X. Gao, J. Jang and S. Nagase, Hydrazine and Thermal Reduction of Graphene Oxide: Reaction Mechanisms, Product Structures, and Reaction Design, *Journal of Physical Chemistry C*, 2010, **114**, 832-842.
53. Y. Zhu, M. D. Stoller, W. Cai, A. Velamakanni, R. D. Piner, D. Chen and R. S. Ruoff, Exfoliation of Graphite Oxide in Propylene Carbonate and Thermal Reduction of the Resulting Graphene Oxide Platelets, *Acs Nano*, 2010, **4**, 1227-1233.
54. D. Li, M. B. Mueller, S. Gilje, R. B. Kaner and G. G. Wallace, Processable aqueous dispersions of graphene nanosheets, *Nature Nanotechnology*, 2008, **3**, 101-105.
55. H. Q. Bao, Y. Z. Pan, Y. Ping, N. G. Sahoo, T. F. Wu, L. Li, J. Li and L. H. Gan, Chitosan-Functionalized Graphene Oxide as a Nanocarrier for Drug and Gene Delivery, *Small*, 2011, **7**, 1569-1578.
56. H. C. Schniepp, J. L. Li, M. J. McAllister, H. Sai, M. Herrera-Alonso, D. H. Adamson, R. K. Prud'homme, R. Car, D. A. Saville and I. A. Aksay, Functionalized single graphene sheets derived from splitting graphite oxide, *Journal of Physical Chemistry B*, 2006, **110**, 8535-8539.
57. E. Ziaei, A. Mehdinia and A. Jabbari, A novel hierarchical nanobiocomposite of graphene oxide-magnetic chitosan grafted with mercapto as a solid phase extraction sorbent for the determination of mercury ions in environmental water samples, *Analytica Chimica Acta*, 2014, **850**, 49-56.
58. Y. Luo, G. Zhu, X. Li, B. Yuan and Y. Feng, Facile fabrication of reduced graphene oxide-encapsulated silica: A sorbent for solid-phase extraction, *Journal of Chromatography a*, 2013, **1299**, 10-17.
59. E. Kazemi, S. Dadfarnia and A. Shabani, Dispersive solid phase microextraction with magnetic graphene oxide as the sorbent for separation and preconcentration of ultra-trace amounts of gold ions, *Talanta*, 2015, **141**, 273-278.
60. N. Hussain, P. Gogoi, V. Azhaganand, M. Shelke and M. Das, Green synthesis of stable Cu(0) nanoparticles onto reduced graphene oxide nanosheets: a reusable catalyst for the synthesis of symmetrical biaryls from arylboronic acids under base-free conditions, *Catalysis Science & Technology*, 2015, **5**, 1251-1260.
61. W. Liu, D. Sun, J. Fu, R. Yuan and Z. Li, Assembly of evenly distributed Au nanoparticles on thiolated reduced graphene oxide as an active and robust catalyst for hydrogenation of 4-nitroarenes, *Rsc Advances*, 2014, **4**, 11003-11011.
62. R. Nie, J. Wang, L. Wang, Y. Qin, P. Chen and Z. Hou, Platinum supported on reduced graphene oxide as a catalyst for hydrogenation of nitroarenes, *Carbon*, 2012, **50**, 586-596.
63. X. Xiong, H. Chen and R. Zhu, Highly efficient and scale-up synthesis of propargylamines catalyzed by graphene oxide-supported CuCl2 catalyst under microwave condition, *Catalysis Communications*, 2014, **54**, 94-99.
64. R. J. Gillespie, Teaching molecular geometry with the VSEPR model, *Journal of Chemical Education*, 2004, **81**, 298-304.

65. J. Clayden, S. G. Warren and N. Greeves, *Organic Chemistry*, OUP Oxford, Oxford, 2012.
66. A. Nixon, *Understanding Graphene - Part 1*, Technology Metals Intel, Technology Metals Intel, 2016.
67. K. I. Bolotin, K. J. Sikes, Z. Jiang, M. Klima, G. Fudenberg, J. Hone, P. Kim and H. L. Stormer, Ultrahigh electron mobility in suspended graphene, *Solid State Communications*, 2008, **146**, 351-355.
68. O. Akhavan and E. Ghaderi, Toxicity of Graphene and Graphene Oxide Nanowalls Against Bacteria, *Acs Nano*, 2010, **4**, 5731-5736.
69. M. C. Duch, G. R. S. Budinger, Y. T. Liang, S. Soberanes, D. Urich, S. E. Chiarella, L. A. Campochiaro, A. Gonzalez, N. S. Chandel, M. C. Hersam and G. M. Mutlu, Minimizing Oxidation and Stable Nanoscale Dispersion Improves the Biocompatibility of Graphene in the Lung, *Nano Letters*, 2011, **11**, 5201-5207.
70. X. G. Hu and Q. X. Zhou, Health and Ecosystem Risks of Graphene, *Chemical Reviews*, 2013, **113**, 3815-3835.
71. M. S. A. Saraswathi, R. Kausalya, N. J. Kaleekkal, D. Rana and A. Nagendran, BSA and humic acid separation from aqueous stream using polydopamine coated PVDF ultrafiltration membranes, *Journal of Environmental Chemical Engineering*, 2017, **5**, 2937-2943.
72. J. X. Ma, D. Ping and X. F. Dong, Recent Developments of Graphene Oxide-Based Membranes: A Review, *Membranes*, 2017, **7**, 29.
73. H. B. Huang, Y. L. Ying and X. S. Peng, Graphene oxide nanosheet: an emerging star material for novel separation membranes, *Journal of Materials Chemistry A*, 2014, **2**, 13772-13782.
74. D. Cohen-Tanugi and J. C. Grossman, Water Desalination across Nanoporous Graphene, *Nano Letters*, 2012, **12**, 3602-3608.
75. A. Abdel-Karim, S. Leaper, M. Alberto, A. Vijayaraghavan, X. L. Fan, S. M. Holmes, E. R. Souaya, M. I. Badawy and P. Gorgojo, High flux and fouling resistant flat sheet polyethersulfone membranes incorporated with graphene oxide for ultrafiltration applications, *Chemical Engineering Journal*, 2018, **334**, 789-799.
76. S. Liu, T. H. Zeng, M. Hofmann, E. Burcombe, J. Wei, R. Jiang, J. Kong and Y. Chen, Antibacterial Activity of Graphite, Graphite Oxide, Graphene Oxide, and Reduced Graphene Oxide: Membrane and Oxidative Stress, *Acs Nano*, 2011, **5**, 6971-6980.
77. F. M. Zou, H. J. Zhou, D. Y. Jeong, J. Kwon, S. U. Eom, T. J. Park, S. W. Hong and J. Lee, Wrinkled Surface-Mediated Antibacterial Activity of Graphene Oxide Nanosheets, *Acs Applied Materials & Interfaces*, 2017, **9**, 1343-1351.
78. C. Q. Zhao, X. C. Xu, J. Chen, G. W. Wang and F. L. Yang, Highly effective antifouling performance of PVDF/graphene oxide composite membrane in membrane bioreactor (MBR) system, *Desalination*, 2014, **340**, 59-66.
79. M. S. A. Saraswathi, D. Rana, J. S. B. Melbiah, D. Mohan and A. Nagendran, Effective removal of bovine serum albumin and humic acid contaminants using poly (amide imide) nanocomposite ultrafiltration membranes tailored with GO and MoS2 nanosheets, *Materials Chemistry and Physics*, 2018, **216**, 170-176.
80. W. Zhang, W. Cheng, E. Ziemann, A. Be'er, X. L. Lu, M. Elimelech and R. Bernstein, Functionalization of ultrafiltration membrane with polyampholyte hydrogel and graphene

oxide to achieve dual antifouling and antibacterial properties, *Journal of Membrane Science*, 2018, **565**, 293-302.
81. X. P. Wang, N. N. Li, Y. Zhao and S. J. Xia, Preparation of graphene oxide incorporated polyamide thin-film composite membranes for PPCPs removal, *Membrane Water Treatment*, 2018, **9**, 211-220.
82. L. F. Liu, X. Xie, R. S. Zambare, A. P. J. Selvaraj, B. Sowrirajalu, X. X. Song, C. Y. Y. Tang and C. J. Gao, Functionalized Graphene Oxide Modified Polyethersulfone Membranes for Low-Pressure Anionic Dye/Salt Fractionation, *Polymers*, 2018, **10**, 15.
83. J. G. Zhang, Z. W. Xu, M. J. Shan, B. M. Zhou, Y. L. Li, B. D. Li, J. R. Niu and X. M. Qian, Synergetic effects of oxidized carbon nanotubes and graphene oxide on fouling control and anti-fouling mechanism of polyvinylidene fluoride ultrafiltration membranes, *Journal of Membrane Science*, 2013, **448**, 81-92.
84. J. L. Lv, G. Q. Zhang, H. M. Zhang and F. L. Yang, Graphene oxide-cellulose nanocrystal (GO-CNC) composite functionalized PVDF membrane with improved antifouling performance in MBR: Behavior and mechanism, *Chemical Engineering Journal*, 2018, **352**, 765-773.
85. M. Mahmoudian, M. G. Kochameshki and M. Hosseinzadeh, Modification of graphene oxide by ATRP: A pH-responsive additive in membrane for separation of salts, dyes and heavy metals, *Journal of Environmental Chemical Engineering*, 2018, **6**, 3122-3134.
86. Y. Kang, M. Obaid, J. Jang, M. H. Ham and I. S. Kim, Novel sulfonated graphene oxide incorporated polysulfone nanocomposite membranes for enhanced-performance in ultrafiltration process, *Chemosphere*, 2018, **207**, 581-589.
87. Z. C. Wu, C. Zhang, K. M. Peng, Q. Y. Wang and Z. W. Wang, Hydrophilic/underwater superoleophobic graphene oxide membrane intercalated by TiO2 nanotubes for oil/water separation, *Frontiers of Environmental Science & Engineering*, 2018, **12**, 10.
88. L. Chen, N. Li, Z. Y. Wen, L. Zhang, Q. Chen, L. N. Chen, P. C. Si, J. K. Feng, Y. H. Li, J. Lou and L. J. Ci, Graphene oxide based membrane intercalated by nanoparticles for high performance nanofiltration application, *Chemical Engineering Journal*, 2018, **347**, 12-18.
89. X. Dai, X. Li, M. Zhang, J. Xie and X. L. Wang, Zeolitic Imidazole Framework/Graphene Oxide Hybrid Functionalized Poly(lactic acid) Electrospun Membranes: A Promising Environmentally Friendly Water Treatment Material, *Acs Omega*, 2018, **3**, 6860-6866.
90. Y. Jiang, W. N. Wang, D. Liu, Y. Nie, W. L. Li, J. W. Wu, F. Z. Zhang, P. Biswas and J. D. Fortner, Engineered Crumpled Graphene Oxide Nanocomposite Membrane Assemblies for Advanced Water Treatment Processes, *Environmental Science & Technology*, 2015, **49**, 6846-6854.
91. G. Charalampides, K. I. Vatalis, B. Apostoplos and B. Ploutarch-Nikolas, Rare Earth Elements: Industrial Applications and Economic Dependency of Europe, *Procedia Economics and Finance*, 2015, **24**, 126-135.
92. N. N. Greenwood and A. Earnshaw, *Chemistry of the Elements (2nd ed.)*, Butterworth-Heinemann, 1997.
93. C. Hurst, *China's Rare Earth Elements Industry: What Can the West Learn?*, 2010.
94. A. V. Naumov, Review of the world market of rare-earth metals, *Russian Journal of Non-Ferrous Metals*, 2008, **49**, 14-22.

95. M. Dejhosseini, T. Aida, M. Watanabe, S. Takami, D. Hojo, N. Aoki, T. Arita, A. Kishita and T. Adschiri, Catalytic Cracking Reaction of Heavy Oil in the Presence of Cerium Oxide Nanoparticles in Supercritical Water, *Energy & Fuels*, 2013, **27**, 4624-4631.
96. S. S. Ye, Y. Jing, Y. D. Wang and W. Y. Fei, Recovery of rare earths from spent FCC catalysts by solvent extraction using saponified 2-ethylhexyl phosphoric acid-2-ethylhexyl ester (EHEHPA), *Journal of Rare Earths*, 2017, **35**, 716-722.
97. D. I. Bleiwas, *Potential for Recovery of Cerium Contained in Automotive Catalytic Converters*, 2013.
98. K. Krishnamoorthy, M. Veerapandian, G. S. Kim and S. J. Kim, A One Step Hydrothermal Approach for the Improved Synthesis of Graphene Nanosheets, *Current Nanoscience*, 2012, **8**, 934-938.
99. Y. Q. Zhan, X. L. Yang, F. B. Meng, J. J. Wei, R. Zhao and X. B. Liu, Controllable synthesis, magnetism and solubility enhancement of graphene nanosheets/magnetite hybrid material by covalent bonding, *Journal of Colloid and Interface Science*, 2011, **363**, 98-104.
100. S. Mao, Z. H. Wen, H. Kim, G. H. Lu, P. Hurley and J. H. Chen, A General Approach to One-Pot Fabrication of Crumpled Graphene-Based Nanohybrids for Energy Applications, *Acs Nano*, 2012, **6**, 7505-7513.
101. D. Yang, A. Velamakanni, G. Bozoklu, S. Park, M. Stoller, R. D. Piner, S. Stankovich, I. Jung, D. A. Field, C. A. Ventrice and R. S. Ruoff, Chemical analysis of graphene oxide films after heat and chemical treatments by X-ray photoelectron and Micro-Raman spectroscopy, *Carbon*, 2009, **47**, 145-152.
102. Z. G. Geng, Y. Lin, X. X. Yu, Q. H. Shen, L. Ma, Z. Y. Li, N. Pan and X. P. Wang, Highly efficient dye adsorption and removal: a functional hybrid of reduced graphene oxide-Fe3O4 nanoparticles as an easily regenerative adsorbent, *Journal of Materials Chemistry*, 2012, **22**, 3527-3535.
103. W. Choi, J. Choi, J. Bang and J. H. Lee, Layer-by-Layer Assembly of Graphene Oxide Nanosheets on Polyamide Membranes for Durable Reverse-Osmosis Applications, *Acs Applied Materials & Interfaces*, 2013, **5**, 12510-12519.
104. S. Park, J. An, J. R. Potts, A. Velamakanni, S. Murali and R. S. Ruoff, Hydrazine-reduction of graphite- and graphene oxide, *Carbon*, 2011, **49**, 3019-3023.
105. Graphehe oxide product properties, http://www.sigmaaldrich.com/catalog/product/aldrich/763705?lang=en&region=US).
106. I. Chowdhury, M. C. Duch, N. D. Mansukhani, M. C. Hersam and D. Bouchard, Colloidal Properties and Stability of Graphene Oxide Nanomaterials in the Aquatic Environment, *Environmental Science & Technology*, 2013, **47**, 6288-6296.
107. K. L. Chen and M. Elimelech, Aggregation and Deposition Kinetics of Fullerene (C60) Nanoparticles, *Langmuir*, 2006, **22**, 10994-11001.
108. L. Tang, Y. Wang, Y. Li, H. Feng, J. Lu and J. Li, Preparation, Structure, and Electrochemical Properties of Reduced Graphene Sheet Films, *Advanced Functional Materials*, 2009, **19**, 2782-2789.
109. G. Q. Qi, J. Cao, R. Y. Bao, Z. Y. Liu, W. Yang, B. H. Xie and M. B. Yang, Tuning the structure of graphene oxide and the properties of poly(vinyl alcohol)/graphene oxide nanocomposites by ultrasonication, *Journal of Materials Chemistry A*, 2013, **1**, 3163-3170.

110. S. Y. Pan and I. A. Aksay, Factors Controlling the Size of Graphene Oxide Sheets Produced via the Graphite Oxide Route, *Acs Nano*, 2011, **5**, 4073-4083.
111. S. I. Ahn, Changing the sp(2) Carbon Clusters in Graphene Oxide During Exfoliation, *Transactions on Electrical and Electronic Materials*, 2015, **16**, 49-52.
112. A. Liscio, K. Kouroupis-Agalou, X. D. Betriu, A. Kovtun, E. Treossi, N. M. Pugno, G. De Luca, L. Giorgini and V. Palermo, Evolution of the size and shape of 2D nanosheets during ultrasonic fragmentation, *2d Materials*, 2017, **4**.
113. X. D. Qi, T. N. Zhou, S. Deng, G. Y. Zong, X. L. Yao and Q. Fu, Size-specified graphene oxide sheets: ultrasonication assisted preparation and characterization, *Journal of Materials Science*, 2014, **49**, 1785-1793.
114. C. Botas, A. M. Perez-Mas, P. Alvarez, R. Santamaria, M. Granda, C. Blanco and R. Menendez, Optimization of the size and yield of graphene oxide sheets in the exfoliation step, *Carbon*, 2013, **63**, 576-578.
115. M. A. Velasco-Soto, S. A. Pérez-García, J. Alvarez-Quintana, Y. Cao, L. Nyborg and L. Licea-Jiménez, Selective band gap manipulation of graphene oxide by its reduction with mild reagents, *Carbon*, 2015, **93**, 967-973.
116. Q. Lai, S. Zhu, X. Luo, M. Zou and S. Huang, Ultraviolet-visible spectroscopy of graphene oxides, *Aip Advances*, 2012, **2**.
117. K. Madhusudan Reddy, S. V. Manorama and A. Ramachandra Reddy, Bandgap studies on anatase titanium dioxide nanoparticles, *Materials Chemistry and Physics*, 2003, **78**, 239-245.
118. A. S. Hassanien and A. A. Akl, Effect of Se addition on optical and electrical properties of chalcogenide CdSSe thin films, *Superlattices and Microstructures*, 2016, **89**, 153-169.
119. A. Mathkar, D. Tozier, P. Cox, P. J. Ong, C. Galande, K. Balakrishnan, A. L. M. Reddy and P. M. Ajayan, Controlled, Stepwise Reduction and Band Gap Manipulation of Graphene Oxide, *Journal of Physical Chemistry Letters*, 2012, **3**, 986-991.
120. V. Stengl, D. Popelkova and P. Vlacil, TiO2-Graphene Nanocomposite as High Performace Photocatalysts, *Journal of Physical Chemistry C*, 2011, **115**, 25209-25218.
121. F. Tuinstra and J. L. Koenig, Raman Spectrum of Graphite, *Journal of Chemical Physics*, 1970, **53**, 1126-&.
122. A. C. Ferrari and J. Robertson, Interpretation of Raman spectra of disordered and amorphous carbon, *Physical review B*, 2000, **61**, 14095.
123. A. C. Ferrari and J. Robertson, Resonant Raman spectroscopy of disordered, amorphous, and diamondlike carbon, *Phys. Rev. B*, 2001, **64**, 075414.
124. C. Thomsen and S. Reich, Double resonant Raman scattering in graphite, *Phys. Rev. Lett.*, 2000, **85**, 5214.
125. L. G. Cançado, A. Jorio, E. H. M. Ferreira, F. Stavale, C. A. Achete, R. B. Capaz, M. V. O. Moutinho, A. Lombardo, T. S. Kulmala and A. C. Ferrari, Quantifying Defects in Graphene via Raman Spectroscopy at Different Excitation Energies, *Nano Letters*, 2011, **11**, 3190-3196.
126. L. G. Cançado, M. A. Pimenta, B. R. A. Neves, M. S. S. Dantas and A. Jorio, Influence of the atomic structure on the Raman spectra of graphite edges, *Phys. Rev. Lett.*, 2004, **93**, 247401.
127. C. Casiraghi, A. Hartschuh, H. Qian, S. Piscanec, C. Georgi, A. Fasoli, K. S. Novoselov, D. M. Basko and A. C. Ferrari, Raman Spectroscopy of Graphene Edges, *Nano Lett.*, 2009, **9**, 1433.

128. A. Oyefusi, O. Olanipekun, G. M. Neelgund, D. Peterson, J. M. Stone, E. Williams, L. Carson, G. Regisford and a. A. Oki, Hydroxyapatite grafted carbon nanotubes and graphene nanosheets: promising bone implant materials, *Spectrochimica acta. Part A, Molecular and biomolecular spectroscopy*, 2014, **132**, 410-416.
129. M. T. Eliason, E. O. Sunden, A. H. Cannon, S. Graham, A. J. García and W. P. King, Polymer cell culture substrates with micropatterned carbon nanotubes, *Journal of Biomedical Materials Research Part A*, 2007, **86A**, 996-1001.
130. M. C. Hsiao, S. H. Liao, M. Y. Yen, P. I. Liu, N. W. Pu, C. A. Wang and C. C. M. Ma, Preparation of Covalently Functionalized Graphene Using Residual Oxygen-Containing Functional Groups, *Acs Applied Materials & Interfaces*, 2010, **2**, 3092-3099.
131. G. M. Neelgund, A. Oki and Z. P. Luo, In situ deposition of hydroxyapatite on graphene nanosheets, *Materials Research Bulletin*, 2013, **48**, 175-179.
132. J. Shen, X. Li, W. Huang, N. Li and M. Ye, Synthesis of novel photocatalytic RGO-InVO4 nanocomposites with visible light photoactivity, *Materials Research Bulletin*, 2013, **48**, 3112-3116.
133. L. Shao, X. Chang, Y. Zhang, Y. Huang, Y. Yao and Z. Guo, Graphene oxide cross-linked chitosan nanocomposite membrane, *Applied Surface Science*, 2013, **280**, 989-992.
134. S. Azizighannad and S. Mitra, Stepwise Reduction of Graphene Oxide (GO) and Its Effects on Chemical and Colloidal Properties, *Scientific Reports*, 2018, **8**, 8.
135. M. Shu, X. Gao, G. W. Li, W. H. Zhu, H. T. Hao and B. Y. Shi, Effect of speciation transformation of manganese on aggregation and deposition of graphene oxide, *New Journal of Chemistry*, 2018, **42**, 2545-2552.
136. B. B. Sun, Y. Q. Zhang, W. Chen, K. K. Wang and L. Y. Zhu, Concentration Dependent Effects of Bovine Serum Albumin on Graphene Oxide Colloidal Stability in Aquatic Environment, *Environmental Science & Technology*, 2018, **52**, 7212-7219.
137. M. Wang, B. Gao, D. S. Tang, H. M. Sun, X. Q. Yin and C. R. Yu, Effects of temperature on aggregation kinetics of graphene oxide in aqueous solutions, *Colloids and Surfaces a-Physicochemical and Engineering Aspects*, 2018, **538**, 63-72.
138. Y. Jiang, R. Raliya, P. Liao, P. Biswas and J. D. Fortner, Graphene oxides in water: assessing stability as a function of material and natural organic matter properties, *Environmental Science-Nano*, 2017, **4**, 1484-1493.
139. M. J. Watts and K. G. Linden, Chlorine photolysis and subsequent OH radical production during UV treatment of chlorinated water, *Water Research*, 2007, **41**, 2871-2878.
140. E. Neyens and J. Baeyens, A review of classic Fenton's peroxidation as an advanced oxidation technique, *Journal of Hazardous Materials*, 2003, **98**, 33-50.
141. M. W. Lechevallier, C. D. Cawthon and R. G. Lee, Inactivation of Biofilm Bacteria, *Applied and Environmental Microbiology*, 1988, **54**, 2492-2499.
142. T. Hallaj, M. Amjadi, J. L. Manzoori and R. Shokri, Chemiluminescence reaction of glucose-derived graphene quantum dots with hypochlorite, and its application to the determination of free chlorine, *Microchimica Acta*, 2015, **182**, 789-796.
143. C. Wang, C. Shang, M. Ni, J. Dai and F. Jiang, (Photo)chlorination-Induced Physicochemical Transformation of Aqueous Fullerene nC(60), *Environmental Science & Technology*, 2012, **46**, 9398-9405.
144. K. N. Kim, V. P. Pham and G. Y. Yeom, Chlorine Radical Doping of a Few Layer Graphene with Low Damage, *Ecs Journal of Solid State Science and Technology*, 2015, **4**, N5095-N5097.

145. Y. C. Zhao and C. T. Jafvert, Environmental photochemistry of single layered graphene oxide in water, *Environmental Science-Nano*, 2015, **2**, 136-142.
146. T. Ji, Y. Hua, M. Sun and N. Ma, The mechanism of the reaction of graphite oxide to reduced graphene oxide under ultraviolet irradiation, *Carbon*, 2013, **54**, 412-418.
147. J. G. Radich, A. L. Krenselewski, J. Zhu and P. V. Kamat, Is Graphene a Stable Platform for Photocatalysis? Mineralization of Reduced Graphene Oxide With UV-Irradiated TiO2 Nanoparticles, *Chemistry of Materials*, 2014, **26**, 4662-4668.
148. W.-C. Hou, I. Chowdhury, D. G. Goodwin, Jr., W. M. Henderson, D. H. Fairbrother, D. Bouchard and R. G. Zepp, Photochemical Transformation of Graphene Oxide in Sunlight, *Environmental Science & Technology*, 2015, **49**, 3435-3443.
149. Y. Li, N. Yang, T. T. Du, X. Z. Wang and W. Chen, Transformation of graphene oxide by chlorination and chloramination: Implications for environmental transport and fate, *Water Research*, 2016, **103**, 416-423.
150. J. W. Wu, L. B. Alemany, W. L. Li, D. Benoit and J. D. Fortner, Photoenhanced transformation of hydroxylated fullerene (fullerol) by free chlorine in water, *Environmental Science-Nano*, 2017, **4**, 470-479.
151. J. W. Wu, W. Li and J. D. Fortner, Photoenhanced oxidation of C-60 aggregates (nC(60)) by free chlorine in water, *Environmental Science-Nano*, 2017, **4**, 117-126.
152. J. W. Wu, D. Benoit, S. S. Lee, W. L. Li and J. D. Fortner, Ground State Reactions of nC(60) with Free Chlorine in Water, *Environmental Science & Technology*, 2016, **50**, 721-731.
153. T. T. Du, A. S. Adeleye, A. A. Keller, Z. N. Wu, W. Han, Y. Y. Wang, C. D. Zhang and Y. Li, Photochlorination-induced transformation of graphene oxide: Mechanism and environmental fate, *Water Research*, 2017, **124**, 372-380.
154. J. D. Fortner, D.-I. L. Kim, A. M. Boyd, J. C. Falkner, S. Moran, V. L. Colvin, J. B. Hughes and J.-H. Kim, Reaction of Water-Stable C-60 aggregates with ozone, *Environmental Science & Technology*, 2007, **41**, 7497-7502.
155. L. S. Clesceri, A. D. Eaton, A. E. Greenberg, A. P. H. Association, A. W. W. Association and W. E. Federation, *Standard Methods for the Examination of Water and Wastewater*, American Public Health Association, 1998.
156. R. Y. N. Gengler, D. S. Badali, D. Zhang, K. Dimos, K. Spyrou, D. Gournis and R. J. D. Miller, Revealing the ultrafast process behind the photoreduction of graphene oxide, *Nature Communications*, 2013, **4**.
157. X. Y. Yang, X. B. Wang, J. Li, J. Yang, L. Wan and J. C. Wang, Controllable Reduction and Structural Characterizations of Graphene Oxides, *Chemical Journal of Chinese Universities-Chinese*, 2012, **33**, 1902-1907.
158. J. L. Chen, X. M. Zhang, X. L. Zheng, C. Liu, X. Q. Cui and W. T. Zheng, Size distribution-controlled preparation of graphene oxide nanosheets with different C/O ratios, *Materials Chemistry and Physics*, 2013, **139**, 8-11.
159. T. Xia, J. D. Fortner, D. Zhu, Z. Qi and W. Chen, Transport of Sulfide-Reduced Graphene Oxide in Saturated Quartz Sand: Cation-Dependent Retention Mechanisms, *Environmental Science & Technology*, 2015, **49**, 11468-11475.
160. Y. J. Jung, K. W. Baek, B. S. Oh and J. W. Kang, An investigation of the formation of chlorate and perchlorate during electrolysis using Pt/Ti electrodes: The effects of pH and reactive oxygen species and the results of kinetic studies, *Water Research*, 2010, **44**, 5345-5355.

161. C. H. Liao, S. F. Kang and F. A. Wu, Hydroxyl radical scavenging role of chloride and bicarbonate ions in the H2O2/UV process, *Chemosphere*, 2001, **44**, 1193-1200.
162. Y. G. Feng, D. W. Smith and J. R. Bolton, Photolysis of aqueous free chlorine species (NOCI and OCI-) with 254 nm ultraviolet light, *Journal of Environmental Engineering and Science*, 2007, **6**, 277-284.
163. A. C. Ferrari, J. C. Meyer, V. Scardaci, C. Casiraghi, M. Lazzeri, F. Mauri, S. Piscanec, D. Jiang, K. S. Novoselov, S. Roth and A. K. Geim, Raman spectrum of graphene and graphene layers, *Physical Review Letters*, 2006, **97**.
164. Y. Si and E. T. Samulski, Synthesis of water soluble graphene, *Nano Letters*, 2008, **8**, 1679-1682.
165. Y. Gao, X. G. Jian and J. Y. Wang, Synthesis and characterization of poly (aryl ether ketone) containing phthalazinone and naphthalene moieties, *Chinese Chemical Letters*, 2000, **11**, 777-778.
166. F. Cataldo, Photochlorination of C60 and C70 Fullerenes, *Carbon*, 1994, **32**, 437-443.
167. A. Fujimoto, Y. Yamada, M. Koinuma and S. Sato, Origins of sp3C peaks in C1s X-ray Photoelectron Spectra of Carbon Materials, *Analytical chemistry*, 2016, **88**, 6110-6114.
168. J. Mansouri, S. Harrisson and V. Chen, Strategies for controlling biofouling in membrane filtration systems: challenges and opportunities, *Journal of Materials Chemistry*, 2010, **20**, 4567-4586.
169. A. Matin, Z. Khan, S. M. J. Zaidi and M. C. Boyce, Biofouling in reverse osmosis membranes for seawater desalination: Phenomena and prevention, *Desalination*, 2011, **281**, 1-16.
170. H. M. Colquhoun, D. Chappell, A. L. Lewis, D. F. Lewis, G. T. Finlan and P. J. Williams, Chlorine tolerant, multilayer reverse-osmosis membranes with high permeate flux and high salt rejection, *Journal of Materials Chemistry*, 2010, **20**, 4629-4634.
171. J. Glater, S. K. Hong and M. Elimelech, THE SEARCH FOR A CHLORINE-RESISTANT REVERSE-OSMOSIS MEMBRANE, *Desalination*, 1994, **95**, 325-345.
172. H. R. Chae, J. Lee, C. H. Lee, I. C. Kim and P. K. Park, Graphene oxide-embedded thin-film composite reverse osmosis membrane with high flux, anti-biofouling, and chlorine resistance, *Journal of Membrane Science*, 2015, **483**, 128-135.
173. M. Safarpour, A. Khataee and V. Vatanpour, Thin film nanocomposite reverse osmosis membrane modified by reduced graphene oxide/TiO2 with improved desalination performance, *Journal of Membrane Science*, 2015, **489**, 43-54.
174. S. Park, D. A. Dikin, S. T. Nguyen and R. S. Ruoff, Graphene Oxide Sheets Chemically Cross-Linked by Polyallylamine, *Journal of Physical Chemistry C*, 2009, **113**, 15801-15804.
175. L. Hureiki, J. P. Croue and B. Legube, CHLORINATION STUDIES OF FREE AND COMBINED AMINO-ACIDS, *Water Research*, 1994, **28**, 2521-2531.
176. V. T. Do, C. Y. Y. Tang, M. Reinhard and J. O. Leckie, Degradation of Polyamide Nanofiltration and Reverse Osmosis Membranes by Hypochlorite, *Environmental Science & Technology*, 2012, **46**, 852-859.
177. J. Powell, J. Luh and O. Coronell, Bulk Chlorine Uptake by Polyamide Active Layers of Thin-Film Composite Membranes upon Exposure to Free Chlorine-Kinetics, Mechanisms, and Modeling, *Environmental Science & Technology*, 2014, **48**, 2741-2749.

178. S. Al-Gharabli, J. Kujawa, M. O. Mavukkandy and H. A. Arafat, Functional groups docking on PVDF membranes: Novel Piranha approach, *European Polymer Journal*, 2017, **96**, 414-428.
179. S. Iftekhar, D. L. Ramasamy, V. Srivastava, M. B. Asif and M. Sillanpaa, Understanding the factors affecting the adsorption of Lanthanum using different adsorbents: A critical review, *Chemosphere*, 2018, **204**, 413-430.
180. T. G. Goonan, *Rare earth elements: end use and recyclability*, Report 2011-5094, Reston, VA, 2011.
181. Z. C. Sims, D. Weiss, S. K. McCall, M. A. McGuire, R. T. Ott, T. Geer, O. Rios and P. A. E. Turchi, Cerium-Based, Intermetallic-Strengthened Aluminum Casting Alloy: High-Volume Co-product Development, *Jom*, 2016, **68**, 1940-1947.
182. C. Borra, T. J. H. Vlugt, Y. Yang and S. Erik Offerman, *A BRIEF REVIEW ON RECOVERY OF CERIUM FROM GLASS POLISHING WASTE*, 2017.
183. N. N. Vinogradova, L. N. Dmitruk and O. B. Petrova, Glass Transition and Crystallization of Glasses Based on Rare-Earth Borates, *Glass Physics and Chemistry*, 2004, **30**, 1-5.
184. A. C. V. de Araujo, I. T. Weber, B. S. Santos, B. J. P. da Silva, R. P. de Mello Jr, S. Alves Jr, G. F. de Sa and C. de Mello Donega, Spectroscopy and crystallization behavior of Eu3+-doped La2O3: B2O3 binary glasses, *Journal of Non-Crystalline Solids*, 1997, **219**, 160-164.
185. F. Gan, Recent development of scintillating glasses with heavy metal elements, *Proc. XII Intern. Simposium on Non-Oxide Glasses and Advanced Materials. Brazil*, 2000, 433-438.
186. S. Gorman, As hybrid cars gobble rare metals, shortage looms.*Journal*, 2009.
187. S.-L. Lin, K.-L. Huang, I. C. Wang, I. C. Chou, Y.-M. Kuo, C.-H. Hung and C. Lin, Characterization of spent nickel–metal hydride batteries and a preliminary economic evaluation of the recovery processes, *Journal of the Air & Waste Management Association*, 2016, **66**, 296-306.
188. S. Massari and M. Ruberti, Rare earth elements as critical raw materials: Focus on international markets and future strategies, *Resources Policy*, 2013, **38**, 36-43.
189. H. Sepehrian, R. Cheraghali, P. Rezaei and H. alla Abdi, Adsorption behavior studies of Cerium on modified Mesoporous Aluminosilicate, *International Journal of Nano Dimension*, 2014, **5**, 169-175.
190. R. Kecili, I. Dolak, B. Ziyadanogullari, A. Ersoz and R. Say, Ion imprinted cryogel-based supermacroporous traps for selective separation of cerium(III) in real samples, *Journal of Rare Earths*, 2018, **36**, 857-862.
191. S. Nishihama, K. Kohata and K. Yoshizuka, Separation of lanthanum and cerium using a coated solvent-impregnated resin, *Separation and Purification Technology*, 2013, **118**, 511-518.
192. E. H. Borai, M. G. Hamed, A. M. El-Kamash and M. M. Abo-Aly, Sonochemical synthesis and characterization of emulsion polymer for sorption of lanthanides, *Journal of Molecular Liquids*, 2018, **255**, 556-561.
193. J. D. Chen, W. J. Luo, A. F. Guo, T. T. Luo, C. Lin, H. F. Li and L. R. Jing, Preparation of a novel carboxylate-rich palygorskite as an adsorbent for Ce3+ from aqueous solution, *Journal of Colloid and Interface Science*, 2018, **512**, 657-664.

194. L. Cheng, S. Yu, C. Zha, Y. Yao and X. Pan, Removal of simulated radionuclide Ce(III) from aqueous solution by as-synthesized chrysotile nanotubes, *Chemical Engineering Journal*, 2012, **213**, 22-30.
195. M. N. Lahiji, A. R. Keshtkar and M. A. Moosavian, Adsorption of cerium and lanthanum from aqueous solutions by chitosan/polyvinyl alcohol/3-mercaptopropyltrimethoxysilane beads in batch and fixed-bed systems, *Particulate Science and Technology*, 2018, **36**, 340-350.
196. M. Khalil, Y. F. El-Aryan and E. M. El Afifi, Sorption performance of light rare earth elements using zirconium titanate and polyacrylonitrile zirconium titanate ion exchangers, *Particulate Science and Technology*, 2018, **36**, 618-627.
197. M. M. H. Khalil, M. S. Atrees, A. I. L. Abd El Fatah, H. Salem and R. Roshdi, Synthesis and application studies of chitosan acryloylthiourea derivative for the separation of rare earth elements, *Journal of Dispersion Science and Technology*, 2018, **39**, 605-613.
198. X. J. Li, C. J. Yan, W. J. Luo, Q. Gao, Q. Zhou, C. Liu and S. Zhou, Exceptional cerium(III) adsorption performance of poly(acrylic acid) brushes-decorated attapulgite with abundant and highly accessible binding sites, *Chemical Engineering Journal*, 2016, **284**, 333-342.
199. , !!! INVALID CITATION !!! 14.
200. C. Kutahyali, S. Sert, B. Cetinkaya, S. Inan and M. Eral, Factors Affecting Lanthanum and Cerium Biosorption on Pinus brutia Leaf Powder, *Separation Science and Technology*, 2010, **45**, 1456-1462.
201. C. Kutahyali, S. Sert, B. Cetinkaya, E. Yalcintas and M. B. Acar, Biosorption of Ce(III) onto modified Pinus brutia leaf powder using central composite design, *Wood Science and Technology*, 2012, **46**, 721-736.
202. Z. S. Birungi and E. M. N. Chirwa, The kinetics of uptake and recovery of lanthanum using freshwater algae as biosorbents: Comparative analysis, *Bioresource Technology*, 2014, **160**, 43-51.
203. M. Torab-Mostaedi, M. Asadollahzadeh, A. Hemmati and A. Khosravi, Biosorption of lanthanum and cerium from aqueous solutions by grapefruit peel: equilibrium, kinetic and thermodynamic studies, *Research on Chemical Intermediates*, 2015, **41**, 559-573.
204. D. Das, C. J. S. Varshini and N. Das, Recovery of lanthanum(III) from aqueous solution using biosorbents of plant and animal origin: Batch and column studies, *Minerals Engineering*, 2014, **69**, 40-56.
205. M. Torab-Mostaedi, BIOSORPTION OF LANTHANUM AND CERIUM FROM AQUEOUS SOLUTIONS USING TANGERINE (Citrus reticulate) PEEL: EQUILIBRIUM, KINETIC AND THERMODYNAMIC STUDIES, *Chemical Industry & Chemical Engineering Quarterly*, 2013, **19**, 79-88.
206. G. X. Zhao, J. X. Li, X. M. Ren, C. L. Chen and X. K. Wang, Few-Layered Graphene Oxide Nanosheets As Superior Sorbents for Heavy Metal Ion Pollution Management, *Environmental Science & Technology*, 2011, **45**, 10454-10462.
207. W. Chen, L. Wang, M. Zhuo, Y. Liu, Y. Wang and Y. Li, Facile and highly efficient removal of trace Gd (III) by adsorption of colloidal graphene oxide suspensions sealed in dialysis bag, *Journal of hazardous materials*, 2014, **279**, 546-553.
208. R. R. Amirov, J. Shayimova and A. M. Dimiev, Distribution of Gd(III) ions at the graphene oxide/water interface, *Journal of Colloid and Interface Science*, 2018, **527**, 222-229.

209. Y. Sun, Q. Wang, C. Chen, X. Tan and X. Wang, Interaction between Eu (III) and graphene oxide nanosheets investigated by batch and extended X-ray absorption fine structure spectroscopy and by modeling techniques, *Environmental science & technology*, 2012, **46**, 6020-6027.
210. Y. B. Sun, D. D. Shao, C. L. Chen, S. B. Yang and X. K. Wang, Highly Efficient Enrichment of Radionuclides on Graphene Oxide-Supported Polyaniline, *Environmental Science & Technology*, 2013, **47**, 9904-9910.
211. F. N. Behdani, A. T. Rafsanjani, M. Torab-Mostaedi and S. Mohammadpour, Adsorption ability of oxidized multiwalled carbon nanotubes towards aqueous Ce(III) and Sm(III), *Korean Journal of Chemical Engineering*, 2013, **30**, 448-455.
212. S. T. Lyu and E. G. Rakov, Sorption of La(III) and Ce(III) by Oxidized Carbon Nanotubes, *Russian Journal of Physical Chemistry A*, 2016, **90**, 2011-2015.
213. Q. G. S. Wang, W. Luo, J. Xu, C. Zhou, H, Xia, Removal of methyl blue from aqueous solution by magnetic carbon nanotube, *Water Science and Technology*, 2013, **68**, 665-673.
214. X. Chen, S. Zhou, L. Zhang, T. You and F. Xu, Adsorption of Heavy Metals by Graphene Oxide/Cellulose Hydrogel Prepared from NaOH/Urea Aqueous Solution, *Materials*, 2016, **9**, 582.
215. M. H. Bradbury and B. Baeyens, Sorption of Eu on Na- and Ca-montmorillonites: experimental investigations and modelling with cation exchange and surface complexation, *Geochimica et Cosmochimica Acta*, 2002, **66**, 2325-2334.
216. B. Bouchaud, J. Balmain, G. Bonnet and F. Pedraza, pH-distribution of cerium species in aqueous systems, *Journal of Rare Earths*, 2012, **30**, 559-562.
217. P. Chanaud, A. Julbe, P. Vaija, M. Persin and L. Cot, Study of lanthanum-based colloidal sols formation, *Journal of Materials Science*, 1994, **29**, 4244-4251.
218. C. Kim, S. Lee and S. Hong, Application of osmotic backwashing in forward osmosis: mechanisms and factors involved, *Desalination and Water Treatment*, 2012, **43**, 314-322.
219. C. Kim and S. Lee, Effect of seepage velocity on the attachment efficiency of TiO2 nanoparticles in porous media, *Journal of hazardous materials*, 2014, **279**, 163-168.
220. Z. B. Zhang, Y. F. Qiu, Y. Dai, P. F. Wang, B. Gao, Z. M. Dong, X. H. Cao, Y. H. Liu and Z. G. Le, Synthesis and application of sulfonated graphene oxide for the adsorption of uranium(VI) from aqueous solutions, *Journal of Radioanalytical and Nuclear Chemistry*, 2016, **310**, 547-557.

Curriculum Vitae

Siyuan An

Ph.D. Candidate
Department of Energy, Environmental and Chemical Engineering
McDonnell International Scholars Academy
China Risun Group (Hong Kong) Corporate Fellow
Washington University in St. Louis
Tel: +1 (314)278-9717
Email: ansiyuan@wustl.edu

EDUCATION

- **Ph.D. Candidate in Chemical Engineering** 2013 – 2018
  Department of Energy, Environmental and Chemical Engineering
  Washington University in St. Louis, MO, US
- **Master of Science in Chemical Engineering** 2011 – 2013
  Department of Chemical Engineering, Institute of Biochemical Engineering
  Tsinghua University, China
- **Bachelor of Science in Chemical Engineering** 2007 – 2011
  Department of Chemical Engineering
  Tsinghua University, China

PROFESSIONAL EXPERIENCE

- **Surface Science Co-Op** June 2018 – Aug 2018
  Novelis, Atlanta, GA
- **Chemical Engineer Intern** May 2017 – Aug 2017
  Lineage Logistics, San Francisco, CA
- **Research Assistant** August 2013 – present
  Department of Energy, Environmental and Chemical Engineering, Washington University in Saint Louis, MO
- **Research Assistant** August 2011 – June 2013
  Department of Chemical Engineering, Institute of Biochemical Engineering, Tsinghua University, China

PUBLICATIONS AND PRESENTATIONS

- **Siyuan An**, Jingying Zhu, Diannan Lu et al. Lipase-catalyzed synthesis and characterization of high-molecular-weight PBS[J]. **CIESC Journal**, 2013, (5): 1855-1861.
- Jingying Zhu, **Siyuan An**, Diannan Lu et al. Development and prospects of enzymatic polymerization[J]. **CIESC Journal**, 2013, 64(2): 407-414.
- **Siyuan An**, Jiewei Wu, Yao Nie and John Fortner. Photoenhanced transformation of graphene oxide by free chlorine: reaction kinetics and product characterization. In revision to **Environmental Science: Nano**.
- Changwoo Kim, **Siyuan An** Junseok, Qingqing Zeng and John Fortner. Engineering graphene oxide laminate membranes for enhanced flux and boron treatment with polyethylenimine (PEI) polymers. In revision to **Desalination**.
- Changwoo Kim, James Meyer, **Siyuan An**, Marcus B. Foston, and John D. Fortner. High efficiency (photo)reduction of chromium by polyethylenimine (PEI) polymers. In revision to **Science of the Total Environment**.
- **Siyuan An**, Wenlu Li, Qingqing Zeng, Kishan Patel and John Fortner. Exploration of graphene oxide synthesis: effect of temperature and sonication on oxidation state, structure and aqueous stability. In preparation.
- **Siyuan An**, Zhiyao Li, Changwoo Kim and John Fortner. Aqueous cerium(III) and lanthanum(III) adsorption on graphene oxide nano-sheet. In preparation.
- Presentation: Jingying Zhu, **Siyuan An**, Diannan Lu and Zheng Liu. Lipase-Catalyzed Synthesis of Poly(butylene succinate). American Institute of Chemical Engineers (AIChE) 2011 Annual Meeting, Minneapolis, MN
- Presentation: **Siyuan An**, Jingying Zhu, Diannan Lu et al. Enzyme-catalyzed synthesis of poly (butylene succinate). Conference of Polymer Science and Engineering. 2012, Wuhan, China.
- Presentation: **Siyuan An**, Jiewei Wu, and John D. Fortner. Photo-enhanced Oxidation of Graphene Oxide in the Presence of Free Chlorine. 21st Annual Mid-America Environmental Engineering Conference (MAEEC). 2015, Columbia, MO.
- Presentation: **Siyuan An**, Jiewei Wu, John Fortner. Photoenhanced oxidation of graphene oxide in the presence of free chlorine. 255th ACS National Meeting, New Orleans, LA. **Invited Speaker**.
- Presentation: Changwoo Kim, **Siyuan An**, John, Fortner. PEI functionalized graphene oxide for enhanced sorption and rapid photoreduction of chromium (VI). 255th ACS National Meeting, New Orleans, LA.